KINETIC GROWTH OF COPPER OXIDATION IN SEMICONDUCTOR PACKAGING

SITI RAHMAH ESA

FACULTY OF SCIENCE
UNIVERSITY OF MALAYA
KUALA LUMPUR

2017

KINETIC GROWTH OF COPPER OXIDATION IN SEMICONDUCTOR PACKAGING

SITI RAHMAH ESA

**DISSERTATION SUBMITTED IN FULFILMENT
OF THE REQUIREMENTS FOR THE DEGREE OF
MASTER OF SCIENCE**

**DEPARTMENT OF CHEMISTRY
FACULTY OF SCIENCE
UNIVERSITY OF MALAYA
KUALA LUMPUR**

2017

UNIVERSITY OF MALAYA

ORIGINAL LITERARY WORK DECLARATION

Name of Candidate: **Siti Rahmah Esa**

Registration/Matric No: **SGR100081**

Name of Degree: **Master of Science**

Title of Project Paper/Research Report/Dissertation/Thesis (“this Work”):

KINETIC GROWTH OF COPPER OXIDATION IN SEMICONDUCTOR PACKAGING

Field of Study: **Chemistry**

I do solemnly and sincerely declare that:

(1) I am the sole author/writer of this Work;
(2) This Work is original;
(3) Any use of any work in which copyright exists was done by way of fair dealing and for permitted purposes and any excerpt or extract from, or reference to or reproduction of any copyright work has been disclosed expressly and sufficiently and the title of the Work and its authorship have been acknowledged in this Work;
(4) I do not have any actual knowledge nor do I ought reasonably to know that the making of this work constitutes an infringement of any copyright work;
(5) I hereby assign all and every rights in the copyright to this Work to the University of Malaya (“UM”), who henceforth shall be owner of the copyright in this Work and that any reproduction or use in any form or by any means whatsoever is prohibited without the written consent of UM having been first had and obtained;
(6) I am fully aware that if in the course of making this Work I have infringed any copyright whether intentionally or otherwise, I may be subject to legal action or any other action as may be determined by UM.

Candidate’s Signature Date:

Subscribed and solemnly declared before,

Witness’s Signature Date:

Name: **Professor Dr. Rosiyah Yahya**

Designation: **Professor**

ABSTRACT

This thesis systematically investigates the physical, mechanical and chemical properties of the copper oxidation on the copper alloy leadframe that influence the reliability of an IC packaging in semiconductor industries. In this study, the oxidation on the copper alloy leadframe was promoted via heat treatment process. The copper oxidation was investigated and characterized using various advanced analytical techniques by means of Optical Microscopy, Field Emission Scanning Electron Microscopy (FESEM), Atomic Force Microscopy (AFM), Vickers Micro-Indentation, Energy Dispersive X-ray Spectroscopy (EDS), Auger Electron Spectroscopy (AES), Focused Ion Beam (FIB), High Resolution Transmission Electron Microscopy (HRTEM) and Energy Electron Loss Spectroscopy (EELS). The oxidation was found to cause a transformation of physical colour of the leadframe from light brown to dark brown. The changes of the surface texture from fine to coarse granular were also observed as a result of the oxidation process. The coarse granular surface derived from high temperature treatment was found to be hard and brittle resulting to the flaky and crack surface as it is induced by the Vickers micro indentation test. The oxidation was found to be initiated at the heat treatment temperature of 120 °C. The copper oxide thickness shows an increasing trend as the temperature increases. The copper oxide thickness growth was 16 nm, 49 nm, 93 nm and 160 nm at the heat treatment temperature of 150 °C, 180 °C, 210 °C and 240 °C respectively. The activation energy was found to be 41 kJ/mol. At high oxidation temperature, the formation of micro-voids and separations were observed along the interface between the copper oxide and the bulk copper leadframe. Poor adhesion at this interface region due to micro-voids and separation were found to be the root cause of the delamination issue. EELS analysis determined that for the regions with intact interface the oxidation system is $CuO/Cu_2O/CuO/Cu$, however, in regions containing micro-voids or separations the oxidation system is found to be $CuO/Cu_2O/Cu$.

ABSTRAK

Tesis ini menyiasat secara sistematik sifat-sifat fizikal, mekanikal dan kimia pengoksidaan tembaga pada kerangka kaki tembaga aloi yang mempengaruhi daya ketahanan pembungkusan IC dalam industri semikonduktor. Dalam kajian ini, pengoksidaan pada kerangka kaki tembaga aloi dilakukan melalui proses rawatan haba. Pengoksidaan tembaga telah dikaji dengan menggunakan pelbagai teknik analisa seperti Optical Microscopy, Field Emission Scanning Electron Microscopy (FESEM), Atomic Force Microscopy (AFM), Vickers Micro-Indentation, Energy Dispersive X-ray Spectroscopy (EDS), Auger Electron Spectroscopy (AES), Focused Ion Beam (FIB), High Resolution Transmission Electron Microscopy (HRTEM) dan Energy Electron Loss Spectroscopy (EELS). Pengoksidaan menyebabkan berlakunya perubahan warna fizikal kerangka kaki daripada coklat terang kepada coklat gelap. Perubahan permukaan tekstur daripada halus kepada kasar juga terjadi akibat proses pengoksidaan. Permukaan kasar yang terhasil daripada rawatan haba bersuhu tinggi didapati keras dan rapuh serta menyebabkan permukaannya tidak kukuh dan rekahan terjadi apabila ujian kekerasan vickers dilakukan. Pengoksidaan didapati bermula pada suhu rawatan haba 120 °C. Ketebalan tembaga oksida adalah bertambah dengan kenaikan suhu. Pertumbuhan ketebalan tembaga oksida adalah 16 nm, 49 nm, 93 nm dan 160 nm masing-masing pada suhu rawatan haba 150 °C, 180 °C, 210 °C dan 240 °C. Tenaga pengaktifan adalah 41 kJ/mol. Pada suhu pengoksidaan yang tinggi, pembentukan ruang kosong mikro dan pemisahan disepanjang permukaan antara oksida tembaga dan tembaga berlaku. Perlekatan yang lemah ini disebabkan oleh pembentukan ruang kosong mikro dan pemisahan adalah punca kepada isu pelekangan. Analisa EELS mendapati bahawa sistem pengoksidaan pada kawasan yang mempunyai permukaan yang melekat adalah $CuO/Cu_2O/CuO/Cu$, bagaimanapun di kawasan yang mempunyai ruang kosong mikro dan pemisahan, sistem pengoksidaan adalah $CuO/Cu_2O/Cu$.

ACKNOWLEDGEMENTS

Alhamdulillah. All praises to Allah for all the graciousness and blessings that have made it possible for me to finish up this thesis write-up.

At the outset, I would like to express my sincere gratitude to my supervisor and co-supervisor; Professor Dr. Rosiyah Yahya and Professor Dr. Aziz Hassan, for the opportunities, encouragement, and guidance.

A special thank goes to my industrial supervisor, Professor Dr. Ghazali Omar for his continuous support, patience, motivation, encouragement and critical reviews on this thesis over the years for which I am truly grateful.

I appreciate the motivation, encouragement and sponsorship from the management of Infineon Technologies Kulim, which made my career and research life very enjoyable. In particular, I thank; Tan Kia Heng, Yong Foo Khong and Gan Chye Siong Kenny for their excellent management and for allowing me to utilize Failure Analysis Laboratory facilities in Infineon Technologies Kulim without having any difficulty, resistance and hesitation. Without their precious support it would not be possible for me to conduct and complete this research work.

I also appreciate the management of MIMOS Berhad, in particular Advanced Analytical Services Laboratory for supporting this thesis write-up, especially Mrs Bazura Abdul Rahim and AAS Lab staff.

I also would like to thank my family; my parents, my sisters and my brother for supporting me spiritually throughout writing this thesis and my life in general.

Last but not the least, I wish to thank all individuals that were very helpful to me in various ways which made it possible for me to complete this research work and thesis.

TABLE OF CONTENTS

LIST OF FIGURES

LIST OF TABLES

LIST OF SYMBOLS AND ABBREVIATIONS

˚C	Degree Celsius
µm	Micro Meter
3D	Three Dimensional
AES	Auger Electron Spectroscopy
AFM	Atomic Force Microscopy
Ag	Silver
Al	Aluminium
Ar	Argon
ASTM	American Society for Testing and Material
Au	Gold
BTAH	Benzotriazole
CCD	Charged Coupled Device
CTE	Coefficient Thermal Expansion
Cu	Copper
Cl	Chlorine
CuO	Cupric Oxide
Cu_2O	Cuprous Oxide
E_a	Activation Energy
EDS	Energy Dispersive X-ray Spectroscopy
EMC	Epoxy Mould Compound
EELS	Electron Energy Loss Spectroscopy
eV	Electron Volt
FCC	Face Centered Cubic
Fe	Iron

FEG	:	Field Emission Gun
FESEM	:	Field Emission Scanning Electron Microscopy
FIB	:	Focused Ion Beam
Ga	:	Gallium
GIS	:	Gas Injection System
HCP	:	Hexagonal Closed Packed
HRTEM	:	High Resolution Transmission Electron Microscopy
HV	:	Vickers Hardness
Hz	:	Hertz
IC	:	Integrated Circuit
IMC	:	Inter-metallic Compound
kJ	:	Kilo Joule
kV	:	Kilo Volt
LMIS	:	Liquid Metal Ion Souce
mN	:	Mili Newton
Mo	:	Molybdenum
MO	:	Metal Oxide
MPa	:	Mega Pascal
NA	:	Not Applicable
nA	:	Nano Ampere
nm	:	Nano Meter
NSOL	:	Non Stick on Lead
O_2	:	Oxygen
OFHC	:	Oxygen Free High Thermal Conductivity
OH	:	Hydroxide
P	:	Phosphorus

P-B	:	Pilling-Bedworth
PCB	:	Printed Circuit Board
Pd	:	Palladium
Pt	:	Platinum
Redox	:	Reduction-Oxidation
RMS	:	Root Mean Square
RT	:	Room Temperature
SAED	:	Selected Area Electron Diffraction
SCC	:	Stress Corrosion Cracking
SiO_2	:	Silicon Dioxide
SMT	:	Surface Mount Technology
STEM	:	Scanning Transmission Electron Microscopy
TEM	:	Transmission Electron Microscopy
TiN	:	Titanium Nitride
XPS	:	X-ray Photoelectron Spectroscopy
XRD	:	X-ray Diffraction
Zn	:	Zinc

LIST OF APPENDICES

CHAPTER 1: INTRODUCTION

1.1 Overview

Copper (Cu) and its alloys are known as one of the most popular and widely used materials in various applications and industries which includes engineering, electrical, electronics, semiconductor packaging as well as applied research fields (Zheng, 2003).

In semiconductor packaging, copper is extensively used as the skeleton of the IC package called leadframe (Li, 2012) and as an interconnection material called wire bonding (Yee, 2012). Copper has tremendous advantages over other material such as gold (Au), aluminium (Al) and nickel (Ni) due to the low-cost factor, high mechanical stability, and excellent electrical and thermal conductivity (Pelzer, 2012). All these advantages attract a lot of development work to study the application of copper as a workable technology (Shuisheng, 2003).

1.2 Problem Statement

Copper by nature has a high affinity towards oxygen and tends to oxidize easily as it is exposed to the elevated temperature (Berriche, 1999). This oxidation phenomenon slows down the application of copper as it can cause serious reliability issues in semiconductor packaging industries. For instance, the oxidation of copper leadframe on the plastic IC package leads to the delamination at the epoxy moulding compound (EMC) and the die-pad interface and frequently causes "*pop-corn*" failures due to the moisture absorption of the moulding compound and finally results in the cracking of the whole plastic package (Lee, 2005). The oxidation of copper leadframe during the heat treatment process for the die attach adhesive curing leads to the wedge bonding failure due to non-stick on lead (NSOL) (Lin, 2002). The oxidation of the interconnection wire also has an effect on the long-term reliability that the oxidize copper may lead to the stress corrosion cracking, it will also decrease the interfacial shear strength and weaken the Cu-Al bonding causing a lot of wire bond lifted issues during the wire bonding process (Tan, 2002).

The surface condition of copper can be further improved by protecting it with another surface finished. Gold (Au), silver (Ag), nickel (Ni), tin (Sn) and a polymer material such as Benzotriazole (BTAH) had been studied widely by many researchers as an alternative to coating materials of copper (Izquierdo, 2010). Although this coating layer is able to improve the surface condition of copper, many semiconductor industries favoured to use copper as a base material without any surface finishing, so that the manufacturing cost can be further minimized while higher profit can be secured.

In order to accomplish the technology breakthrough of copper, the solid understanding of the behaviour of copper at the elevated temperatures is required. Owing to its importance, several studies had been reported on the thermal oxidation of copper leadframe. Lahiri (1998) characterized the oxidation of copper leadframe using X-Ray Diffraction (XRD) technique while Cho (1998) had utilized both XRD and X-ray Photoelectron Spectroscopy (XPS) techniques. Although Cho (1998) included the Transmission Electron Microscopy (TEM) technique, the investigation was only carried out on the lateral view of the copper oxide. The investigation in the interface area of the copper leadframe and the copper oxide was not performed in both studies. This gives an open question why the delamination likely to occur in this interface region.

In this research work, the oxidation of bare copper alloy leadframe samples at elevated temperatures are studied. The leadframe samples were subjected to the heat treatment in air to promote the oxidation. As the leadframe samples experience the oxidation, the surface characteristic is expected to be altered as compared to the as-received sample that has not undergone the oxidation process. However, the degree of the surface modification is subjected to the heat treatment temperatures.

Various advanced analytical techniques were deployed to characterize the surface properties change such as the Optical Microscopy, Field Emission Scanning Electron Microscopy (FESEM), Atomic Force Microscopy (AFM) and Vickers Micro-Indentation Test. The presence of the oxidation was then confirmed by the spectroscopy techniques such as Energy Dispersive X-ray Spectroscopy (EDS), Auger Electron Spectroscopy (AES) and Electron Energy Loss Spectroscopy (EELS). The High Resolution Transmission Electron Microscopy (HRTEM) technique was also equipped to study on the nano-scale oxidation in terms of the oxide thickness, atomic and crystal structure via Selected Area Electron Diffraction (SAED) technique. The kinetic growth of copper oxidation is studied by using the Arrhenius Reaction Rate Model.

1.3 Research Objectives

The objectives of this research work are described as the following;

1. To investigate the physical and mechanical properties change on the surface of the copper alloy leadframe samples at a different heat treatment temperature.
2. To quantify the amount of the oxidation on the surface of the heat treated copper alloy leadframe samples.
3. To determine the oxidation states of the copper oxide.
4. To measure the copper oxide thickness and to perform the interface study in between the copper oxide and the copper alloy leadframe samples.
5. To investigate the kinetic growth of the copper oxidation by measuring the activation energy using the Arrhenius reaction rate model.

1.4 Content of Thesis

The purpose of this study is to investigate the kinetic growth of copper oxidation on the copper alloy leadframe samples.

This research works are divided into 3 major areas;

Chapter 4.1 – Surface characteristic investigations

Chapter 4.2 – Spectroscopy analysis

Chapter 4.3 – Copper oxidation analysis

Chapter 4.1 examines the surface characteristic of the heat treated copper alloy leadframe samples mainly on the physical and mechanical properties changed. The investigation includes the observation of the physical colour change using the high power optical microscopy. The surface textures of the copper alloy leadframe samples were analyzed using the high resolution scanning electron microscopy technique. The 3D surface morphology analysis using atomic force microscopy was performed to quantify the surface roughness of the copper alloy leadframe samples. The mechanical properties of the heat treated copper alloy leadframe samples were then measured using a micro hardness tester. Further detailed examinations of the indentation mark from the hardness test were carried out using high resolution scanning electron microscopy technique. The surface grain and the bulk grain size of the heat treated copper alloy leadframe samples were revealed using focused ion beam. The grain sizes were then measured using ASTM E 112 intercept counting method.

Chapter 4.2 deployed the spectroscopy analysis techniques to validate the presence of the copper oxide on the surface of the copper alloy leadframe samples. The energy dispersive x-ray spectroscopy analysis via the field emission scanning electron microscopy system was acquired from the sample surface to determine the elemental composition of the copper alloy leadframe samples. The auger depth profiling analysis was performed to obtain the depth information of the copper oxide on the copper alloy leadframe surface. This analysis involves argon (Ar) ion sputtering and a SiO_2 standard sample for the etching rate calibration. This technique allows the estimation of the copper oxide thickness based on the depth profile information. The elemental mapping and the line scan analysis using the energy dispersive x-ray spectroscopy via scanning transmission electron microscopy technique in the cross section view of the sample was then performed to obtain the elemental distribution and the line profile information of the sample. The electron energy loss spectroscopy analysis via the transmission electron microscopy system allows the determination of the nano scale copper oxidation state to be done in the cross section view of the sample.

Chapter 4.3 discussed the growth of the copper oxide in the cross section view of the samples using the high resolution transmission electron microscopy technique. This analysis allows the detailed examination to be done on the copper oxide layer as well as the interface of the copper oxide to the bulk copper alloy leadframe sample. This interface region is examined to understand the factor that contributes to the delamination issues on the oxidized copper. The high resolution transmission electron microscopy analysis also enables accurate copper oxide thickness measurement as compared to the auger depth profiling analysis technique. This is due to the high resolution transmission electron microscopy analysis allows a nano scale examination whereby the auger depth profiling analysis uses SiO_2 as a standard for the etching rate calibration. The crystal structure analysis of the copper oxide layer was then performed using the selected area electron diffraction technique via the transmission electron microscopy system. Lastly, the kinetic growth of the copper oxidation is discussed by measuring the activation energy using the Arrhenius reaction rate model.

CHAPTER 2: LITERATURE REVIEW

2.1 Copper and its Alloy

Copper and copper-based alloys, has been utilized in a variety of applications since antiquity (Reardon, 2011). Unalloyed copper is soft and ductile and therefore, it is difficult to machine (Haque, 2008). It also has unlimited capacity to be cold worked. The mechanisms and properties of copper may be improved by alloying. This is achieved by making a solid material out of two or more different metals (Volkov, 2004). By combining copper with other metals, alloys can be made to fit almost any application. There are more than 400 copper alloys, each with a unique combination of properties, to suit many applications, manufacturing processes, and environments (Romano, 2015). Some of these applications include power transmission lines, architectural applications, spark plugs, electrical wiring, cables and high conductivity wires, electrical and electronic products.

The chemical symbol for copper is Cu, (from Latin: *cuprum*). Copper has the atomic number of 29 (the number of protons in an atom) and is in the “transition metals” group in the periodic table. Copper is in the same periodic table group as gold (Au) and silver (Ag). Therefore, it is relatively inert against chemicals. In most of its compounds, it can have the valence of +I or the valence state +II for the oxidation state. When exposed to the atmosphere, protective layers of oxide forms on the surface of copper and its alloy (Kim, 2006). Copper has the crystal structure of face-centered cubic (FCC) (Yariv, 1984). It is based on one of the 14 Bravais lattices. Each copper atom has 12 nearest neighbours. Copper also has high electrical and thermal conductivity (Maki, 2013). The melting point of copper is 1083 ˚C (Park, 2007). It also has high mechanical stability. Copper also formed great reliability of the bonding wire as it forms less inter-metallic compound (IMC) growths in semiconductor packaging process (Leong, 2013).

2.2 Copper Leadframe in Semiconductor Packaging

In semiconductor packaging, a commercial copper leadframes are produced in a long strip. This allows quick processed of leadframes on assembly machines. In manufacturing processes, there are two main techniques for leadframes productions, namely photo etching (Ohno, 1993) and stamping (Deo, 1994). Typically, the photo etching process is implemented for low to medium volume of leadframes production. Stamping process most often associated with the high volume of production runs. Figure 2.1 shows the image of commercial leadframes in semiconductor packaging.

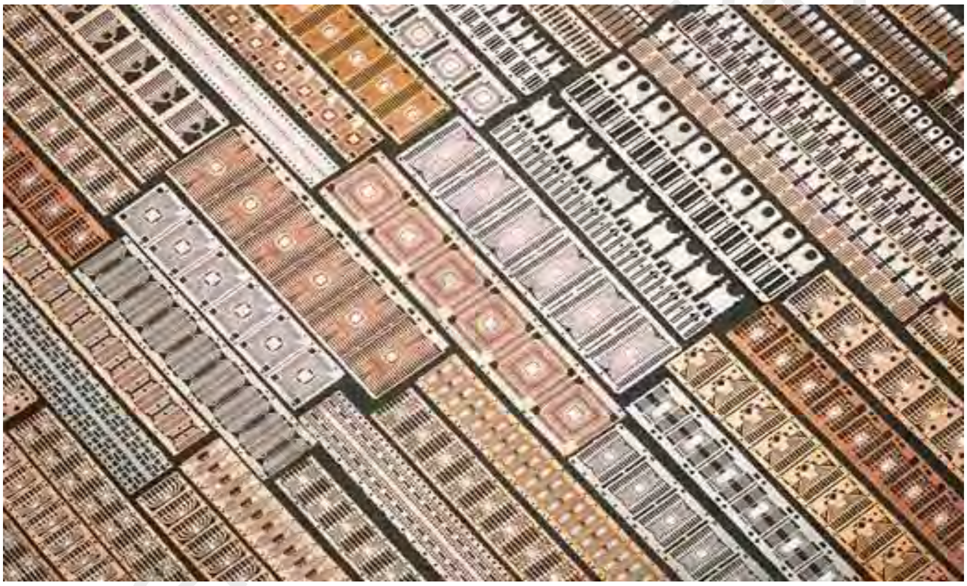

Figure 2.1: The Leadframes.

Photo etching is one of the most popular and widely used in the leadframe manufacturing process as it is cost effective and time efficient technique (Nakayama, 1999). The leadframes are manufactured in the flat sheets. The process started with a photoresist film coated on both sides of the sheets. The photoresist is then exposed to the required leadframe pattern using an ultraviolet source. Next, the resist is developed and the remaining resist serves to protect the sheet during the etching process. Finally, the remaining photoresist is stripped-off from the leadframes. The sheet is then singulated into strips and the process completed after the cleaning step.

Stamping is an automated and high-speed leadframe manufacturing process (Tung, 2003). This technique is suitable for large production runs. The leadframes are manufactured in roll form of a metal sheet. Both edges of the metal sheet are pierced to form indexing holes to advance the sheet through the stamping machine. Die-and-punch sets specific to the leadframe geometry is required for this technique. Series of the stamping operations is essential to accomplish the final leadframe geometry. The complexity of the leadframe geometry determines the number of stamping steps for this process.

Leadframes are primarily used as the skeleton of the IC package to support the semiconductor dies mechanically during the IC packaging process. Leadframes served as an electrical interconnects between semiconductor dies of the IC package with external circuitries. Leadframes are also functioning as the main path for the heat transfer and heat dissipation (Smith, 1977).

Semiconductor packaging process starts with diced a semiconductor wafer into individual dies. The wafer dicing process is accomplished by mechanical sawing or by laser cutting. Upon the dicing process, the semiconductors dies are then attached onto the die pads of the leadframe via the die attach process. Next, the electrical connection between the dies and the respective leads is formed using a fine wire via wire bonding process. Copper is also one of the typical materials for the wire bonding (Liu, 2012).

Figure 2.2 shows the typical image of a semiconductor die that was attached onto the die pad of the copper leadframe. Finally, the leadframe is encased with mould compound to encapsulate the semiconductor dies. Figure 2.3 shows the image of the common IC packages. The illustration of the cross section of the IC packages is shown in Figure 2.4.

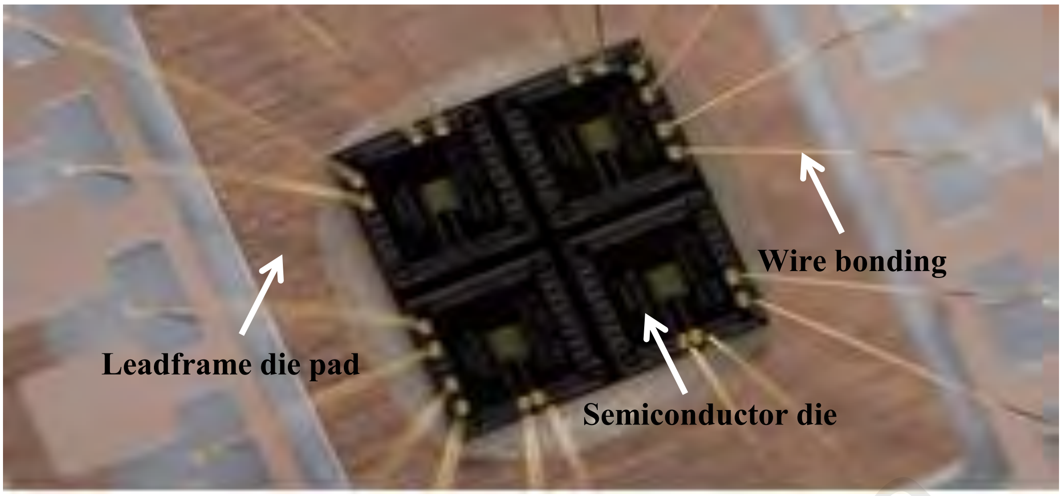

Figure 2.2: Semiconductor dies on the die pad of the copper leadframe.

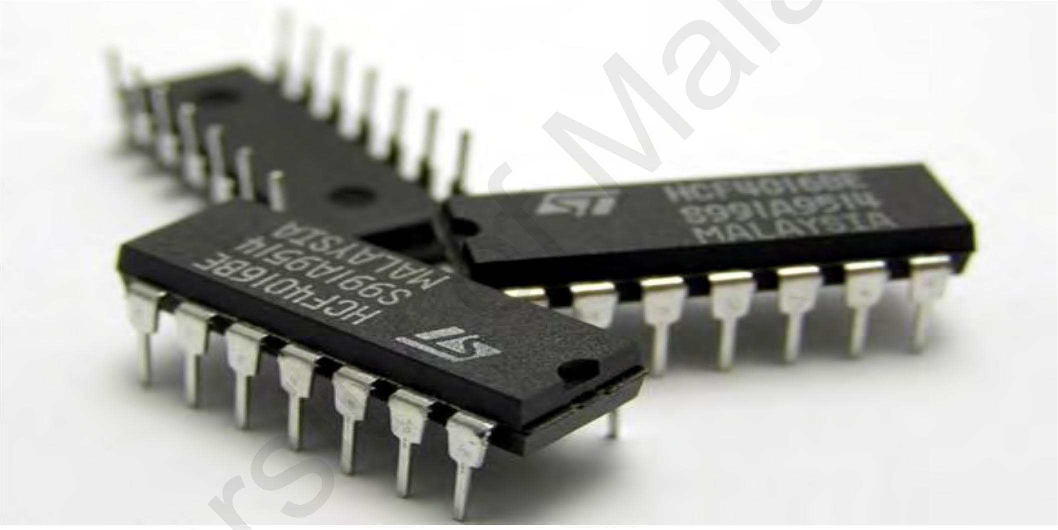

Figure 2.3: The IC packages.

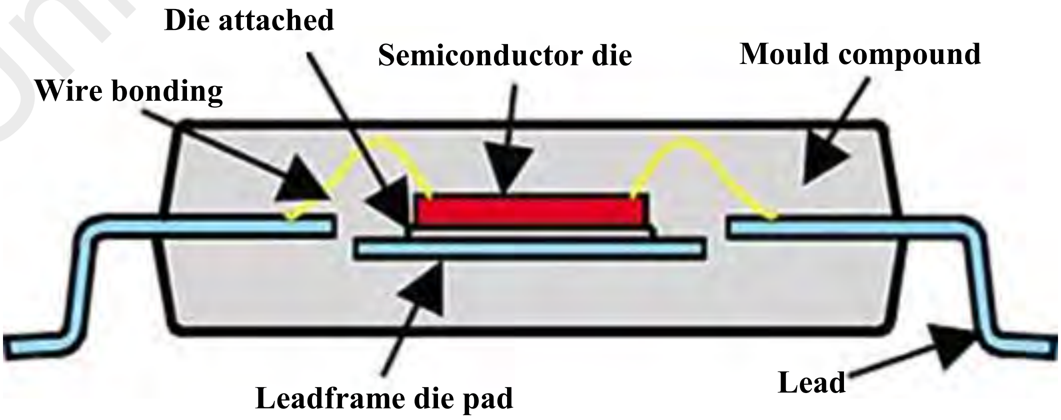

Figure 2.4: The cross section of the IC package.

During the IC packaging process, copper leadframe is subjected to an elevated temperature. For instance, during the die attach curing process, the leadframes are subjected to the temperature of 150 °C for 3 hours depending on the type of material (Hsieh, 2006). In the wire bonding process, the temperatures are ranging from 180 °C to 280 °C for 20 to 200 seconds. The oxidation is likely to occur as the copper leadframe is very susceptible to the thermal oxidation (Chong, 1995).

The oxidation on the copper leadframe has a negative effect on the adhesion of the leadframe to the epoxy moulding compound (EMC) resulting in the interface delamination issues (Lee, 2001). The moisture resistance will decrease significantly if it is not properly controlled which in turn will result in the cracking on the IC package (Lin, 1988).

The control of the moisture sensitivity level leads to the tighten specification in the rule of surface mount technology (SMT) that the package needs to be baked as a process of moisture removal before the package is soldered onto the printed circuit board (PCB) (Shook, 2000).

Therefore, the presence of an oxide layer on the leadframe material has been identified as a contributing factor to the package integrity and reliability issues (Kim, 2000). It is important to develop an in-depth understanding of the oxidation characteristics and mechanism of the oxide growth on the copper leadframes in order to find a means of minimizing the delamination issues between the leadframe and EMC.

2.3 The Mechanisms of Oxidation at High Temperature

Metal and its alloys are environmentally unstable at the elevated temperatures, wherein an oxide layer or scale forms on the surface. This phenomenon is frequently termed as scaling, tarnishing, dry corrosion or oxidation and occurs at a different rate. The reaction rates increase rapidly with an increase in temperature (Belousov, 2013).

At high temperature range, most reactions are completed at short exposure time (Zhao, 2010). Therefore, depending on the equilibrium conditions, oxygen-metal reactions are always likely to occur. At high temperatures, the reaction at metal-air interface forms an intermediate layer in between the metal and air. In order for the reaction to proceed further, one or both reactants must penetrate and diffuse into each other. Two possible mechanisms are either metal transported through the oxide to the oxide-air interface and react, or oxygen transported to the oxide-metal interface and react (Picone, 2016). The mechanisms by which the reactants may penetrate the oxide layers are an important part of the oxidation mechanism at high temperatures.

Metal oxides are ionic bonds, and therefore, ions and electrons must migrate for the reaction to occur (Jackson, 2009). The transporting step of the reaction mechanism links the two-phase boundary reactions, as illustrated in Figure 2.5. Cation migration leads to the scale formation at the scale-air interface, whereas anion migration leads to the scale formation at the metal-scale interface (Cottis, 2009).

It is necessary that electrons be conducted to the scale-air interface, for the oxide layer to increase in thickness. In addition, M^{2+} ions must diffuse away from the metal-scale interface and/or O^{2-} must diffuse towards the same interface. Thus, the oxide scale serves as both an electrolyte through which ions diffuse and as an electrical circuit for the passage of the electrons. Furthermore, the scale may protect the metal from rapid oxidation when it acts as a barrier to ionic diffusion and/or electrical connection.

Cation mobile

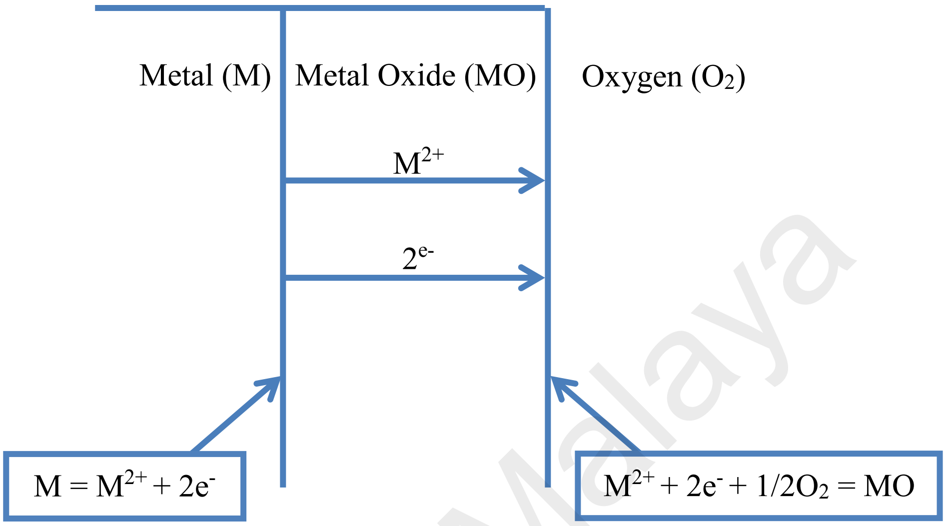

Anion mobile

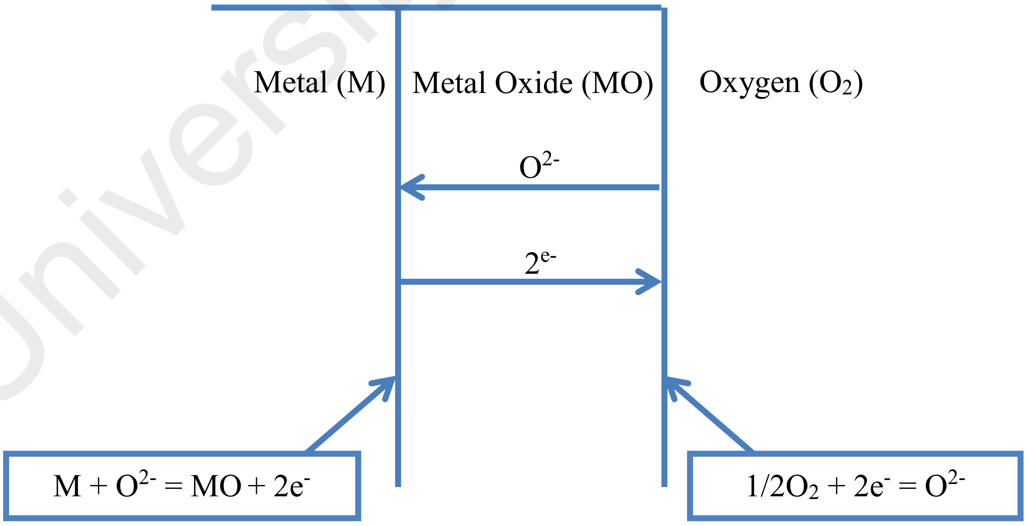

Figure 2.5: The mechanism of the oxidation at high temperature.

2.4 The Oxidation State of Copper

Chemical reactions can be divided into two classes, namely redox (reduction-oxidation) reactions and non-redox reactions. It is based on whether the electron transfer process is involved or not. A redox reaction consists of two half reactions; a reductive half-reaction in which a reactant accepts electrons and an oxidative half-reaction in which a reactant donates electrons. The nature of a redox reaction is that one reactant donates its electrons to the other reagent (Bishop, 2013).

The oxidation of copper starts with the formation of copper (I) oxide (Cu_2O) when copper atoms initially react with oxygen molecules in the air. Copper atoms donate electrons to an oxygen molecule so copper is oxidized while oxygen is reduced (Neikov, 2009).

$$2Cu + O_2 \rightarrow Cu_2O \quad (1)$$

Copper (I) oxide is further oxidized to form copper (II) oxide (CuO).

$$2Cu_2O + O_2 \rightarrow 4CuO \quad (2)$$

The rate of oxidation and the tendency of the film to protect the metal from further oxidation are related to the relative volumes of the oxide and metal. The ratio of this volume termed as Pilling-Bedworth (P-B) ratio (Beranger, 1989). P-B ratio is the ratio of the volume of the elementary cell of a metal oxide to the volume of the elementary cell of the corresponding metal (William, 2011).

For metals having P-B ratio less than unity, the oxide film tends to be porous and un-protective because it is insufficient to fully cover the metal surface. If the ratio is greater than unity, compressive stress results in the film as it forms. The oxide coating may crack and flake-off, continually exposing a fresh and unprotected metal surface if the P-B ratio is greater than 2-3 (Barsoum, 2002).

The ideal ratio of P-B for the formation of a protective oxide film is unity. There are other factors that also influence the oxidation resistance imparted by the film, this includes to a degree of adherence between the film and metal and comparable coefficient of thermal expansion (CTE) for metal and oxide.

Horváth (2012) in his study observed that the P-B ratio for Cu_2O and CuO on copper metal is given as 1.67 and 1.72, respectively. Hence, in the case of the oxidation of the copper grains in the alloy, the volume can expand up to +72 %, depending on the ratio of the developed copper-oxide type. Therefore the larger the copper content is in an alloy, the more stress will develop in the layer due to the larger expansion of the corrosion product within the alloy.

2.5 Crack Initiation and Propagation

The corrosion of copper at elevated temperature can cause serious reliability issues in semiconductor packaging. The long-term oxidation at an elevated temperature leads to the corrosion of copper (Lobnig, 1994). The corrosion rate of copper is determined by the corrosion mechanism. Figure 2.6 shows the typical flake appearance due to the corrosion of metal.

Figure 2.6: Typical flake appearance due to corrosion of metal.

The corrosion layer may flake off due to the corrosion and surface film growth (Segneanu, 2012). Wan (2012) has done the oxidation study of copper at 800 ˚C and found that the corrosion products of copper were easily broken into two layers; the inner and the outer layers. The outer layer is easy to flake off from the inner layer as the effect of corrosion.

Zhang (2014) in his study of the corrosion effect has done mechanistic studies of the corrosion product flaking off on copper and copper-based alloys in marine environments. He found out that the formation of flaking caused the volume expansion during the transformation of the material of $CuCl$ to $Cu_2(OH)_3Cl$.

The formation of the flakes is a phenomenon of Stress Corrosion Cracking (SCC). This is the results of the interaction of corrosion and mechanical stress produced a failure by cracking (Woodtli, 2000). In engineering material, SCC is used to describe failures that occur by environmentally induced crack propagation (Manfredi, 2002). In SCC, the cracks initiate and propagate progressively until the stresses in the remaining metal exceed the fracture strength (Totten, 2008).

The process of SCC involved three stages:

1. Crack initiation; small crack forms at some point of high stress concentration.
2. Crack propagation; the crack advances incrementally with each stress cycle.
3. Final failure; occurs rapidly once the advancing crack has reached a critical size.

The contribution of the final failure of the total fatigue life is insignificant since it occurs rapidly. Crack associated with fatigue failure always initiates on the surface of a component at some points of stress concentration. Crack nucleation includes surface scratches, sharp fillet, thread, dent and the like. Once the stable crack has nucleated, it is then initially propagates slowly. In metals, cracks normally extend through several grains during the propagation stage (Krupp, 2007).

Several mechanisms have been proposed to explain the stress-corrosion interactions that occur at the crack tip. It is likely that more than one process can cause SCC. The proposed mechanisms can be classified into two basic categories: anodic mechanisms and cathodic mechanisms. That is, during corrosion, both anodic and cathodic reactions must occur, and the phenomena that result in the crack propagation may be associated with either type (Jones, 1992).

The most obvious anodic mechanism is that of simple active dissolution and removal of material from the crack tip. The most obvious cathodic mechanism is hydrogen evolution, absorption, diffusion, and embrittlement (Garveric, 1994). However, a specific mechanism must be able to explain the actual crack-propagation rates, the fractographic evidence, and the mechanism of formation or nucleation of cracks. Mechanical fracture includes normal fracture processes that are assumed to be stimulated or induced by one of the following interactions between the material and the environment:

1. Adsorption of environmental species.
2. Surface reactions.
3. Reactions in the metal ahead of the crack tip.
4. Surface films.

Copper has two possible oxidation states; a cuprous oxide (Cu_2O) and cupric oxide (CuO). The amount of Cu_2O and CuO has an essential effect on the development of copper corrosion (Wan, 2012). The scale of Cu_2O and CuO formed on copper in the oxygen environments and at the elevated temperature depends on the thermodynamic stability of the oxides. Thus, it is of interest to examine the thermodynamic aspect of this reaction following by studies of the kinetics, compound and morphological aspects.

2.6 The Diffusion Characteristics and Mechanisms

The diffusion mechanism is illustrated in Figure 2.7. It is categorized based on the paths of the movement (Brook, 2012), into:

1. Lattice diffusion.
2. Dislocation diffusion.
3. Grain boundary diffusion.
4. Surface diffusion.

Lattice diffusion, also called volume diffusion or bulk diffusion refers to diffusion processes in the interior of crystals and in regions having a regular crystal structure. In crystalline materials, there are regular array lattice sites that are energetically favoured positions of atoms. The basic assumption made to explain lattice diffusion is that each diffusing atom makes a series of a jump between the various equilibrium lattice sites. These jumps allow the atom to migrate through the crystal. Hence, these mechanisms are often called point defect mechanisms. Several mechanisms can be distinguished in the lattice diffusion by the type of elementary jumps (Mehrer, 2007).

Typical lattice diffusion mechanisms are:

1. Vacancy mechanism.
2. Interstitial mechanism.
3. Exchange mechanism.

2.6.1 Vacancy Mechanism

Any crystal at a temperature above absolute zero contains some vacant sites, which provide an easy path for lattice diffusion. An atom of species A jumps into a neighbouring vacancy, as shown in Figure 2.7 (a). The site previously occupied by the atom is then vacant so that in effect, the atom and vacancy simply exchange position. Each atom moves through the crystal by a series of exchanges with vacancies in its vicinity from time to time. Vacancy density (concentration) therefore plays an important role in lattice diffusion. Vacancy density increases with temperature because of the increasing thermal instability of the lattice in high temperature. The vacancy mechanism is usually dominant in diffusion processes at high temperatures (Balluffi, 2005).

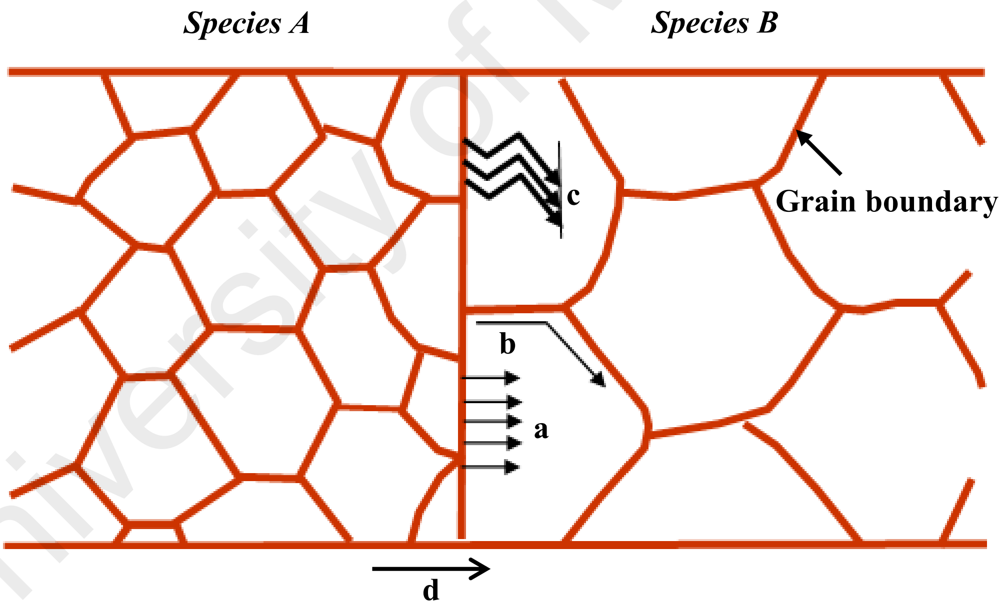

a. Lattice diffusion

b. Dislocation diffusion

c. Grain boundary diffusion

d. Surface diffusion

Figure 2.7: The mechanisms of diffusion in solid.

2.6.2 Interstitial Mechanism

An atom of species A moves through the lattice of species B by jumping directly from one interstitial site to another, as shown in Figure 2.7 (b). This mechanism is particularly likely for diffusion of small atoms of species A, usually as impurity atoms, in the lattice of species B having large atoms. These small atoms, easily fitted into interstitial sites and jumping into nearby interstitial sites, without greatly displace the lattice of species B. Interstitial atom concentration is thus important in interstitial mechanism dominated by lattice diffusion (Nishi, 2000).

2.6.3 Exchange mechanism

The elementary jump is the direct interchange of two neighbouring atoms, as shown in Figure 2.7 (c). This mechanism is unlikely in crystals with tightly packed atomic structures such as hexagonal closed packed (HCP) because that requires high activation energy.

It is possible, however, for this mechanism to occur in a thin film of microelectronics devices, because of loosely packed lattice in thin films. For diffusion between a conductor-conductor pair, such as gold to aluminium in microelectronic devices, the vacancy mechanism is more favourable than the interstitial mechanism because the size of gold and aluminium atoms are similar (Li, 1994).

Elevated temperature accelerates lattice diffusion because many vacancies are thermally activated. The temperature required to induce lattice diffusion in a material is generally higher than half of the melting temperature of the material.

2.6.4 Dislocation Pipe Diffusion

Dislocations are line defects in lattice structures so that the dislocation pipe mechanism is also called a line defect mechanism. Lattice disorder around a dislocation core provides loosely packed paths that allow atoms to diffuse. A special example of diffusion paths is the vacancy pipe formation around cores of edge dislocations, like an atom-free pipe providing free diffusion paths.

Dislocation density is an important parameter in the diffusion processes dominated by the dislocation pipe mechanism (Li, 1994). Dislocation density increases when the lattice is under stress because more dislocation sources are generated. Dislocation density in a lattice, usually decreases if the material is annealed at high temperature.

2.6.5 Grain Boundary Diffusion

A grain boundary is the interface region separating two adjacent grains in a polycrystalline material (Serp, 2009). Therefore, grain boundaries are considered as planar defects in crystalline materials. At a temperature less than half the melting temperature of material, atomic diffusion in the lattice becomes progressively more difficult. On the other hand, atoms at grain boundaries are less closely packed than elsewhere i.e. large amount of vacancies exist along the boundaries.

Atoms or vacancies have greater mobility in grain boundaries. Beside temperature, grain-boundary orientation and grain size also influence the diffusion process. For instance, grain boundaries are likely to be oriented in the direction perpendicular to substrate surfaces during thin-film deposition. Therefore, atoms diffuse at higher rates along the grain boundaries in the direction of the film thickness. Total grain boundary region decreases when the grain size increases, so that diffusion is relatively difficult in crystals with large grain size. The grain size can be controlled by adjusting the maximum temperature and cooling rate during the heat treatment (Austin, 1961).

2.7 Hardness Properties of a Material

Hardness is a measure of a material's resistance to localize plastic deformation by small dent or a scratch. Quantitative hardness measurement has been developed over the years where a small indenter is forced into the surface of a material to be tested, under controlled conditions of load and rate of application. The depth or size of the resulting indentation is measured which in turn related to the hardness number. Soft material has large and deeper indentation and lower hardness index number. Measured hardness is only relative rather than absolute (Tabor, 2000).

Hardness test is performed more frequently than any other mechanical test due to several reasons;

1. It is simple and inexpensive test.
2. The test is non-destructive.
3. Other mechanical properties may be estimated from hardness data, such as tensile stress.

There are several hardness test methods, namely Rockwell hardness test, Brinell hardness test, Knoop and Vickers micro hardness test. The Vickers micro hardness test method consists of indenting the test material with a diamond indenter, in the form of a right pyramid with a square base and an angle of 136° between the opposite faces subjected to a test load. The full load is normally applied for 5 to 10 seconds. The two diagonals of the indentation left on the surface of the material after removal of the load are measured using a microscope and their average is calculated to obtain the hardness value (Herrmann, 2011).

2.8 The Kirkendall Effect

In 1896, Roberts-Austen discovered that the atomic diffusion in metals could occur by direct exchange of atomic position as shown in Figure 2.8 (A) or by a ring mechanism in which the atoms exchange their positions by following a ring path as shown in Figure 2.8 (B).

However, in 1942, Kirkendall reported on a new diffusion theory, known today as the Kirkendall effect (Sequeira, 2014), explaining the interdiffusion between copper and zinc in a copper/brass system. The experimental data reported by Kirkendall supported the theory that atomic inter-diffusion at the interface of two metals occurs through a vacancy exchange mechanism as shown in Figure 2.8 (C).

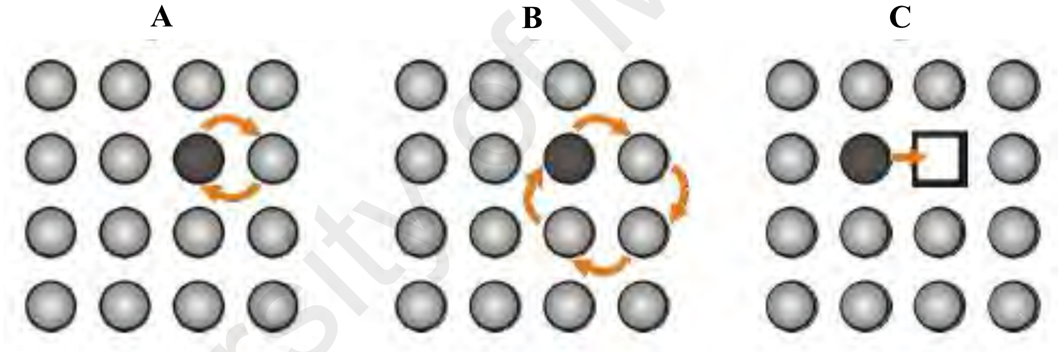

Figure 2.8: Atomic diffusion.

Despite the high importance of this discovery, at that time, it did not receive much attention. In April 1946, together with his student Smigelskas, Kirkendall submitted a manuscript to the editorial office of the Transactions of the AIME describing new results supporting the theory he had proposed four years before. Unfortunately, this manuscript was rejected by the referee (Mehl from the Carnegie Institute of Technology) who was convinced that the new diffusion mechanism proposed by Kirkendall was wrong.

In 1947, Smigelskas and Kirkendall succeeded in publishing their articles after including the criticisms and comments of Mehl in the comments and discussion section. In 1950, Mehl acknowledged the validity of the Kirkendall effect and one year later he and his student DaSilva published new data, validating the reproducibility of the Kirkendall effect for different metal alloys.

The Kirkendall effect describes that the motion of the boundary between two metals is due to a thermally activated, unbalanced diffusion (Paul, 2014). Upon annealing of two stacked on metal A and B, at a high temperature that sufficient to thermally activate the diffusion of atoms, atomic migration can occur at the interface where atoms will diffuse from metal A to B and vice versa as shown in Figure 2.9 (A).

Such an annealing process results in the formation of an A/B alloy layer located between the two sides of the interface. The final thickness is depending on both annealing temperature and time. According to Kirkendall effect, the position of the initial interface changes during the annealing process is different. This is due to different atomic diffusion coefficients of atom A in metal B and atom B in metal A.

As a consequence of the unbalanced diffusion rates between the two stacked metals, vacancies will be injected in the interface region within the faster diffusing metal. For example, if we consider that atom A diffuses in metal B much faster than atom B in metal A, the flux of atoms migrating from metal A to metal B (*J*A/B) will be much higher than atoms of B diffusing in the opposite direction (*J*B/A). In such case, the A/B alloy region will be more extended within metal B and vacancies will be injected in the interface region within metal A shown in Figure 2.9 (B).

The coalescence of an excess of vacancies leads to the formation of small voids distributed all along the interface. As the annealing process progresses in time, vacancies will be generated leading to the enlargement of the formed voids that will coalesce and form pores within the material shown in Figure 2.9 (C).

The voids formation in metals as a consequence of the Kirkendall effect can be considered as serious reliability issues in metallurgy (Zeng, 2005). The voids formation at the interface of two layers deteriorates the mechanical properties of the interface, resulting in poor adhesion and delamination between the layers.

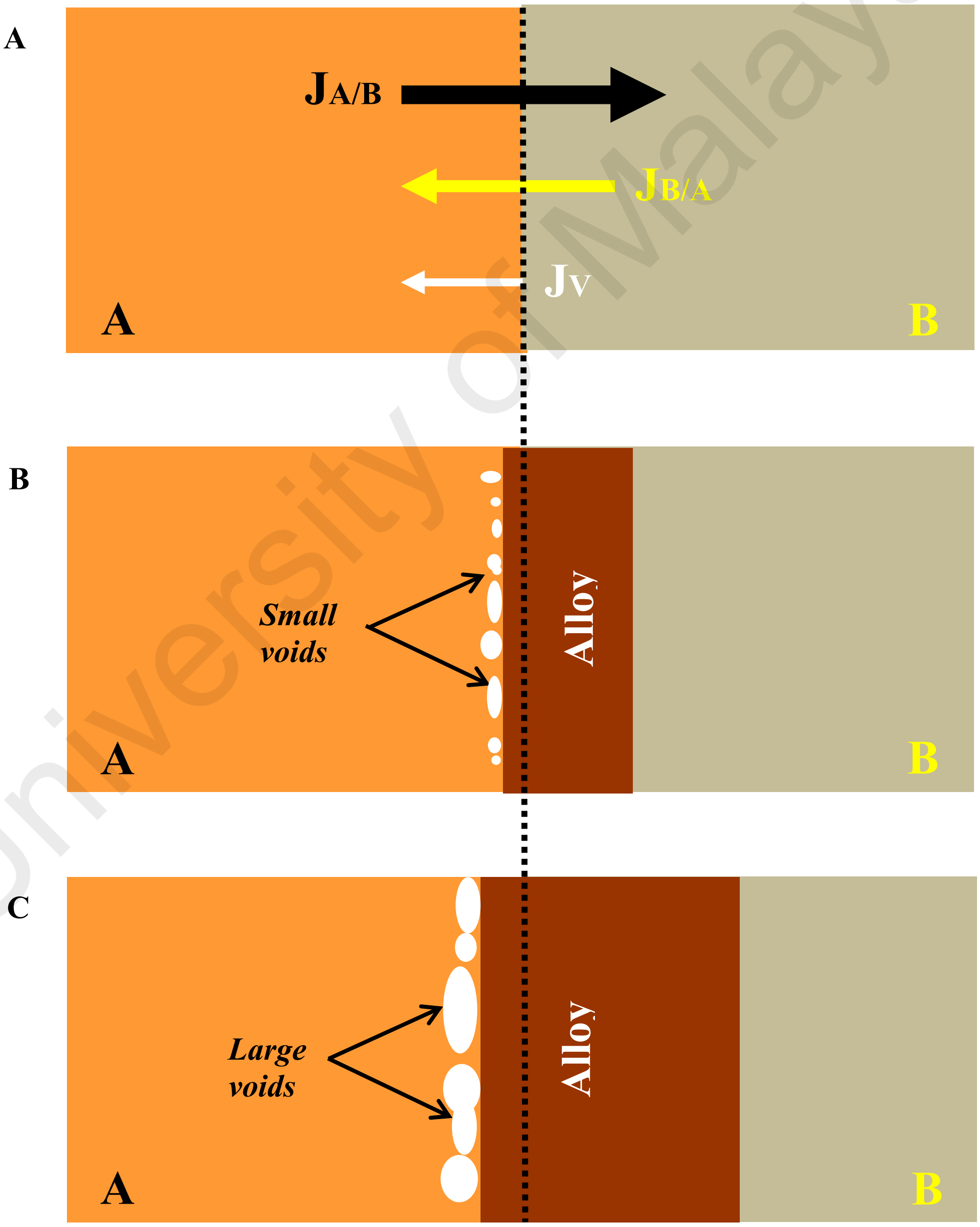

Figure 2.9: Formation of voids at the interface of two metals.

2.9 The Activation Energy – Arrhenius Reaction Rate Model

The Arrhenius Reaction-Rate Model is a mathematical expression that describes the effect of temperature on the velocity of a chemical reaction, the basis of all predictive expressions used for calculating reaction-rate constants. The Arrhenius equation predicts that a small increase in reaction temperature will produce a marked increase in the magnitude of the reaction-rate constant (Miura, 1998).

For a chemical reaction to occur, two or more molecules must come together and react. Most molecules in chemical reactions do not react every time a meeting occurs because of the enormous speed at which these molecules travel. It is necessary to slow these molecules down to allow a chemical reaction or to overcome the barrier to the reaction. Activation energy is the minimum quantity of energy that the reacting species must overcome in order to undergo a specified reaction (Peacock, 2012).

Each semiconductor device technology has its own activation energy. The energy of activation needs to be overcome for the reaction, and the speed of the reaction depends on the magnitude of the activation energy (Jernigan, 1994). If we wanted to know the change rate constant between two temperatures, knowing a value for the activation energy, we would assume that the value of A is constant and form a ratio

$$k = Ae^{\left(-E_a/RT\right)} \tag{3}$$

and the failure-rate form of the Arrhenius equation is

$$\lambda = Ae^{\left[-\frac{E_a}{k}\left(\frac{1}{T}-\frac{1}{T_o}\right)\right]} \tag{4}$$

where

λ = temperature-related failure rate,

R = universal gas constant (8.314 x 10^{-3} kJ/(mol·K),

A = rate constant,

E_a = activation energy,

k = 8.63 x 10^{-5} eV/K (Boltzman's constant),

T = temperature (K), and

T_o = reference temperature.

In general, the activation energy (E_a) is the factor that determined the slope of the reaction-rate curve with temperature as shown in Figure 2.10. This slope describes the accelerating effect of temperature on the rate of a reaction and is expressed in electron volts (eV). It is useful to describe the activation energy (E_a) as merely the slope of the curve, as opposed to a basic energy level. A low activation energy value indicates a small slope, or, in other words, a reaction that has a small dependence on temperature. A large E_a indicates a greater degree of temperature dependence (Connors, 1990).

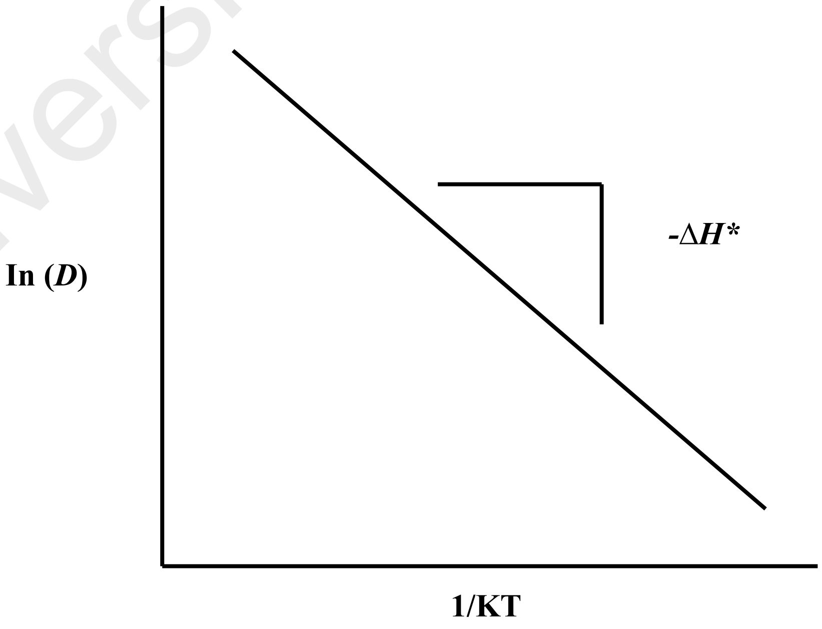

Figure 2.10: The Arrhenius plot.

In summary, there are two uses of Arrhenius curves:

1. To show specific time-temperature failure-rate effects of particular failure mechanism, and
2. To show general time-temperature failure-rate effects on the semiconductor device level. Each device type has particular failure mechanisms associated with it.

There are many different values of the activation energy (E_a) of copper oxidation that has been reported. Some of them are represented in Table 2.1.

Table 2.1: The activation energy of the copper oxidation.

Type of Copper	**Atmosphere**	**Temperature Range (˚C)**	**Activation energy *Qa* (kJ/mol)**	**Reference**
OFHC	0.1 Mpa O_2	300 - 550	84	Valensi, 1948
		550 - 900	158	
OFHC	Air	300 - 500	39	Tylecote, 1951
		600 -900	123	
99.999%	0.1 Mpa O_2 or Air	350 - 450	224	Park, 1993
		459 - 800	84	
99.9999%	0.1 Mpa O_2	300 - 500	40	Zhu, 2002
		600 - 800	111	
	Ar + 1%O_2	300 - 500	58	
		600 - 800	111	

2.10 The Effect of Heat Treatment Temperature to the Grain Size

The mechanical property of copper can be reverted to the pre-cold worked states by appropriate heat treatment. Such restoration results from two different processes that occur at elevated temperatures; recovery and recrystallization, which may be followed by grain growth.

2.10.1 Recovery

During recovery, some of the stored internal strain energy is released by virtue of dislocation motion, a result of enhanced atomic diffusion at the elevated temperature. There is some reduction in the number of dislocations, and dislocation configurations are produced having low strain energies (Davis, 2001).

2.10.2 Recrystallization

Even after recovery is completed, the grains are still at a relatively high strain energy state. Recrystallization is the formation of a new set of strain-free and equiaxed grains that have low dislocation densities and are characteristics of the precold-worked condition. The internal energy difference between the strained and unstrained bonding wire material will be the driving force to produce a new grain structure. New grains form as very small nuclei and grow until they completely replace the parent material, processes that involve short-range diffusion (Rollett, 2004).

During recrystallization, the mechanical properties that were changed because of cold working are restored to their pre-cold work values; that is, the metal becomes softer, weaker and yet more ductile. Recrystallization is a process which depends on both time and temperature. The degree of recrystallization increases with time (Hou, 2003). The influence of temperature is demonstrated in Figure 2.11 which plots tensile strength and ductility of metal as a function of the temperature for a constant heat treatment time of one hour. The grain sizes found on the various stages of the process are also presented schematically.

The recrystallization behaviour of a particular metal alloy is sometimes specified in terms of a recrystallization temperature, the temperature at which recrystallization has just reached completion in one hour. Typically, it is between one third and one half of the absolute melting temperature of a metal or alloy and depends on several factors, including the amount of prior cold work and the purity of the alloy (Fernández, 2000).

Increasing the percentage of cold work enhances the rate of recrystallization, with the result that the recrystallization temperature is lowered. Recrystallization proceeds more rapidly in pure metals than in alloys. Thus alloying raises the recrystallization temperature, sometimes quite substantially (Lalena, 2010).

2.10.3 Grain Growth

After recrystallization is complete, the strain-free grains will continue to grow if the metal specimen is left at the elevated temperature; this phenomenon is called grain growth. As grains increase in size, the total boundary area decreases, yielding a large reduction in the total energy, which is the driving force for grain growth. Grain growth occurs by the migration of grain boundaries. Thus, the average grain size increases with time and, at particular instant there will emerge a range of grain sizes (Cotterill, 1976).

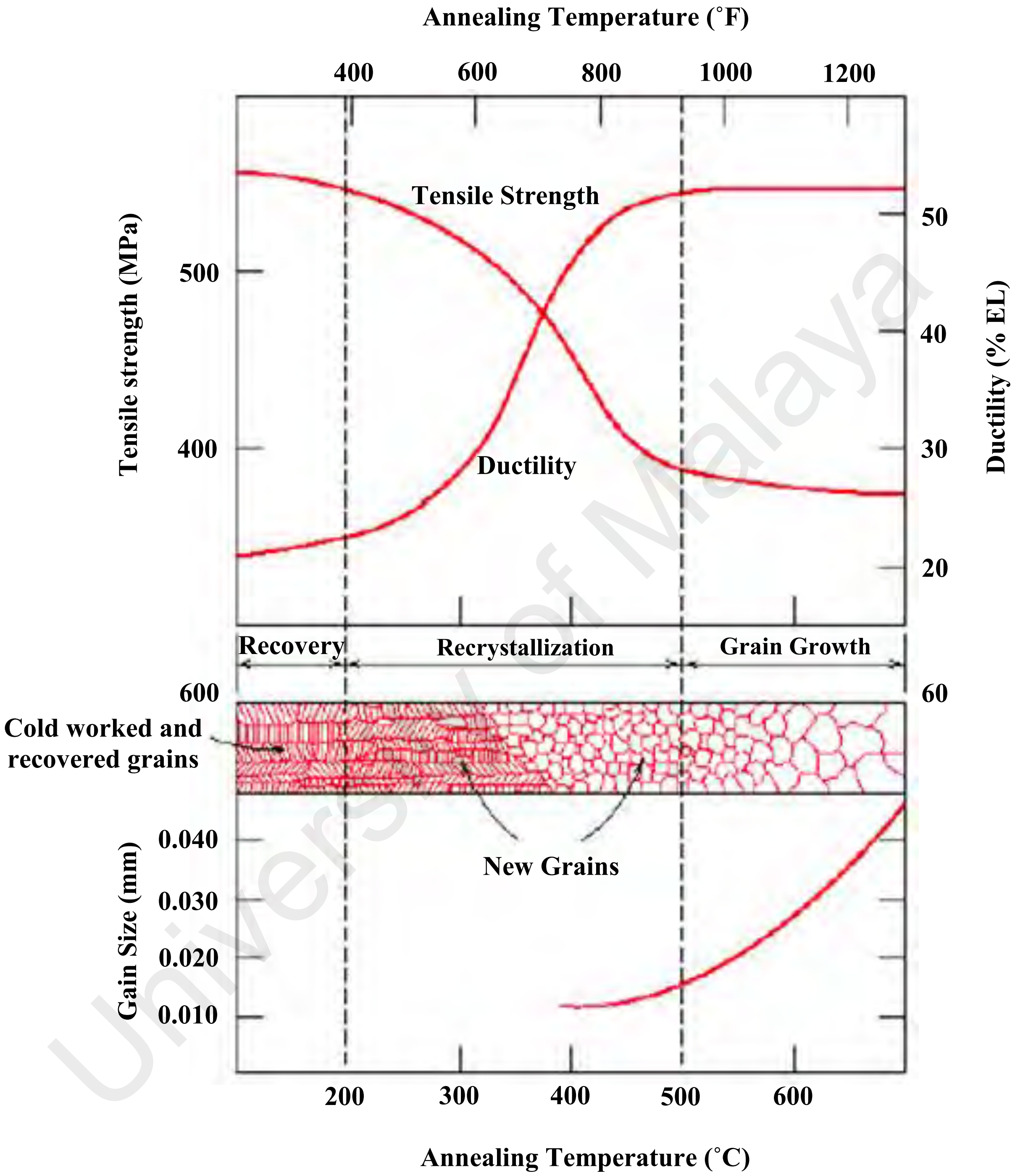

Figure 2.11: The influence of annealing temperature on the grain size.

CHAPTER 3: MATERIALS AND EXPERIMENTAL PROCEDURE

3.1 Analytical Tool

Various sophisticated analytical tools were used in this study. This section describes the principle of operation of each analytical tool. This includes high power optical microscopy, FESEM (Field Emission Scanning Electron Microscopy), AFM (Atomic Force Microscopy), Micro Hardness Tester, EDS (Energy Dispersive X-Ray Spectroscopy), AES (Auger Electron Spectroscopy), FIB (Focused Ion Beam), HRTEM (High Resolution Transmission Electron Microscopy) and EELS (Electron Energy Loss Spectroscopy).

3.1.1 High Power Optical Microscopy

The high power optical microscopy that was utilized in this study was a MX-61 model, manufactured by Olympus. The optical microscopy has three imaging techniques, namely bright field, dark field and interference contrast (Cahn, 2016). The bright field imaging technique provides the most uniform illumination on the sample. This technique was used to image the copper leadframe samples.

The optical microscopy has basic configurations such as a light source, objective lenses, an eyepiece and a stage for sample manipulations. The objective lens allows image magnification up to hundreds of times. However, the image resolution is very limited in the light microscopy (Andreoli, 2013).

The optical imaging is carried out by mounting the samples perpendicular to the axis of the objective lens. A full cone of a light source is then introduced to illuminate the samples. Some of the lights will be reflected back into the lens and translated to form an image by the output device. The image observed are the results from various levels of reflectivity exhibited by the topographical difference of the sample surface.

3.1.2 Field Emission Scanning Electron Microscopy (FESEM)

The FESEM model that was utilized in this study was S-4800, manufactured by Hitachi. In this system, the source of electron beams is produced by the cold FEG (Field Emission Gun) tip. During the FESEM imaging, the electron beams hits and raster's onto the sample surface. This interaction generates several secondary signals such as secondary electrons, backscattered electrons, x-rays, cathode luminescence and auger electrons. However, only secondary electron signals are collected by the detector and translated by the output device to form an image. Figure 3.1 represents the illustration of the electron-sample interactions (Huebschen, 2016).

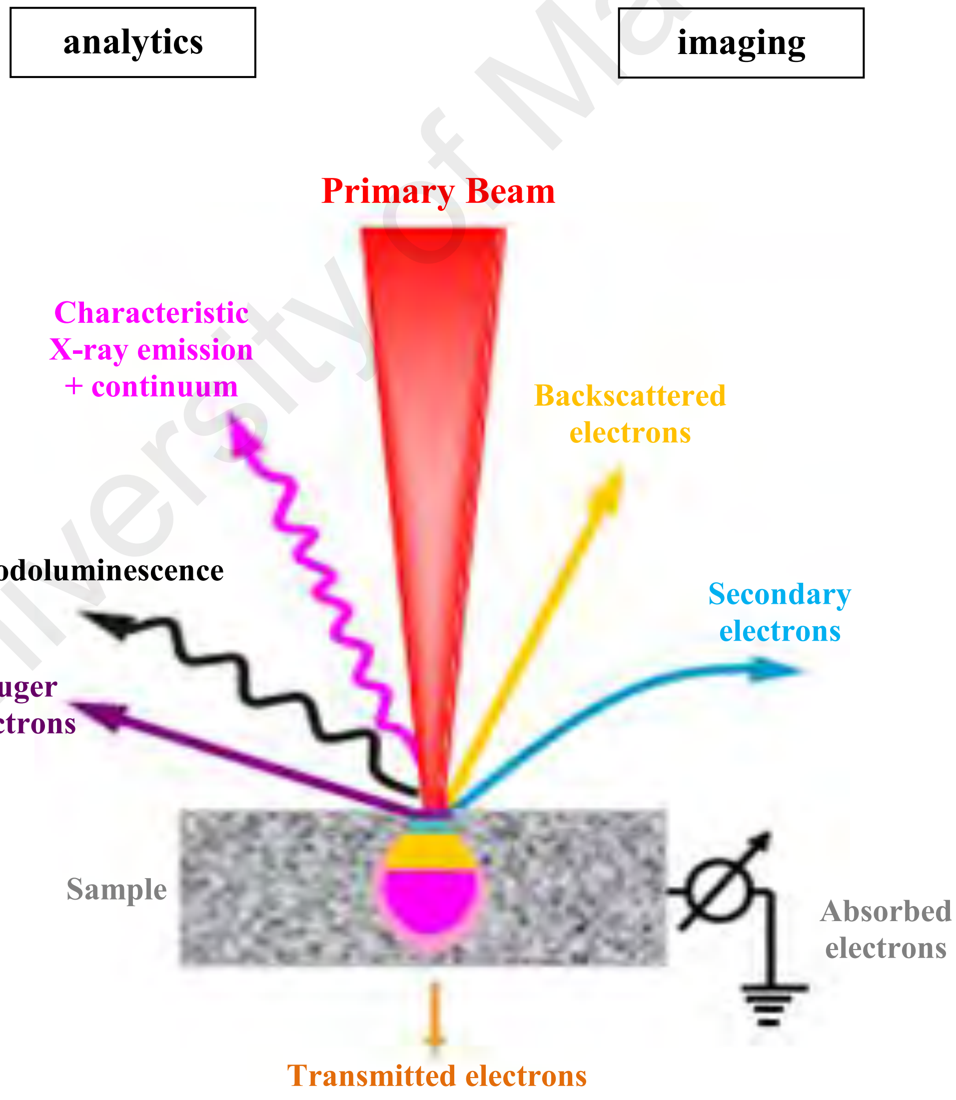

Figure 3.1: The electron-sample interactions on the sample surface.

In principle, the bombardment of the primary electron beams onto the sample surface generates elastic or inelastic scattering events. In inelastic scattering events, the electron beams collide and excites the electrons in a shell, ejecting it from the shell as the secondary electrons. These electrons lose significant amounts of energy during the collisions and therefore have low energy as it is escaping from the sample surface. The secondary electrons have the energy of 50 eV or less (Goldstein, 2012). The low energy of the secondary electrons carries the topographic information of a copper leadframe surface.

The FESEM system is equipped with the secondary electron detector to allow the detection of the secondary signals which generated during the electron-sample interactions. The secondary electron signals detected by the detector will be collected, amplified and translated by the output device to form an image.

The FESEM has the capability to provide a high resolution image which cannot be resolved by the optical microscopy. The electron beams as a source in the FESEM has a shorter wavelength, thus enable a high resolution power as compared to the light source in the optical microscopy (Morgan, 1949). The FESEM can achieve the resolutions of 1.0 nm and 1.4 nm at 15 kV and 1 kV respectively, while the image magnification can be magnified up to 300,000 of times.

Unlike the optical microscopy or the HRTEM, image magnification in the FESEM is not a function of the objective lens power. In the FESEM, the image magnification results from the ratio of the dimensions of the raster on the sample and the raster on the display device. The magnification is therefore controlled by the current supplied to the scanning coils or the voltage supplied to the deflector plates and not by the objective lens power.

3.1.3 Atomic Force Microscopy (AFM)

The AFM model that was utilized in this study was D3100 series, manufactured by Digital Instruments. There are three primary imaging modes in the AFM namely contact, non-contact and tapping modes (Schwarz, 2004). The surface roughness of the copper leadframe samples were analyzed using the tapping mode technique in the AFM.

In principle, the AFM is configured with a sharp tip mounted on a soft cantilever to interact with the sample surface. During the tapping mode operation, the sharp tip taps lightly on the sample surface. The cantilever is oscillated near to its resonant frequency. As the tip passes over a bump on the sample surface, the cantilever has less room to oscillate and the amplitude of oscillation decreases. Conversely, when the tip passes over a depression, the cantilever has more room to oscillate and the amplitude increases. A three-dimensional (3D) AFM image is then constructed by monitoring the motion of the tip as it is scanned over the sample surface. Figure 3.2 illustrates the principle of the AFM technique (Voigtländer, 2015).

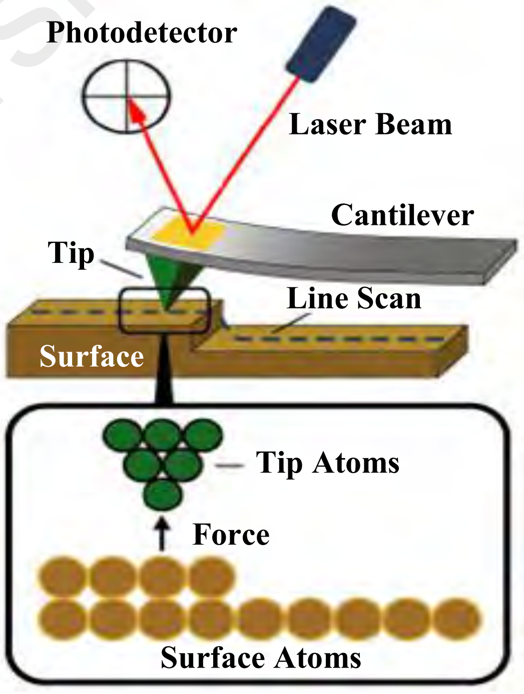

Figure 3.2: The principle of the AFM.

3.1.4 Micro Hardness Tester

The micro hardness tester model that was utilized in this study was HMV-2 series, manufactured by Shimadzu. This tool is used to measure the hardness of the samples (Hashmi, 2014). It has a Vickers tip for the indentation purpose, an eyepiece and an objective lens for the viewing purpose and a stage for the sample manipulation purpose.

During the hardness test, the sample is mounted onto the sample stage. The load is then applied to force the penetration of the Vickers tip onto the sample surface. The indentation mark left on the sample surface after the removal of the load determined the deformation resistance as well as the hardness of the sample. The Vickers tip has a diamond pyramid shape with a square base and has 136˚ angles between the opposite faces (Zhou, 2013). Figure 3.3 illustrates the Vickers indentation test.

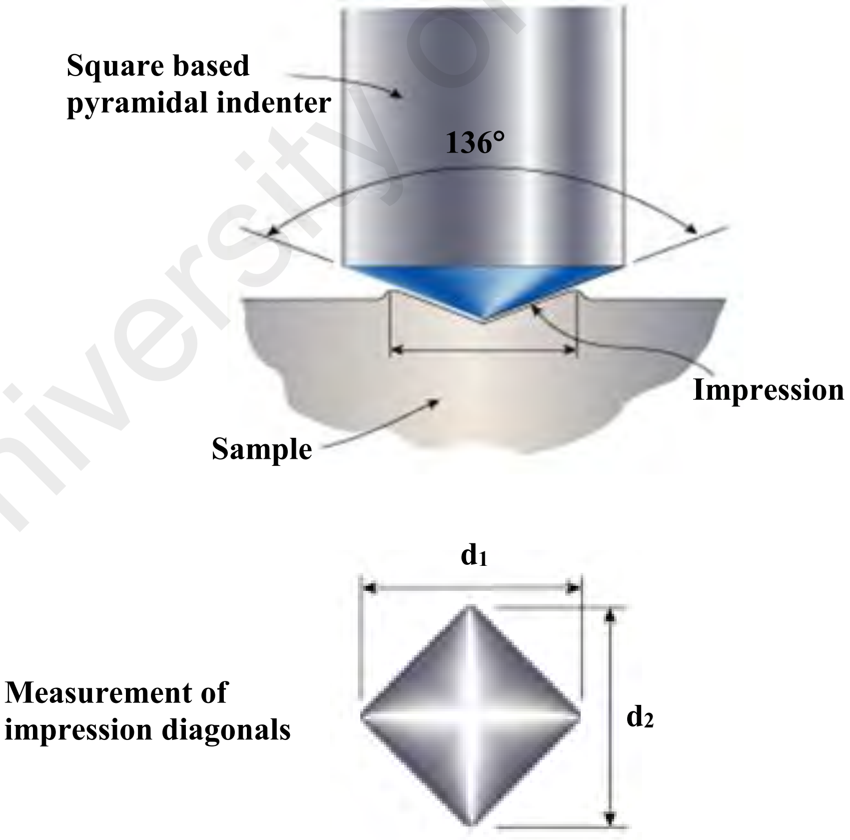

Figure 3.3: The Vickers hardness test.

3.1.5 Energy Dispersive X-ray Spectroscopy (EDS)

The EDS model that was utilized in this study was EMAX EX-350, manufactured by Horiba. The EDS system works together with the FESEM as an integrated system and cannot be operated on its own. The EDS analysis provides the elemental composition of the samples (Bell, 2003).

As discussed in section 3.1.2, the electron-sample interaction occurs as the electron beams hit onto the sample surface. The bombardment of the electron beams excites electrons in an inner shell, ejecting it from the shell while creating holes. This occurrence creates an unstable state of the atoms. The electrons from the outer shell have to fill up the holes in the inner shell to attain the energetic stable states. Since the electrons in the outer shell have higher energy state, it will lose some energy by emitting the x-rays. Figure 3.4 illustrates the principle of the x-ray emission (Jiles, 2008).

The amount of the energy emitted from the electron transfer depends on which shell its transfer from and to. Every element emits x-rays with unique amounts of energy during the transfer process. Therefore, the elemental identification in the EDS analysis can be done by measuring the amounts of the energy present in the x-rays emitted by the sample during the bombardment of electron beams (Russ, 2013).

The EDS analysis provides the spectrum as the output. It displays a corresponding peak to the energy levels of which the most x-rays have been received. Each peak unique to an atom and therefore correspond to a single element. The higher the peak in the spectrum, the more concentrated the element in the sample. The EDS has an energy resolution of 133 eV (Proulx, 2013).

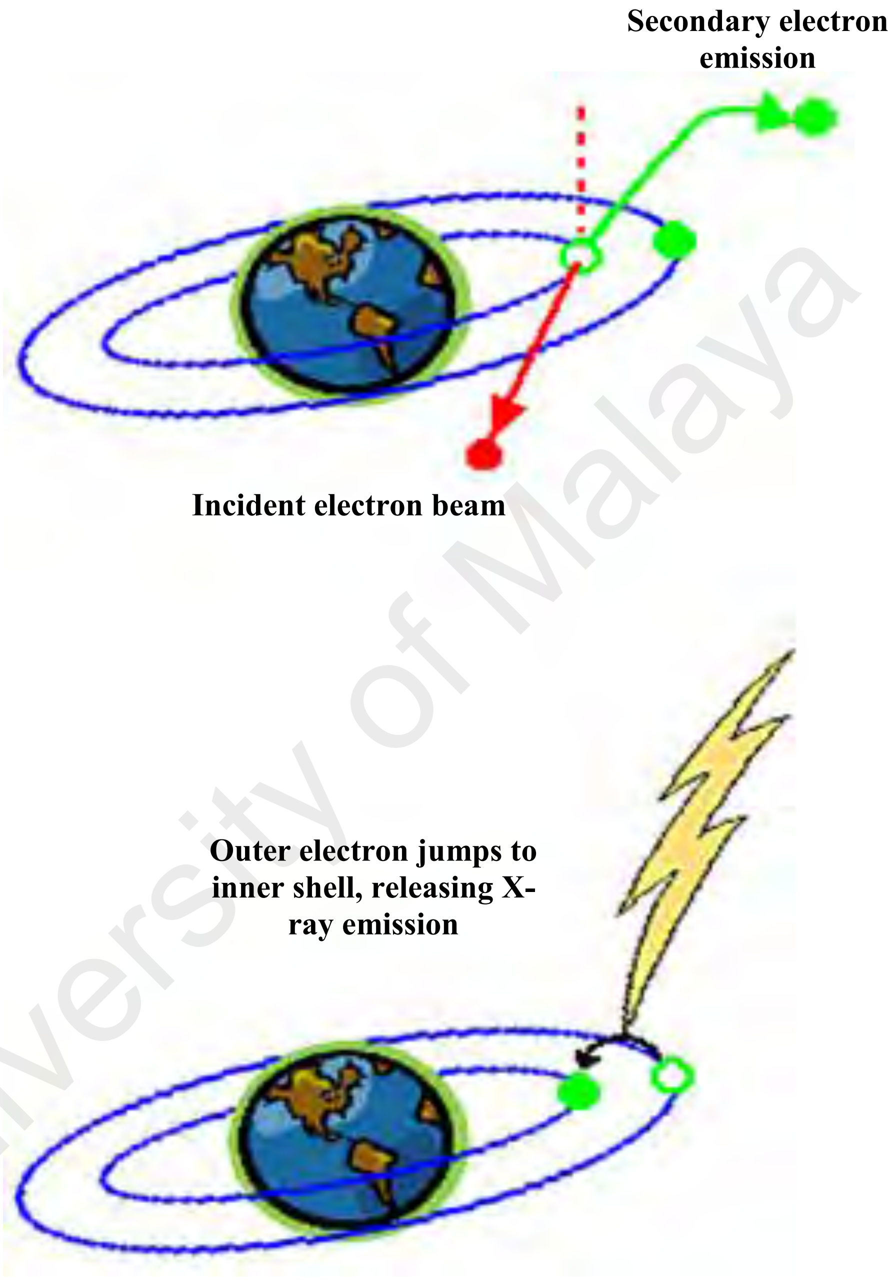

Figure 3.4: The principle of the x-ray emission.

3.1.6 Focused Ion Beam (FIB)

The FIB model that was utilized in this study was Strata 400S, manufactured by FEI. It has both electron and ion columns incorporated in the system. The electron column works similar to that of FESEM as discussed in section 3.1.2. While the ion column uses Gallium (Ga) as a liquid metal ion source (LMIS). Ga has several advantages over other liquid metals due to it has a lower melting point, excellent mechanical, electrical and vacuum properties and has a longer lifetime (Jain, 2017).

The main application of FIB is for micro sectioning at the specific area. This can be done by setting up a high ion beam current in the range of 0.46 nA up to 21 nA. As the ion beam current increases, the sputtering rate also increases, thus enable faster material removal for the micro sectioning purpose. The finely focused ion beam allows precise milling and finishing of the section. Figure 3.5 illustrates the ion-sample interactions on the sample surface (Orloff, 2009).

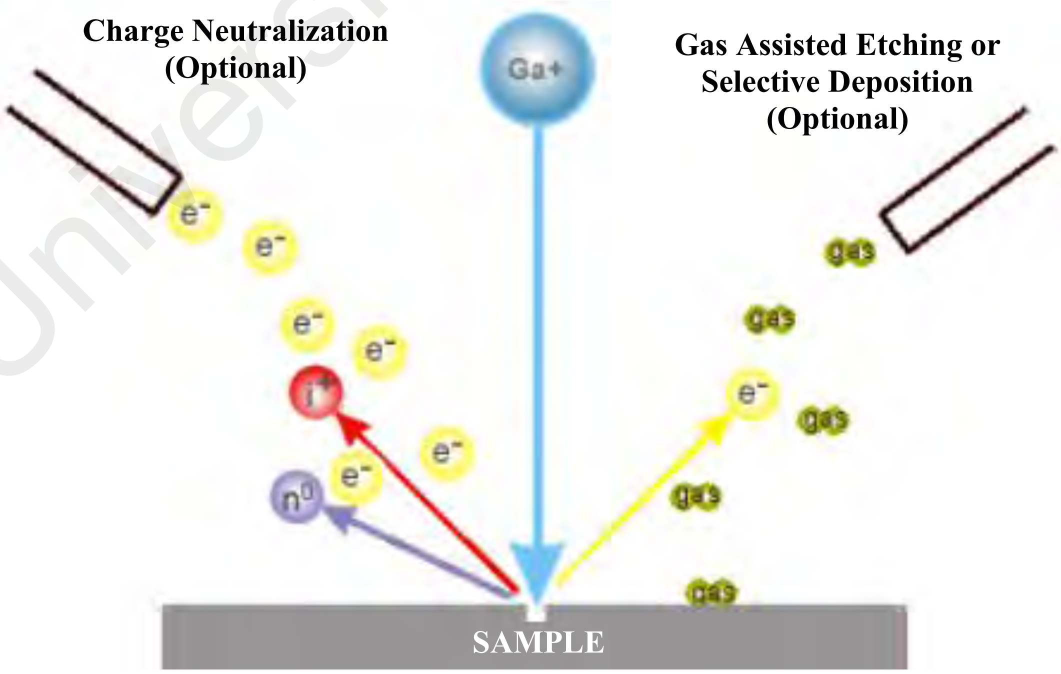

Figure 3.5: Ion-sample interactions on the sample surface.

The FIB system also equipped with a gas injection system (GIS). This enables material deposition to be done via electron or ion beam deposition. Strata 400S uses platinum (Pt) as a deposition material. The Pt deposition prior to the micro sectioning is required to protect the sample surface from the Ga ion bombardment. Without the Pt deposition, the Ga ions will be implanted down to 30 nm from the sample surface and destroyed the surface properties.

Strata 400S has an additional feature called omniprobe micromanipulator system. It consists of omniprobe needle to allow *in-situ* lift-out technique for TEM lamella sample preparation. The details of TEM lamella preparation are discussed in section 3.3.10.

3.1.7 High Resolution Transmission Electron Microscopy (HRTEM)

The HRTEM model that was utilized in this study was TECNAI G² F20 X-Twin, manufactured by FEI. In principle, the HRTEM works similar to the optical microscopy, however, in the HRTEM system, the electron beams are used as a source instead of the light (Buseck, 1989). For this model, the source of electron beams is produced by the Schottky FEG tip.

During the HRTEM operation, the electron beams are accelerated down to the sample at 200 kV. Hence, the electrons have a wavelength about a million times shorter than the light. This characteristic allows the HRTEM to offer higher resolution as compared to the optical microscopy or the FESEM. The HRTEM has a resolution of 0.2 nm at 200 kV and the image can be magnified up to 1 million of times (EDFAS, 2011).

A thin section of a sample, often called as a lamella with the thickness of less than 100 nm is required for the HRTEM imaging. This sample condition allows electron beams to pass through it (Bartos, 2004). In the HRTEM system, the electron beams illuminate the lamella with the aid of the condenser lens. Unlike in the FESEM whereby focused and scanning electron beams are used, the HRTEM uses broad and static electron beams. Figure 3.6 shows the electron-sample interactions of a thin section. There are three types of transmitted electrons that generated during the interactions, namely unscattered or transmitted beam, elastically scattered and inelastically scattered electrons (Padua, 2012).

The bright field and high resolution TEM imaging techniques were applied to image the copper oxide on the copper leadframe samples. In the bright field imaging technique, the image is formed using transmitted beam by intercepting the diffracted beams using a small objective aperture. On the other hand, the high resolution TEM image is formed using transmitted and several diffracted beams by introducing a larger objective aperture (Williams, 1996). In the HRTEM, the image is captured using the CCD (Charged Coupled Device) camera.

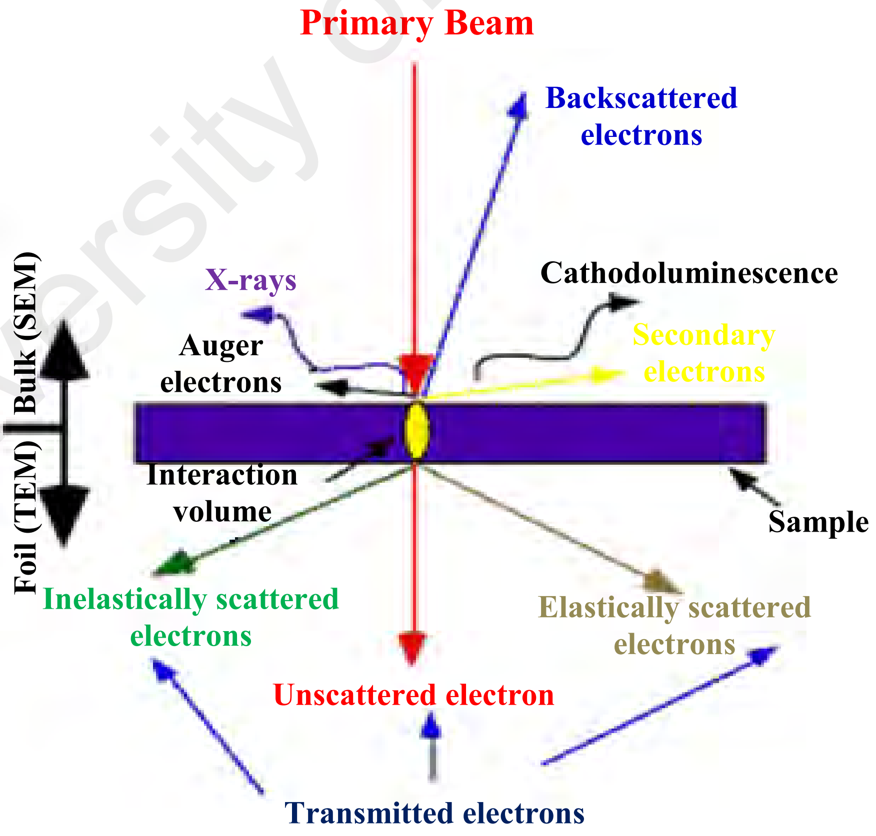

Figure 3.6: Electron-sample interaction on the thin section.

3.1.8 Selected Area Electron Diffraction (SAED)

A diffraction pattern can be one of the useful information of a solid. The diffraction pattern is typically represented as a series of periodic spots or rings. The crystal orientation of a crystalline material can be determined using the diffraction analysis (Schulz, 2005).

The diffraction pattern is acquired under broad and parallel electron beams illumination. An aperture in the image plane is used to select the diffracted region of the sample, giving site-selective diffraction analysis. The SAED patterns are the projection of the reciprocal lattice. The lattice reflections represent as sharp diffraction spots. Figure 3.7 shows the example of the SAED pattern of Cu_2O (Fujita, 2013).

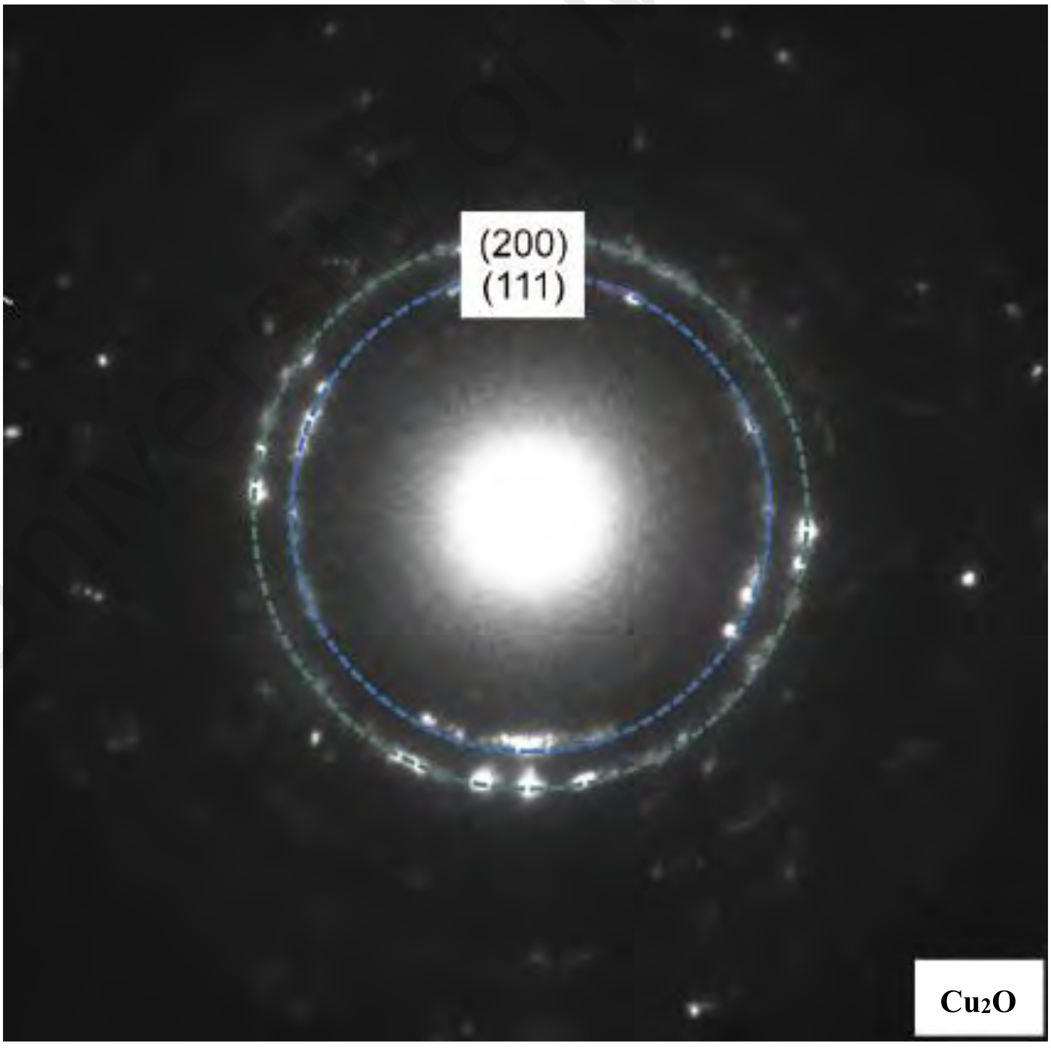

Figure 3.7: SAED pattern of Cu_2O.

3.1.9 Electron Energy Loss Spectroscopy (EELS)

The HRTEM offers an analytical characterization of a material through Electron Energy Loss Spectroscopy (EELS) analysis techniques. The EELS analysis is capable to provide the bonding information of a material due to edge shape caused by the transferred kinetic energy (Nogi, 2012). This technique was performed to determine the oxidation states of the copper oxide.

Figure 3.8 illustrates the configuration of the post column spectrometer of the EELS. During the EELS analysis, the electron beams pass through an entrance aperture, and then deflected by 90 ° angle and dispersed according to their energy loss by a magnetic prism. If the electrons have more energy loss, the deflection will be stronger. The magnetic prism also acts as a magnetic lens, where it focused electrons that travel on and off-axis of the dispersion plane. The electrons with different energy will be separated and will be sent to the corresponding collecting channels for further processing. The outcome of the analysis is the EELS spectrum (Ahn, 2006).

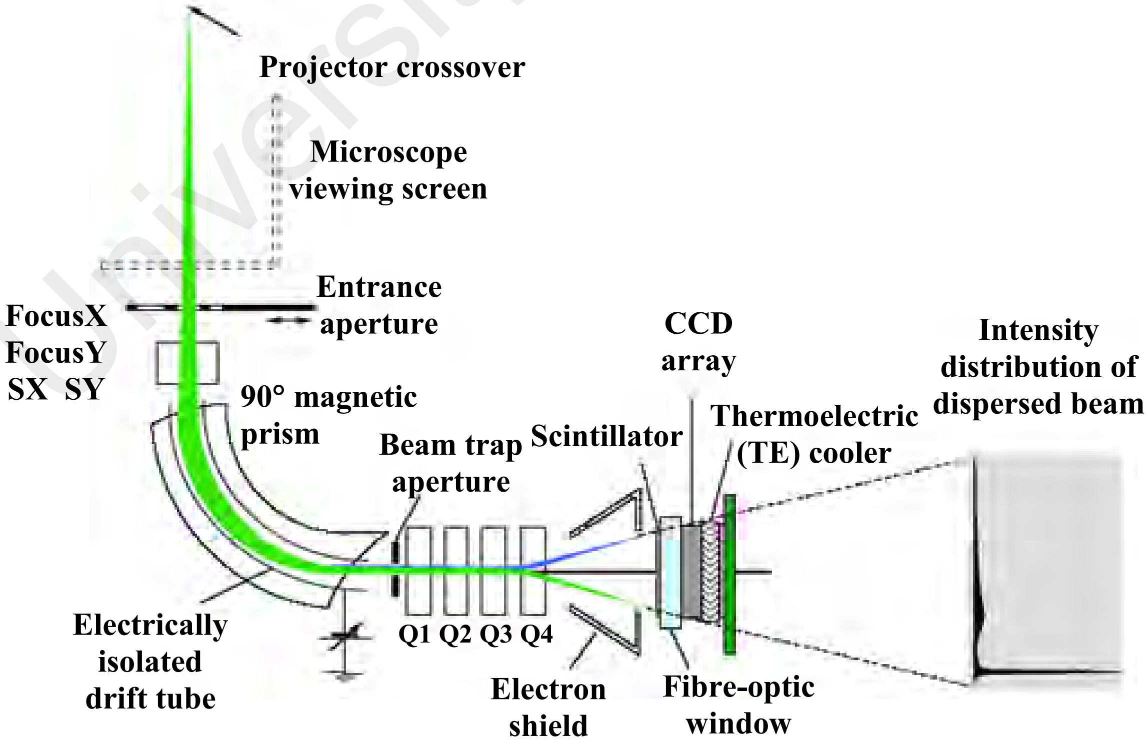

Figure 3.8: The configuration of EELS post column spectrometer.

The EELS spectrum consists of three regions; zero loss peak, low loss and high loss regions as illustrated in Figure 3.9. The zero loss peak is located at 0 eV in the EELS spectrum. It contains the original energy of the electron beams, where it may interact elastically or not at all during collisions with the lamella. The width of the zero loss peak determines the energy resolution of the EELS analysis (Nellist, 2011).

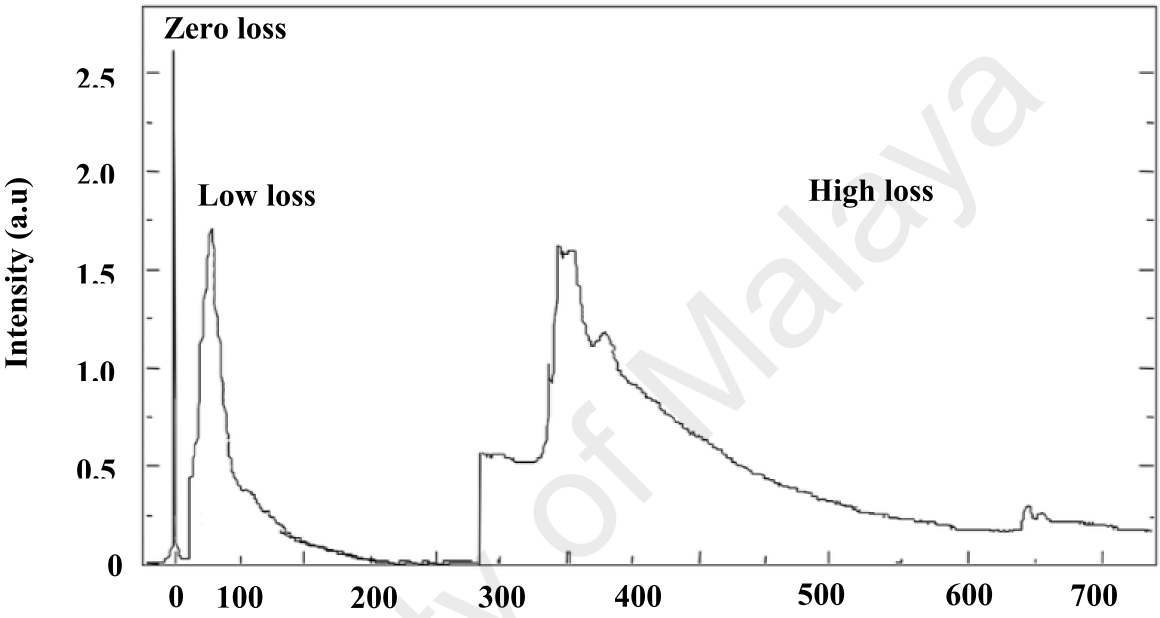

Figure 3.9: The EELS spectrum.

In the EELS spectrum, the low loss region covered an area below 100 eV. Typically, a low loss region consists of a Plasmon peak. In the EELS spectrum, the Plasmon peak always presence except for the ultra-thin lamella. Thus, this region can be used to estimate the lamella thickness. However, thick lamella will generate a multiple Plasmon peak and makes the interpretation difficult (Henderson, 2014).

The high loss region covered an area above 100 eV in the EELS spectrum. It reflects the inelastic scattering of electron beams and lamella during the collisions. The amount of the energy loss is unique for each element and therefore it generates unique EELS spectrum for each element or chemical bonding (Geiger, 2001). However, a standard EELS spectrum is required for elements or chemical bonding identification. Typically, the edges and profile of the EELS spectrum collected from the analysis will be compared with the EELS library for identification (Ahn, 1983).

3.1.10 Auger Electron Spectroscopy (AES)

The AES model that was utilized in this study was JAMP-9500F, manufactured by JEOL. The AES system consists of the FESEM column, ion gun, energy analyzer and a sample stage. The FESEM column in the AES works similar to the FESEM system as discussed in section 3.1.2. In the AES system, the primary electron beams is produced by the Schottky FEG.

In principle, the auger process occurs as the bombardment of the electron beams excites electrons in an inner shell, ejecting it and leaving holes. This process creates an unstable state of the atoms. The inner shell vacancy is then filled by the electrons from the higher shell. Since the electrons in the highest shell have higher energy state, a third electron will be released to attain the energetic stable state as an auger electron. The Auger process is similar to the x-ray process, however, the Auger process involved the third electron released at different subshell as illustrated in Figure 3.10 (Carlson, 2013).

The Auger electrons can only escape from the outer 6 nm of a solid surface, these characteristics make the Auger analysis as an extreme surface sensitive tool for a material characterization. In the Auger analysis, the element is determined by the kinetic energy and the intensity of the Auger peak (Vij, 2007).

The Auger system typically integrated with the Ar ion etching device to allow charge neutralization of charging sample as well as for micro etching for a depth profile analysis. The Auger depth profiling provides the elemental distribution as a function of depth by alternately acquiring a spectrum and ion sputtering. This technique allows the thickness determination of a layer by measuring the depth of the profile, however, the accuracy of the thickness is influenced by the etching rate (Marcus, 2005).

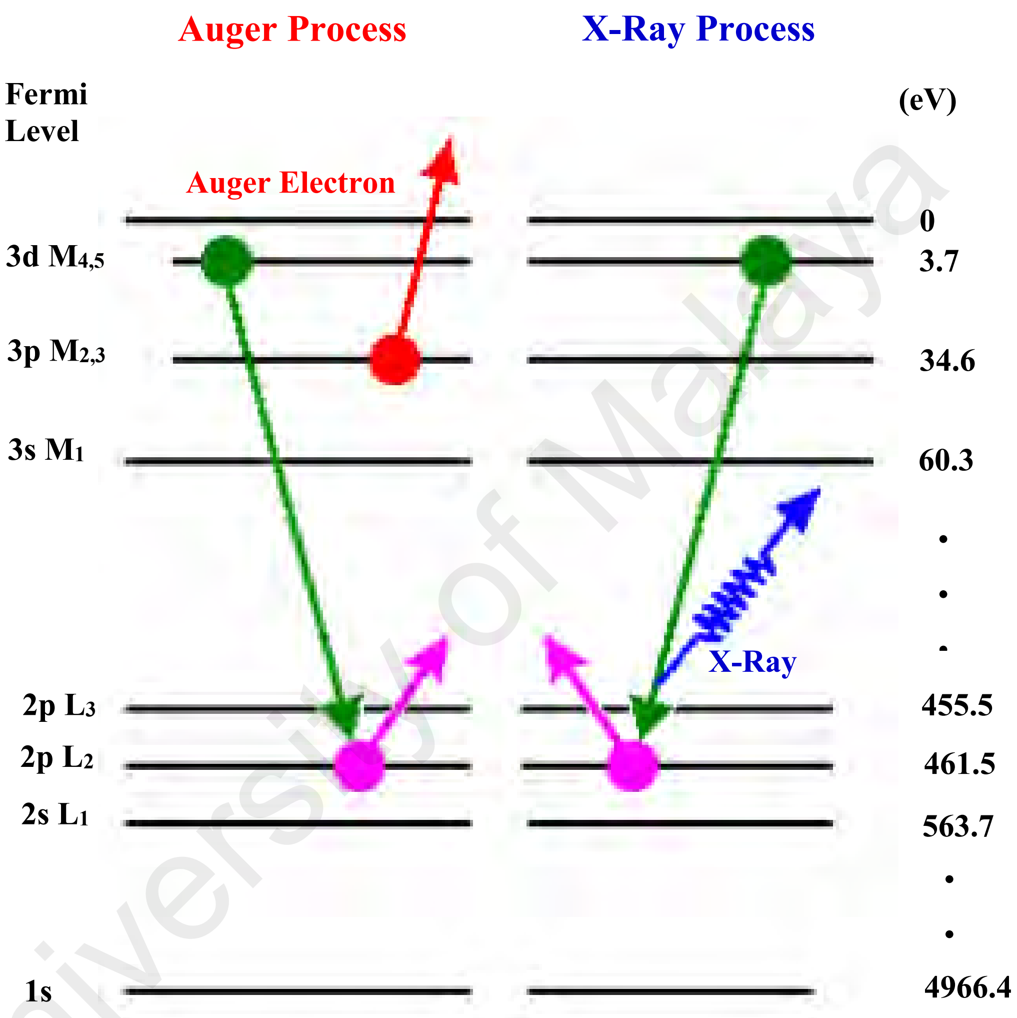

Figure 3.10: Comparison of Auger and X-ray process.

3.2 Sample Preparation

In this study, a commercial copper alloy leadframe material was used. It has a weight composition of 97.05 % copper (Cu), 2.6 % iron (Fe), 0.15 % phosphorus (P) and 0.2 % zinc (Zn). It was cold worked during the leadframe fabrication process in Jade Precision Engineering Pte Ltd production line in Singapore.

3.2.1 Heat Treatment of Copper Alloy Leadframe

The copper alloy leadframe was cut into small pieces as shown in Figure 3.11. No pre-treatment or pre-cleaning were carried out prior to the experiment. As-received copper alloy leadframe sample was used as a control sample in this study.

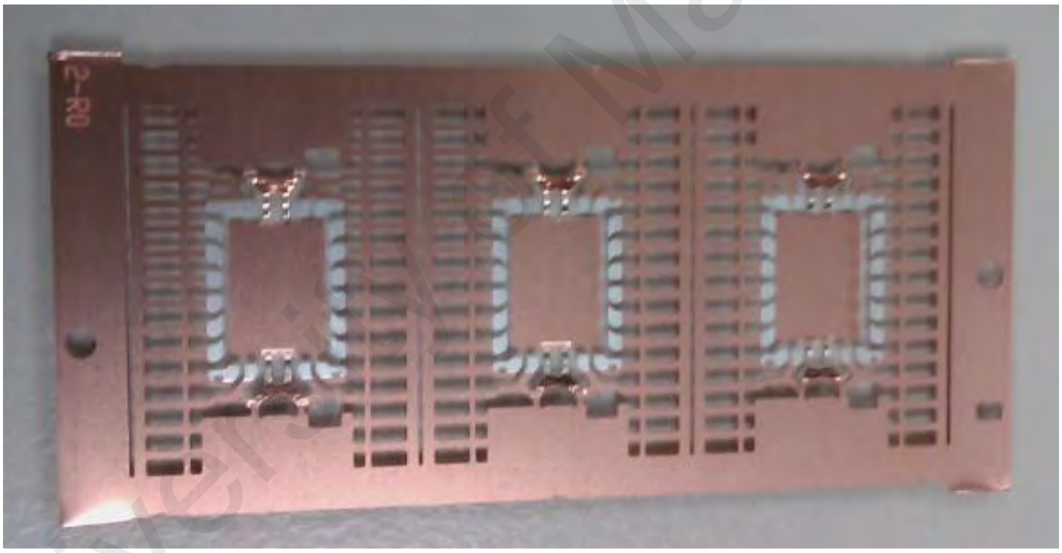

Figure 3.11: The As-received copper alloy leadframe sample.

The oxidation of the copper alloy leadframe sample was introduced via a heat treatment process in an oven under oxygen environment to promote the oxidation process. The heat treatment temperature was varied at 30 °C intervals at the temperature ranging from 60 °C up to 240 °C for 3 hours. There were a total of 8 samples in this research work. Table 3.1 tabulated the list of the evaluation samples.

Table 3.1: The list of the evaluation samples.

Sample No.	**Temperature (˚C)**	**Duration (Hours)**
1	As-received	Not Applicable
2	60	3
3	90	3
4	120	3
5	150	3
6	180	3
7	210	3
8	240	3

3.3 Experimental Procedure

This section describes the experimental procedure that has been carried out to characterize the copper alloy leadframe samples.

3.3.1 Observation of Colour Change

Upon the heat treatment process, the colour change of the copper alloy leadframe samples was recorded and the image was captured using the optical microscopy by applying the bright field imaging technique. During the optical imaging, the exposure time was set to 1.5 ms to maintain the actual colour of heat treated copper alloy leadframe samples. The optical images were taken at 5, 10 and 20 times of magnification for each of the evaluation samples.

3.3.2 Surface Texture Investigation

The surface texture of the heat treated copper alloy leadframe samples was investigated using the FESEM system. Prior to the FESEM inspection, the samples were coated with AuPd for 100 seconds to avoid the charging and the carbon contamination effect on the sample surface. During the FESEM inspection, the acceleration voltage was set to 5 kV with 10 nA current setting while mix detector was selected to obtain a better surface texture effect in the FESEM micrograph. The FESEM micrographs were taken at 5 kx, 10 kx, 20 kx, 50 kx and 100 kx times of magnification for each of the evaluation sample.

3.3.3 Surface Morphology Investigation

The surface morphology of the heat treated copper alloy leadframe samples was investigated using the AFM by applying the tapping mode technique. The scanned area was set to 5 µm by 5 µm with the scan rate of 1 Hz and a tip velocity of 10 µm per second. The 3D image of the surface roughness was constructed and the RMS value was calculated using the AFM software.

3.3.4 Hardness Test Measurement

The hardness test measurements were carried out using micro hardness tester with at least 10 of indentation points were performed on the heat treated copper alloy leadframe samples. The applied load was 980.7 mN, which was the lowest load possible for this tool. This is to ensure less interference of the bulk copper alloy leadframe and to obtain a better accuracy of the copper oxide hardness measurement on the sample surface.

The indentation time was set to 5 seconds for each indentation point. The indentation marks on the sample surface were imaged using the FESEM system. The two diagonal lengths of the indentation marks were measured using the FESEM software. The hardness value of the copper oxide was then measured using the mathematical calculation as below;

$$HV = \frac{0.1891F}{d^2} \tag{5}$$

where

HV is Vickers Hardness with no units

F is the applied force in Newton

d is the average diagonal length of indentation mark in millimeters

3.3.5 Grain Size Measurement

There are two areas of interest for the grain size measurement of the heat treated copper alloy leadframe samples which includes the surface grains and the bulk grains. The surface grains were investigated to understand the changes of the copper grain size on the sample surface after the heat treatment process while the bulk grain size was investigated to understand the effect of the temperature to the bulk properties of the copper alloy leadframe samples.

The surface grains of copper alloy leadframe were revealed by the FIB system. The sample surface was exposed to the Ga ion in the FIB system until the copper grains were visible. The secondary ion images were captured to record the copper grain. The images were acquired at five different locations.

The bulk copper grain was revealed by performing site-specific cut with the dimension of 30 μm by 20 μm with the depth of 10 μm. The platinum deposition took place prior to FIB cut analysis to protect the sample surface from the Ga ion beams bombardment. The cross sectional view of the samples revealed the bulk grains of the copper alloy leadframe samples.

The average of the copper grain size measurement was carried out using the intercept counting method as described in the American Society for Testing and Material (ASTM) E 112 standard (Thorvaldsen, 1997). The method of the grain size measurement is illustrated in Figure 3.12.

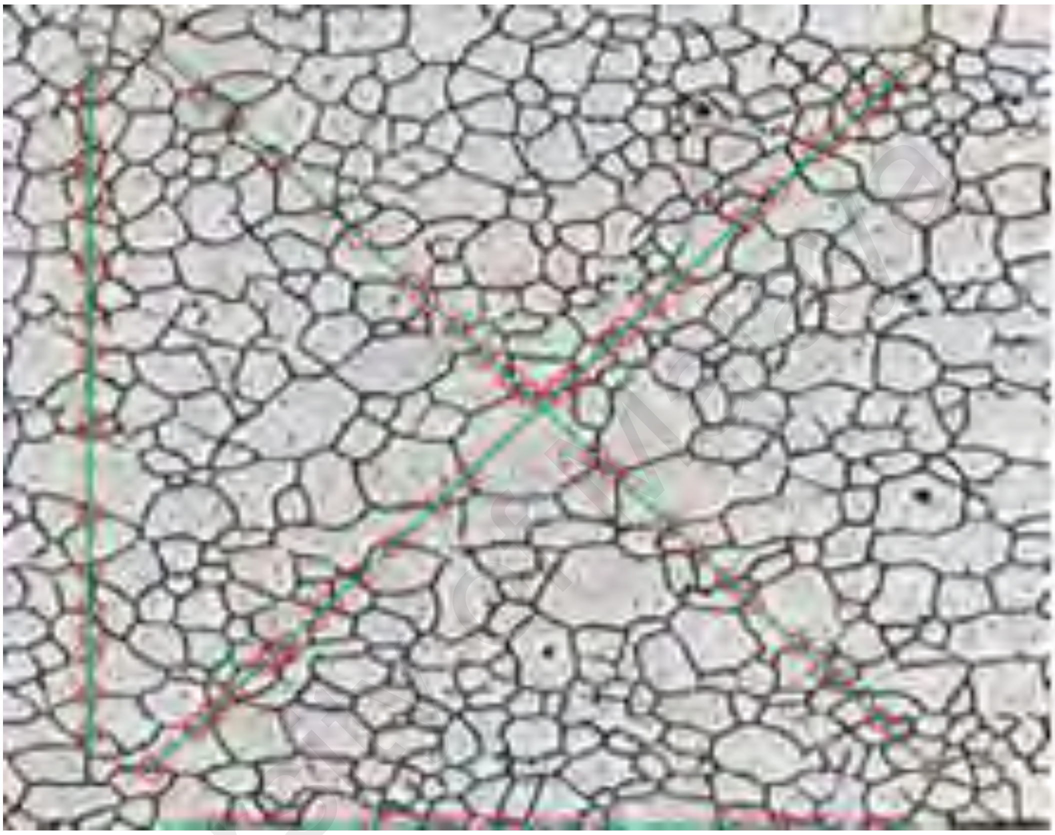

Figure 3.12: The intercept counting method according to ASTM E 112 standard.

3.3.6 Elemental Analysis using FESEM

The EDS analysis in the FESEM system was carried out to determine the elemental composition of the copper alloy leadframe samples. The acceleration voltage was set to 5 kV with 10 nA current settings. The EDS analysis is a bulk analysis since the EDS signal might be detected down to few micron ranges.

An area EDS analysis with a dimension of 5 µm by 5 µm was defined for each sample. The acquisition time was fixed at 200 seconds. The dead time was maintained within 20 % to 30 % during the EDS acquisition. This is important to ensure that the

EDS spectrum is acquired at the optimum condition. The interpretation of the EDS spectrum and the quantification analysis were performed using the EMAX software. The copper oxide on the sample surface was quantified in the atomic percentage.

3.3.7 Elemental Analysis using TEM

The EDS elemental mapping was performed in the cross section view of the copper alloy leadframe sample to obtain the elemental distributions of the copper and oxygen elements. The elemental mapping was carried out in an area of 200 nm by 250 nm in the cross section view of the sample.

The line profile analysis was also carried out in the cross section view of the sample with the line scan length of 300 nm across the bulk copper and the copper oxide layer. The line profile result was plotted in the atomic percentage.

3.3.8 Oxidation State Analysis using TEM

The oxidation state analysis was performed using the EELS point analysis in the cross section view of the sample. The EELS analysis was also carried out on the bulk copper for a reference. The EELS atlas was used as a reference to confirm the oxidation states of the copper oxide.

3.3.9 Depth Profiling Analysis

The AES depth profiling analysis was carried out to determine the depth information of the copper oxide on the surface of the copper alloy leadframe sample. This is a destructive technique as it involved a material removal through a micro etching process. The AES depth profiling analysis was carried out at 2000 eV by Ar ion sputtering at the acceleration voltage of 10 kV and 10 nA current. The etching rate was 21.9 nm per minutes with reference to that of SiO_2 as a standard. The copper and oxygen elements were included in the AES depth profiling analysis. The AES software investigator was used to interpret the AES depth profiling results.

In the AES depth profiling result, the thickness of the oxide layer was estimated by taking the 50 % intersection of the total atomic density as shown by the dotted line in Figure 3.13.

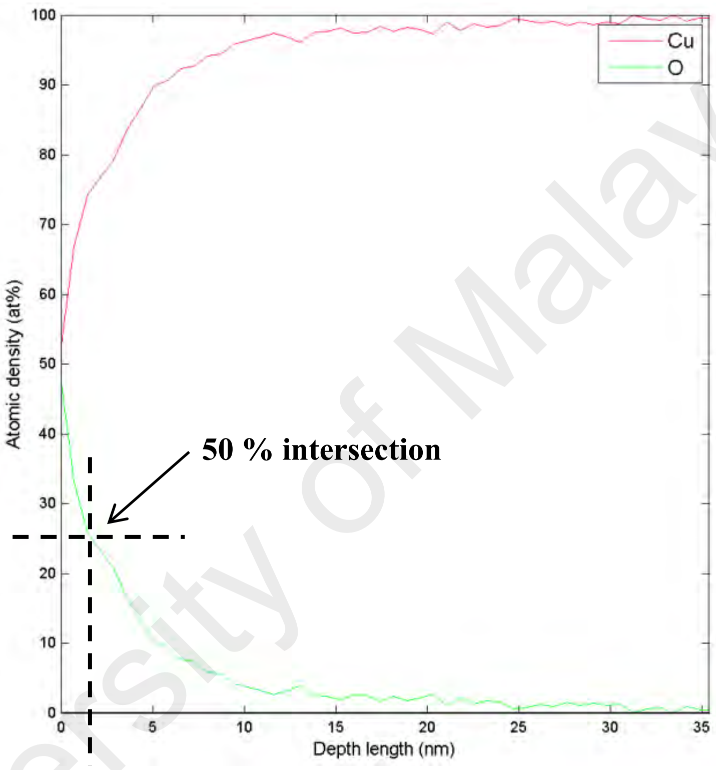

50 % intersection

Figure 3.13: The estimation of the layer thickness.

3.3.10 TEM lamella preparation

As discussed in section 3.1.7, prior to the HRTEM investigation, a thin section of a sample called as a lamella has to be extracted from the heat treated copper alloy leadframe sample. As part of the TEM requirement, the lamella has to be transparent to the electron beams where the thickness is less than 100 nm. This sample condition allows the electrons to pass through it. The TEM lamella sample was prepared by an *in-situ lift-out* technique using the FIB system.

Figure 3.14 shows the TEM lamella preparation steps. The details of the TEM lamella preparation process is described as the following:

1. **Auto TEM** – This is the automated preparation step where the pre-define FIB cut recipe is used to set-up the lamella. Prior to the Auto TEM, two layers of Pt depositions will be deposited onto the sample surface. The first Pt layer is the electron induced platinum deposition where it protects the sample surface from the Ga ion beams exposure. The electron induced Pt deposition is a very slow process and only thin layer can be produced. Therefore the second protection layer which is induced by the ion beams has to be deposited in the same area for more optimum surface protection. During the Auto TEM preparation, the bulk materials will be removed on both sides of the targeted area and left over a membrane-like sample. At this preparation step, the lamella thickness is approximately 1 μm.
2. **U-cut** – This step is required to free the lamella from the bulk sample. A small portion of the sample is reserved during the U-cut process to secure the lamella to the bulk sample.
3. **Insert omniprobe and Pt deposition needle** – Upon the completion of the U-cut, the omniprobe and the Pt deposition needle will be inserted.
4. **Attach omniprobe and cut the lamella free** – The omniprobe needle is attached to the lamella by the Pt deposition. Once the lamella is firmly attached onto the omniprobe needle, the U-cut step is continued to completely free the lamella from the bulk sample.
5. **Lift-Out** – The Lift-out procedure is required to move the lamella away from the bulk sample. This procedure is performed by adjusting the omniprobe needle to the upwards position.
6. **Molybdenum (Mo) Grid** – The Mo grid is used as a sample holder for the TEM lamella. The Mo Grid has three fingers and labelled as A, B and C. This labelling

helps in the TEM lamella identification in the TEM system if more than one lamella is attached onto the grid.

7. **Attach Lamella to Mo Finger** - The lamella is then brought closer to the grid and is attached to one of the grid fingers by the Pt deposition. As this step completed, the omniprobe needle is cut-off and is retracted away from the lamella.
8. **Final Thinning** – In this step, the TEM lamella is thinned down to less than 100 nm using low Ga ion beam current on both side of the lamella. As the desired thickness is achieved, the low kV cleaning step at 5 kV and 2 kV are performed to reduce the amorphous layer on both sides of the lamella. This step is very crucial, especially for the high resolution TEM and EELS analysis. The lamella is then ready for the TEM inspection.

3.3.11 Copper oxide properties and thickness measurement

The properties of the copper oxide on the heat treated copper alloy leadframe samples were investigated using the TEM bright field and atomic resolution imaging techniques. The interface of the copper to copper oxide was also studied in details. The atomic resolution analysis in the HRTEM is required to determine if the copper oxide has a crystalline or amorphous structure. This will also further confirmed by the SAED analysis.

The copper oxide thickness measurement was performed using the HRTEM. The copper oxide thickness was measured on the TEM image by taking an average of 10 points of measurements. The Digital Micrograph software was then used to assist in the thickness measurement.

The activation energy (E_a) of the samples was then determined by the slope of the reaction-rate curve with temperature based on the Arrhenius reaction rate model.

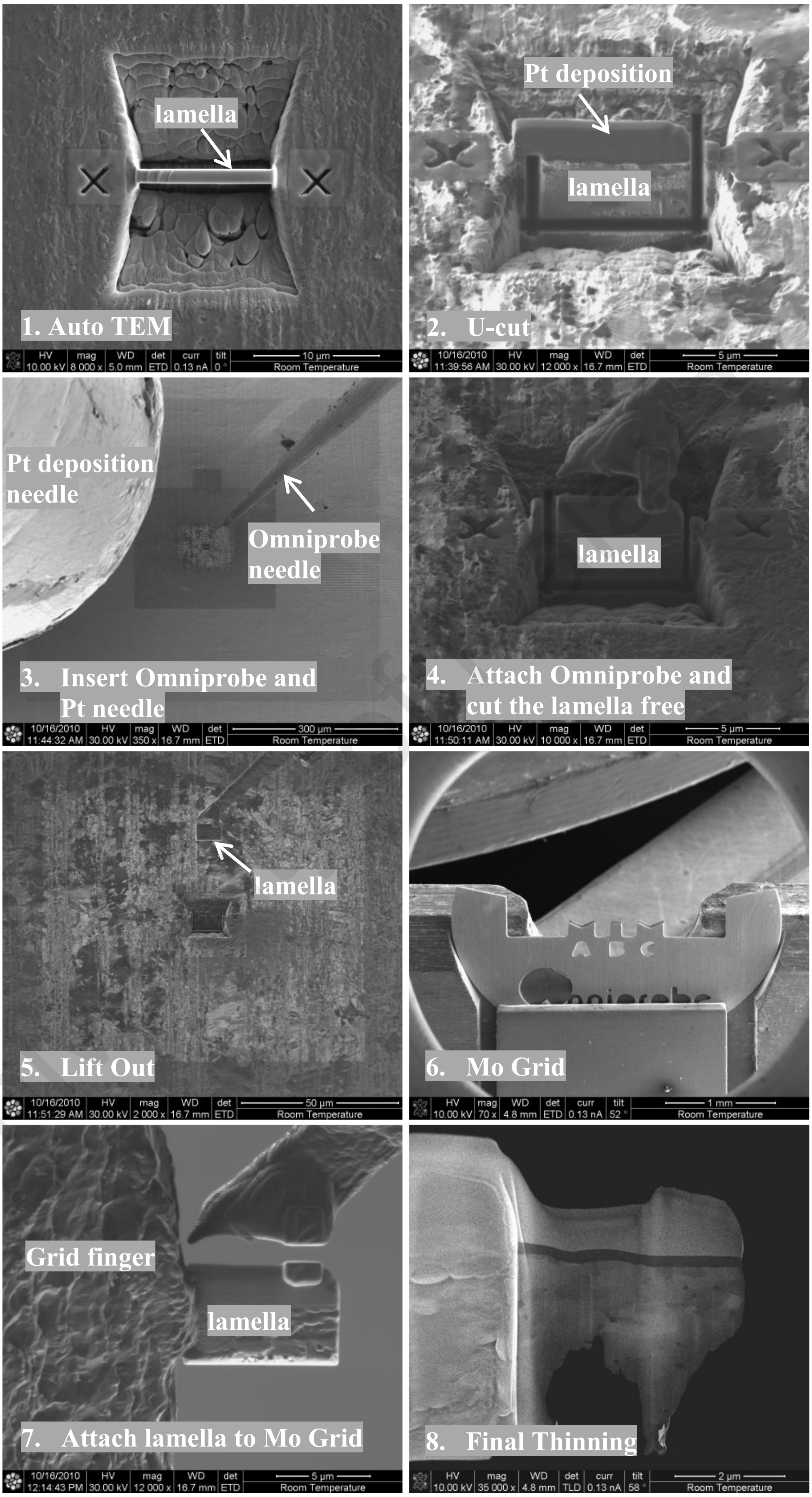

Figure 3.14: The TEM lamella preparation steps.

CHAPTER 4: RESULT AND DISCUSSIONS

4.1 Surface Characteristic of Heat Treated Copper Alloy Leadframe

In this section, the surface characteristic of the heat treated copper alloy leadframe samples is discussed mainly on the physical and mechanical properties variation. The investigation of colour change was done using high power optical microscopy. The surface texture of the sample was then studied by the electron microscopy. The 3D AFM micrograph was used to quantify the surface roughness of the samples. The mechanical properties of the samples were then measured using a Vickers micro hardness test. The surface grains and bulk grains were measured by using ASTM E 112 intercept counting method to understand the effect of the heat treatment on the grain size of the copper samples.

4.1.1 Variation of Copper Colour

Figure 4.1 shows the colour variation of the copper alloy leadframe samples that were heat treated at different temperatures with fixed heat treatment durations of 3 hours. The as-received sample displayed light brownish colour. Similar colour appearance was also observed in the samples that were heat treated at 60 °C, 90 °C and 120 °C. On the other hand, the samples that were heat treated at 150 °C, 180 °C, 210 °C and 240 °C displayed a significant colour changed as compared to the as-received sample. The colour sequence obtained from this heat treatment process is light brown, magenta, silver, dark brown and dark brown with traces of dark green colour.

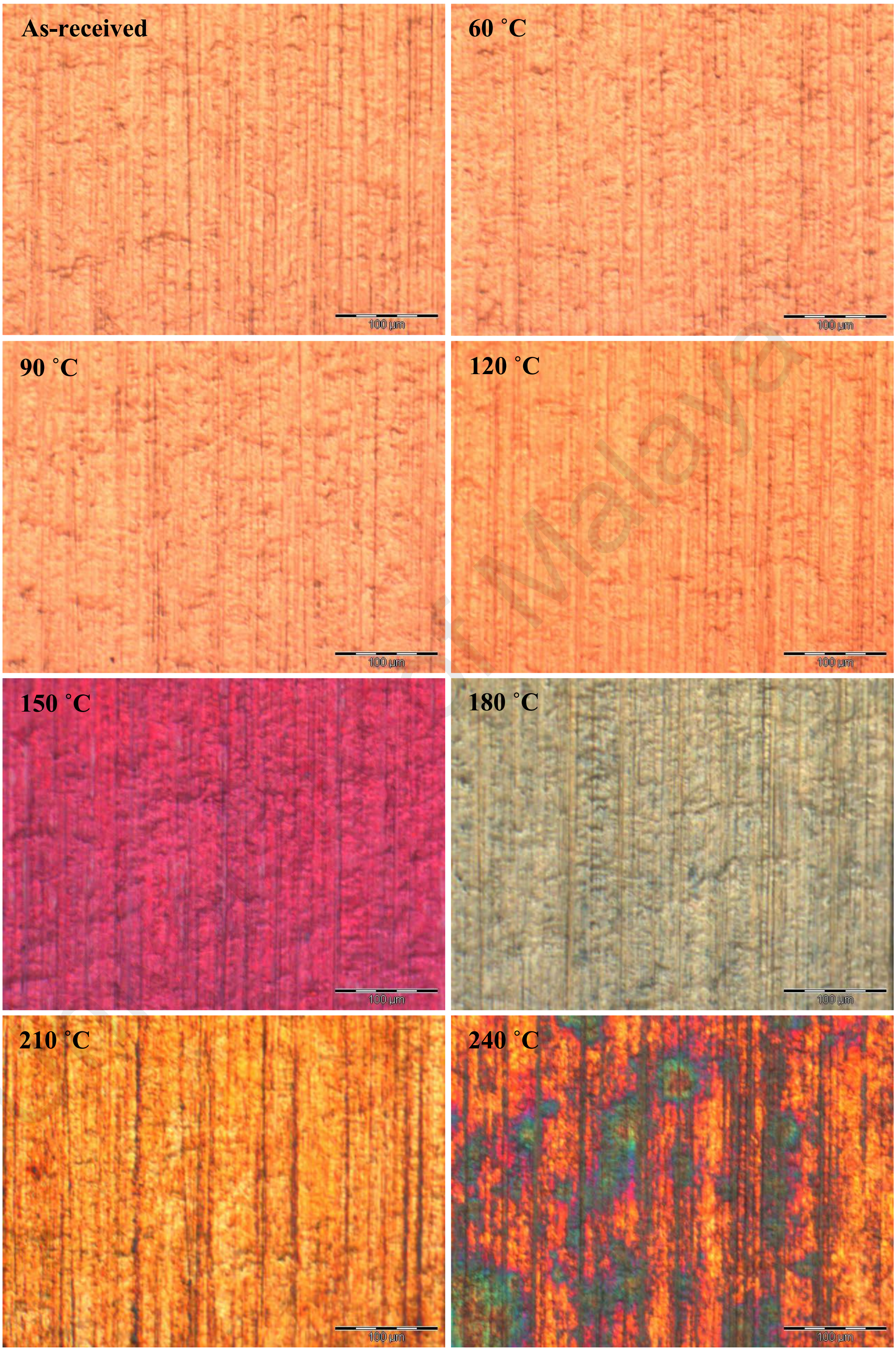

Figure 4.1: The physical colour change observed by the optical microscopy.

When a light travels from one medium to another, several things happened. Some of the light radiation might be transmitted through the medium, some will be absorbed and some will be reflected at the interface between the two media (Tandon, 2014). All reflected light obeys the relationship of reflection called Snell's Law (Whitaker, 1996). Figure 4.2 illustrates the Snell’s Law that describes the angle of the incidence ray is equal to the angle of reflection if the material has smooth or uniform surface.

However, if the surface is rough or non-uniform, it will cause the incident ray to be reflected at a different angle as illustrated in Figure 4.3 (Birkebak, 1965). This theory explains that the variation of the physical colour of the heat treated copper alloy leadframe samples from light brown to dark brown were likely due to the dissimilar surface conditions.

The colour change is also related to the copper oxide thickness variation which is well known and describes in many kinds of literatures. Diamanti (2018) described that the colour of the titanium oxides in her research work by means of anodic oxidation varies with film thickness due to the interference phenomena, taking place at the metal-oxide-air interfaces.

The sample that was heat treated at 240 °C shows two colours tone; dark brown with dark green spots. It was expected that the dark green region has a different surface texture condition as compared to the dark brown area. This hypothesis will be confirmed in the surface texture analysis.

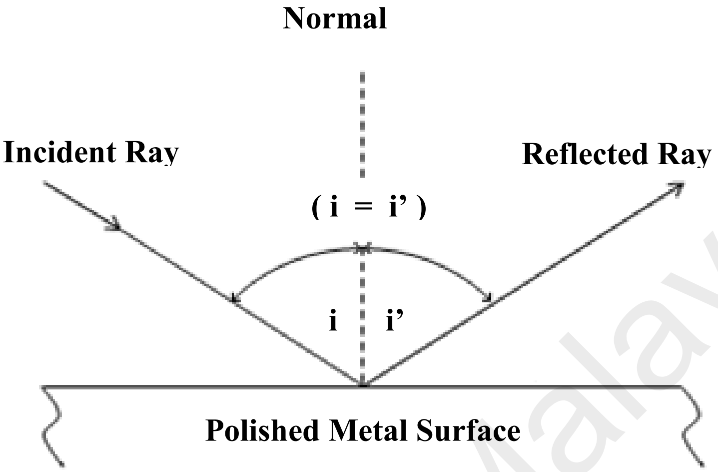

Figure 4.2: Snell's Law.

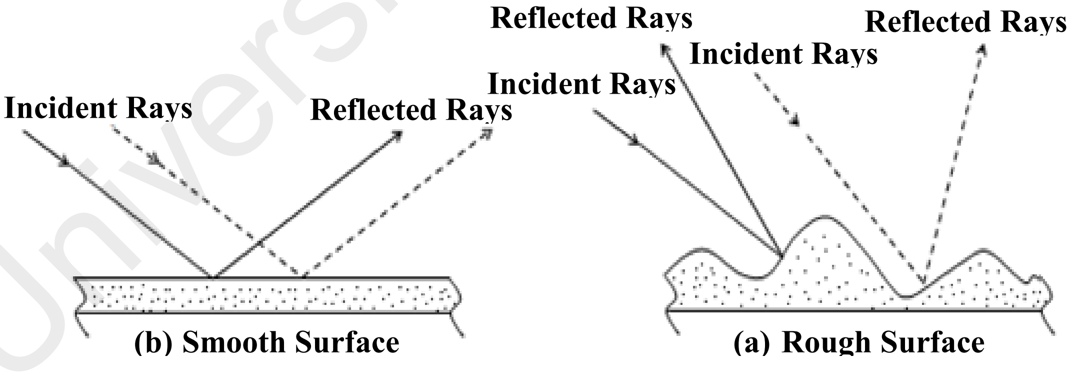

Figure 4.3: Reflection of light at dissimilar surface condition.

4.1.2 Surface Texture Modification

The surface texture of the samples was investigated qualitatively by the FESEM analysis. Figure 4.4 shows the FESEM micrographs of the samples that were acquired at 100,000 times of magnification. The as-received sample has relatively fine and smooth surface texture with indications of tiny particles with the size of 10 nm to 20 nm. The samples at 60 °C and 90 °C have a similar texture with the as-received sample. At 120 °C, the sample has a similar particle size with the as-received sample, however, it has denser tiny particles in a comparison with the as-received sample.

A significant surface texture change and enlargement of particle sizes were noted in the samples that were heat treated at 150 °C to 240 °C. The particle sizes in the range of 20 nm to 50 nm were observed in the sample at 150 °C. The sample at 180 °C shows patches-shaped of surface texture with scattered tiny particles. The patches have the sizes in the range of 200 nm to 300 nm.

At 210 °C, the particles agglomerated and formed 50 nm to 100 nm particle sizes. This result shows an initiation of isotropic growth of the surface grain, suggesting a porous surface. The most significant change in the surface texture was observed in the sample that was heat treated at 240 °C but limited to the dark green region. This region revealed a growth of nearly spherical shape of surface grains with the sizes of 100 nm to 200 nm with higher surface porosity. Berriche (1999) in his oxidation study of copper leadframes also found that oxidation has increased the porosity of the sample surface.

Figure 4.5 compares the surface texture of the sample that was heat treated at 240 °C. The dark green region shows a relatively rougher surface as compared to the dark brown region. This result validates the finding in section 4.1.1 that the physical colour variation is well correlated with the dissimilar surface texture condition due to the heat treatment process.

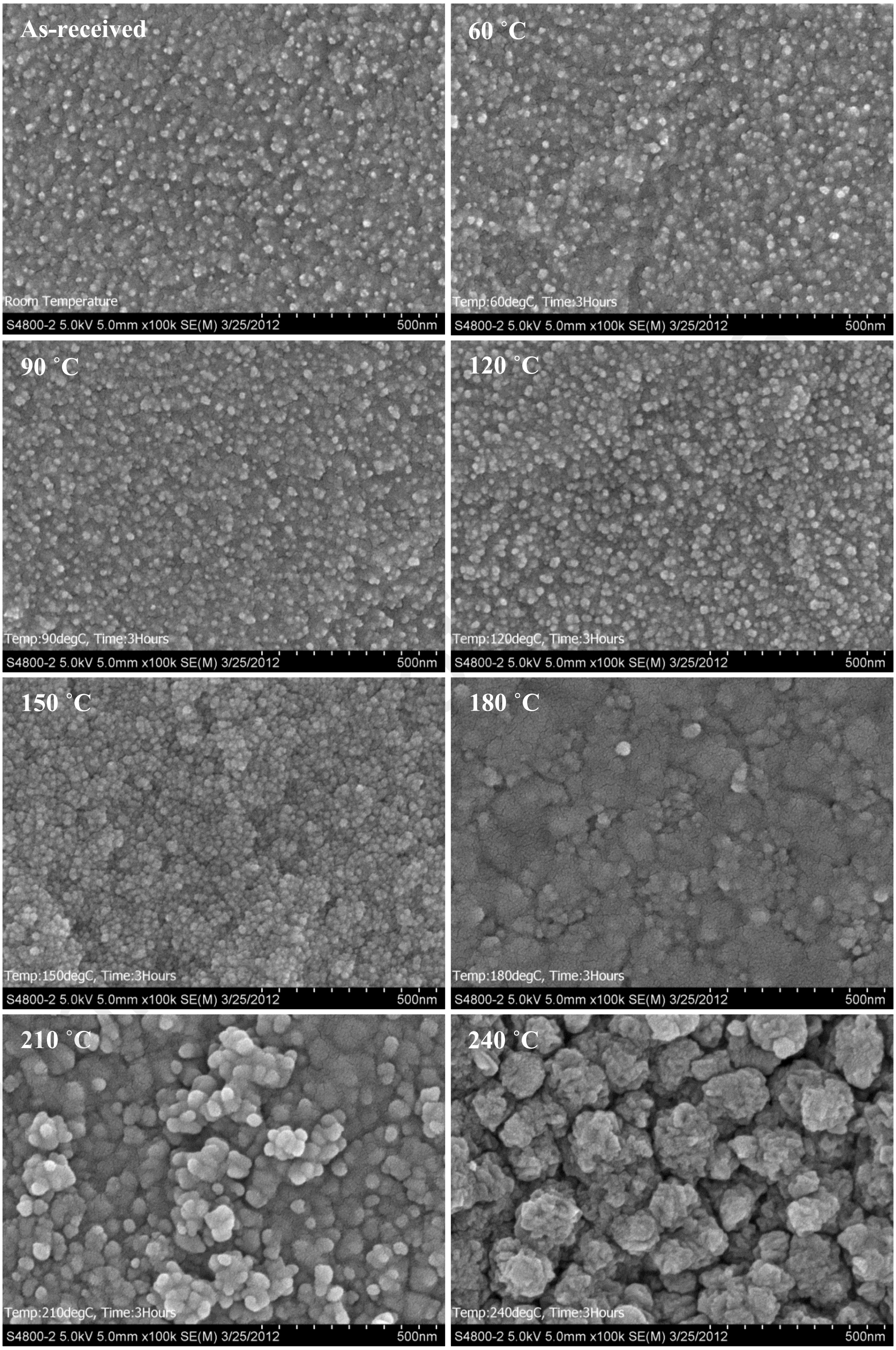

Figure 4.4: The FESEM micrographs show the surface texture of the samples.

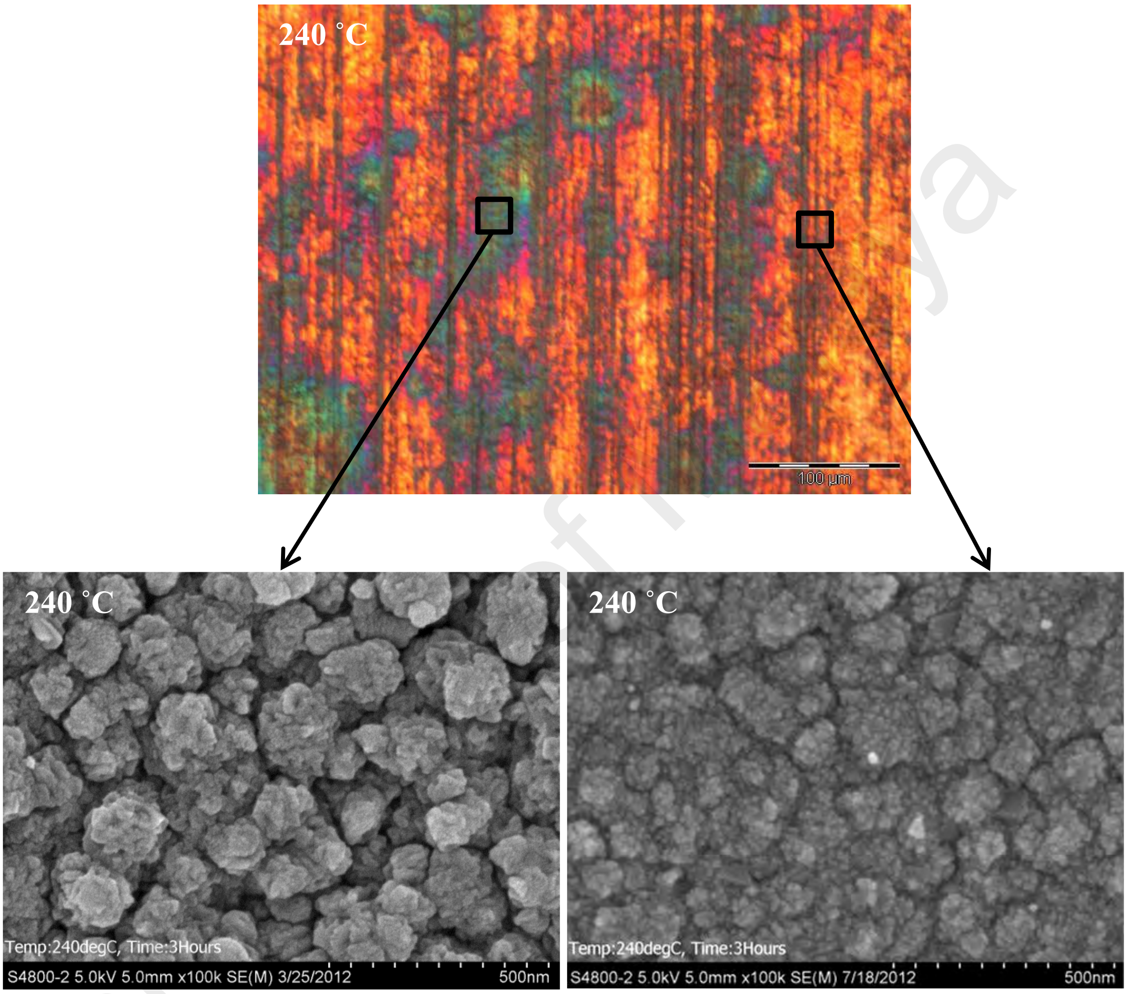

Figure 4.5: The FESEM micrographs at the dark brown and dark green region.

4.1.3 Surface Roughness

The surface roughness of the heat treated copper alloy leadframe samples were quantified by the AFM tapping mode technique. The RMS value obtained from AFM analysis was plotted against the temperature as shown in Figure 4.6 to understand the surface roughness change as a result of the heat treatment process.

In this graph, it is clearly seen that the surface roughness was increased exponentially with an increasing of heat treatment temperature. The as-received sample shows the RMS value of 25 nm. There is no significant change in the surface roughness of the samples that were heat treated at 60 °C and 90 °C. The surface roughness was slightly increased at the temperature of 120 °C, 150 °C and 180 °C with the RMS value of 26 nm, 28 nm and 31 nm respectively. A significant increase in the surface roughness was observed on the sample that was heat treated at 210 °C and 240 °C. The RMS value was increased more than 10 nm at this heat treatment temperature range as compared to the as-received sample. The RMS values were 36 nm and 46 nm respectively.

The difference in the surface roughness rate formation is due to the formation of the surface oxide through oxide nucleation and oxide growth (Zhou, 2004). Chuang (2006) in his oxidation study of copper pads had also observed that the surface roughness increased at elevated temperature could possibly be associated with the formation of copper oxide.

Figure 4.7 is the qualitative AFM micrograph on heat treated copper alloy leadframe samples. This AFM result is well correlated with the SEM micrograph that the surface of the samples becomes rougher as the heat treatment temperature increases. The as-received sample has relatively fine and smooth surfaced. The rough sample surface was observed in the samples that were heat treated above 150 °C.

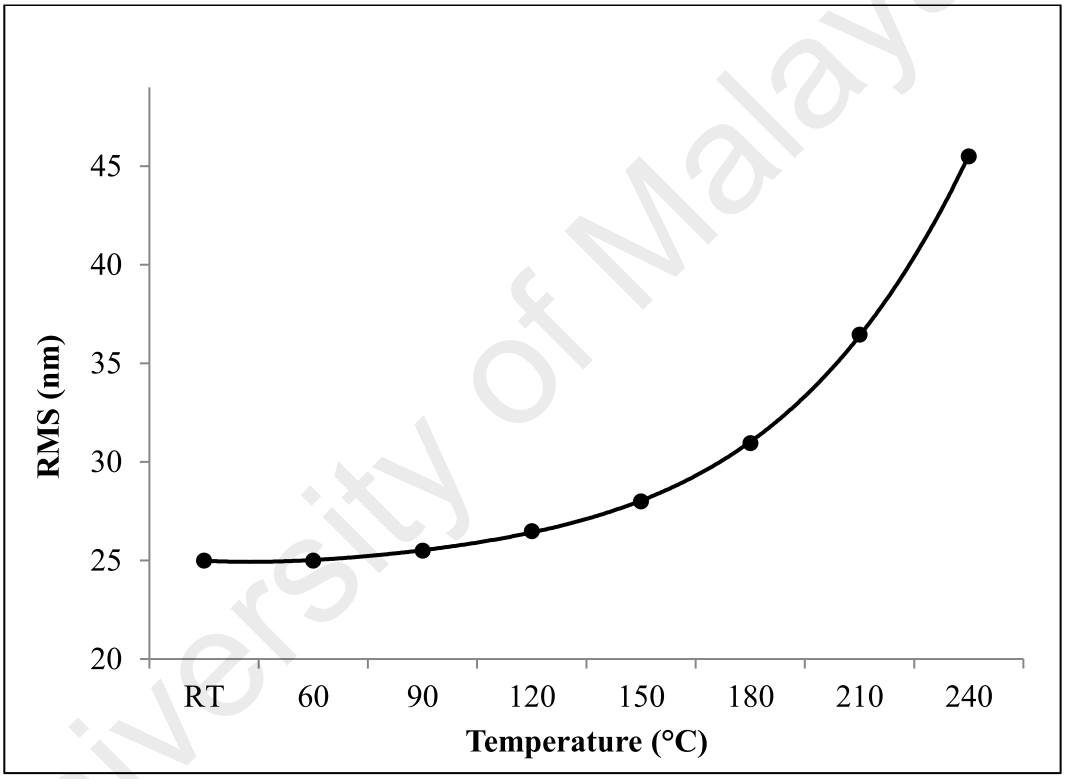

Figure 4.6: The surface roughness as a function of temperature.

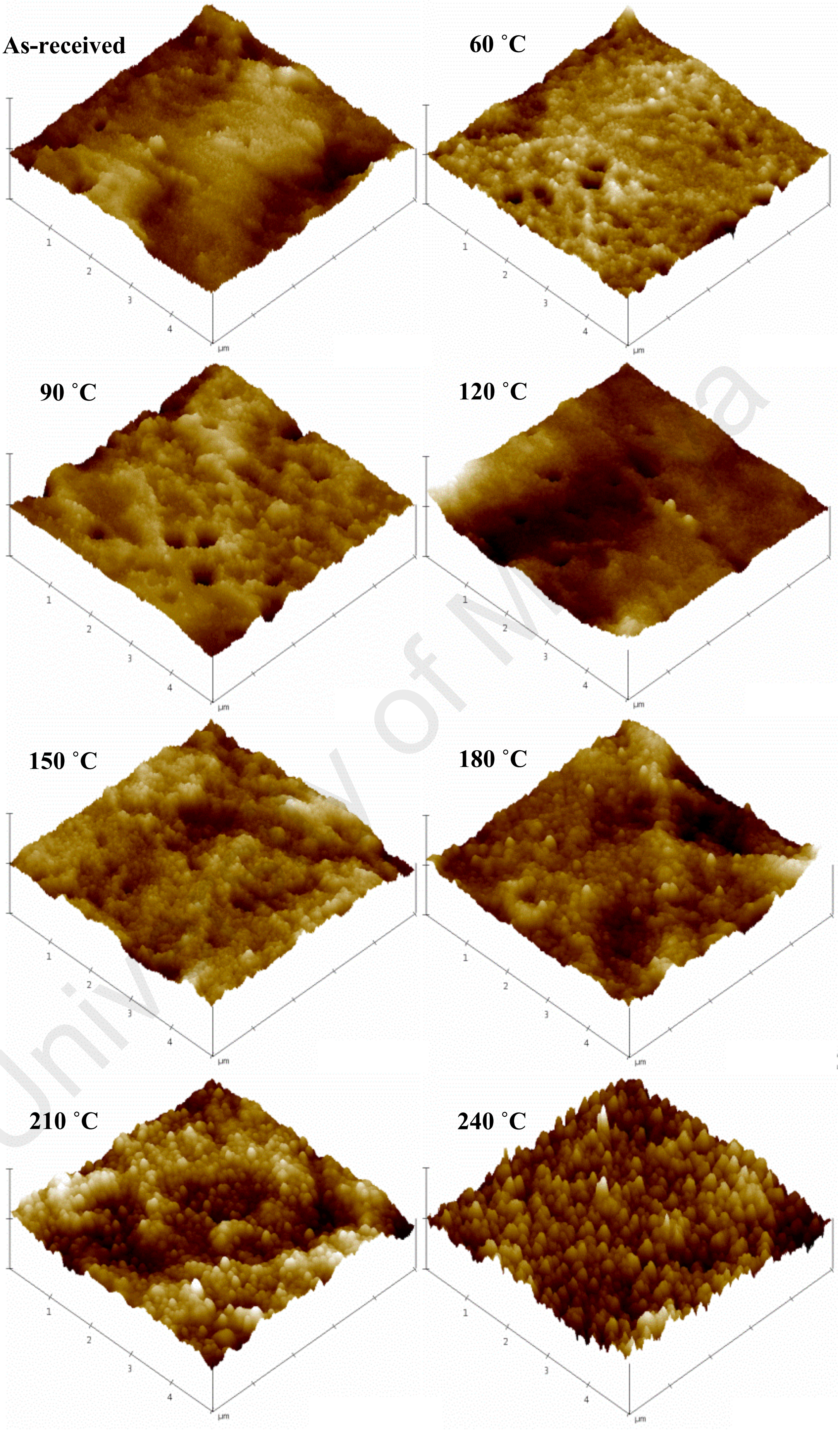

Figure 4.7: The AFM micrographs.

4.1.4 Surface Hardness

The surface hardness of the heat treated copper alloy leadframe samples was determined by Vickers micro hardness test. 10 points of micro indentations were performed on each sample using 980.7 mN loads. The average, maximum and minimum values of the surface hardness were plotted as a function of temperature to study the effect of the heat treatment temperatures to the surface hardness of copper alloy leadframe samples. This also provides the information on surface hardness variation within the sample.

Figure 4.8 shows the plot of the surface hardness as a function of temperature. The surface hardness of the samples was found to be increased with an increasing of temperature. The magnitude of hardness increases from the lowest to the highest value was in the range of 17 HV and the increasing trend was quite linear. Guleryuz (2004) in his study of other type of metal oxide (TiO_2) also found that thermal oxidation yielded higher surface hardness values. The qualitative analysis of the indentations on the sample surface was analyzed using high resolution electron imaging as shown in Figure 4.9.

Despite the variations of the surface hardness values between the oxidized samples were not significant, the image of the indentation shows that the surface of the sample has significant transformations of the surface properties from a ductile to the brittle metal surface as indicated by the crack formation on the indentation marks. This was evidently seen on the sample that experienced the heat treatment temperature of 180 °C and above.

A thin and brittle layer of metal oxide was found to be separated and cracked from the copper base material that follows the geometry and the perimeter of the indentation imprint. This is a phenomenon of stress corrosion cracking (SCC) that the corrosion layers flake off due to the corrosion and surface film growth (Panter, 2006). The higher rate of the copper oxidation at an elevated temperature promotes the nucleation, grain growth and a depleted layer of copper oxide resulting in the formation of a brittle surface with the interaction of corrosion and mechanical stress produced a failure by cracking.

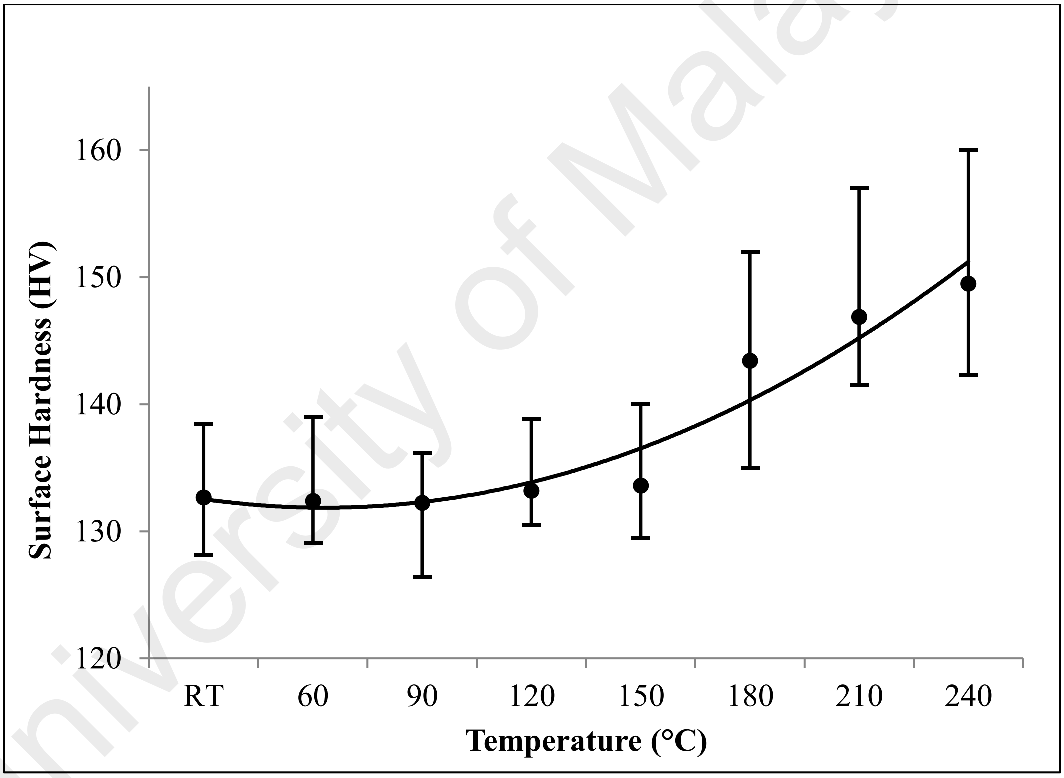

Figure 4.8: The surface hardness as a function of temperature.

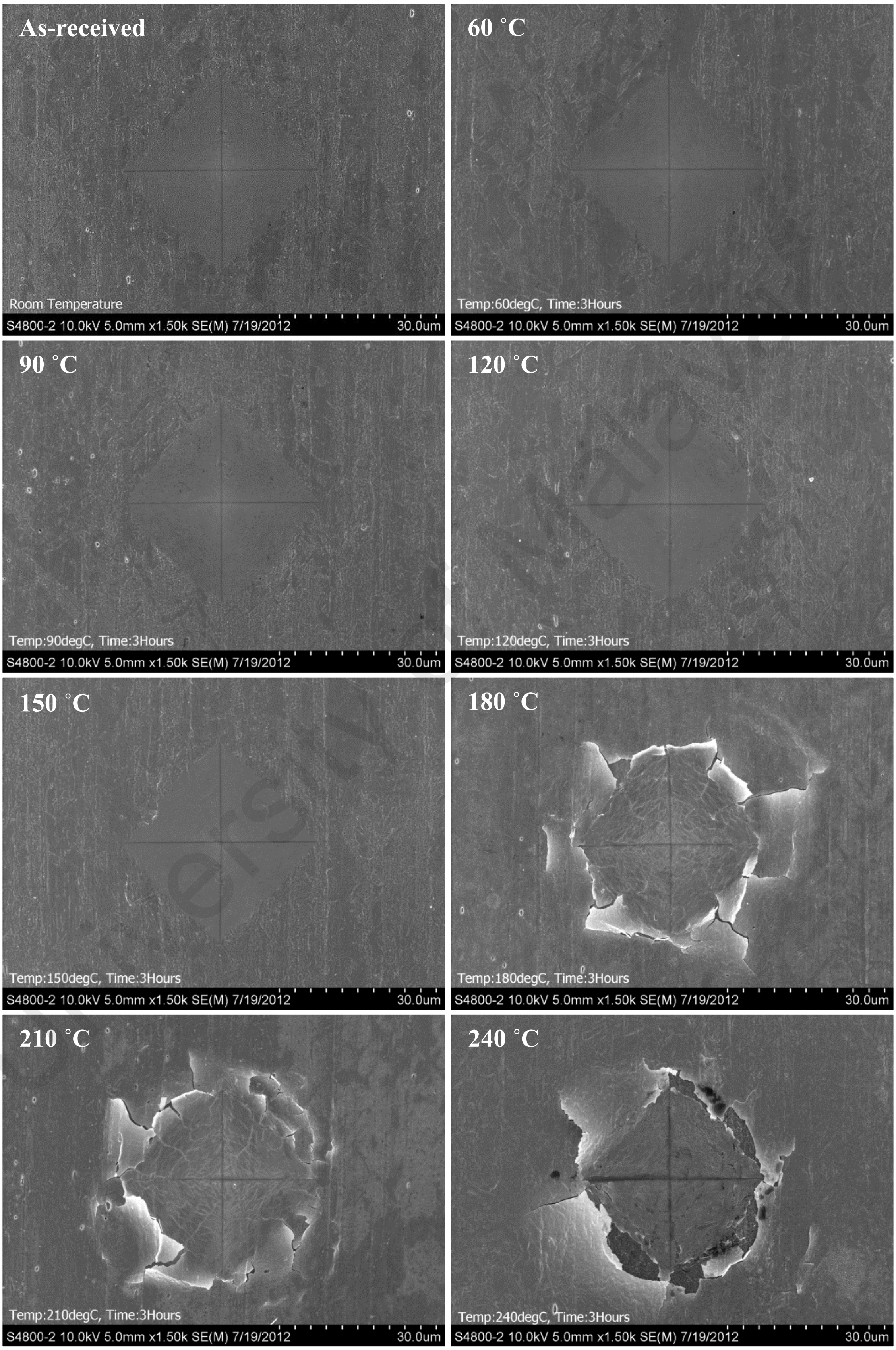

Figure 4.9 : The micro indentation micrographs acquired by the FESEM.

4.1.5 Grain Analysis

The surface grain of the heat treated copper alloy leadframe samples was imaged by using the secondary ion imaging in the FIB system. Prior to the ion imaging, the Ga ion beam was exposed to the sample surface to remove the oxidation layer until the surface grain was visible. The size of the copper grain on the sample surface was acquired at five different locations to calculate the average surface grain size. The size of the bulk copper grain was analyzed by performing a FIB cross section on the samples. Only one FIB cross section analysis was performed on each sample. The grain size was then measured by using ASTM E 112 intercept counting method.

Figures 4.10 and 4.11 show the results of the surface and bulk grains that were plotted as a function of temperature. Both graphs show that the grains were at the increasing trends as the temperature increases. In general, the surface grain has a smaller size as compared to the bulk grain. The surface grain size varies from 400 nm to 1200 nm on the as-received sample and the heat treated samples. Meanwhile, the bulk copper grain size varies from 1000 nm to 2000 nm. The maximum heat treatment temperature in this research work was 240 ˚C and the grains were at the recovery stage. According to Gondcharton (2015), the higher heat treatment temperature above 350 ˚C is required to change the grain properties to a recrystallization stage.

Figures 4.12 and 4.13 show the micrographs of the surface grains and the bulk copper grains. There were two different grain contrast in the ion micrographs; bright and dark contrasts. These contrasts difference were due to the channelling contrast effect of the grains (Hillard, 1999). In polycrystalline samples, the grains have a different orientation relative to one and another. The Ga ion beams in the FIB system penetrates the individual grains at different depths depending on the grain orientation and consequently generates different signal intensities in the secondary ion micrograph.

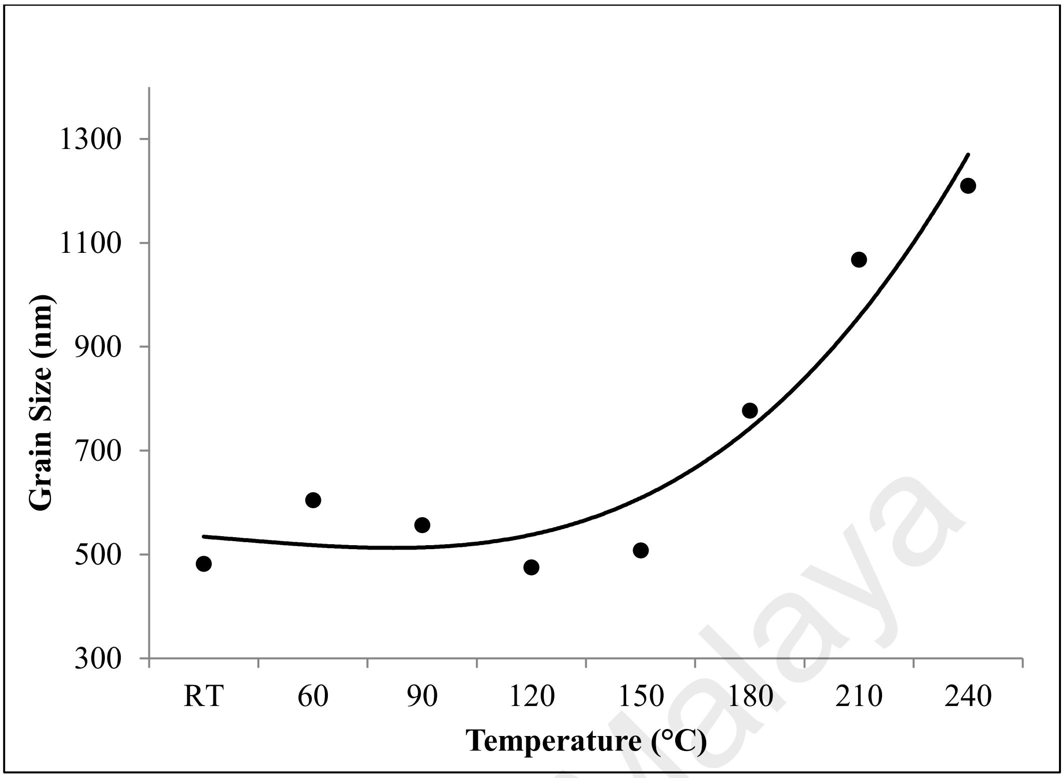

Figure 4.10 : The plot of surface grain size as a function of temperature.

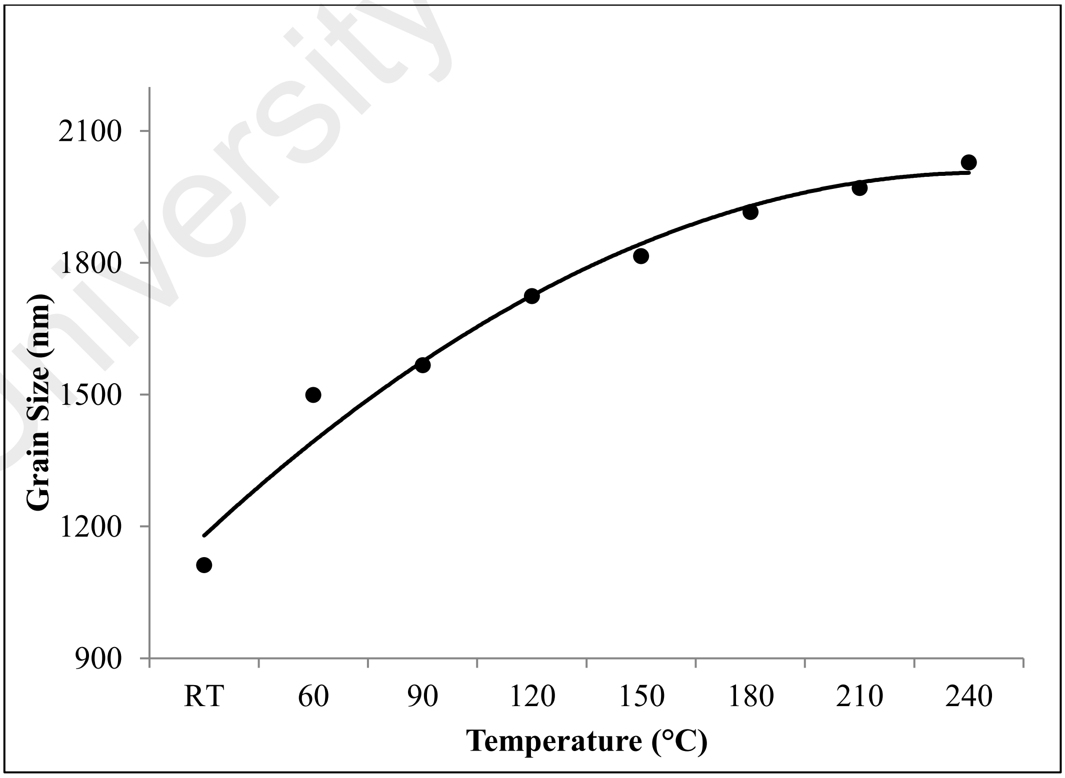

Figure 4.11 : The plot of bulk grain size as a function of temperature.

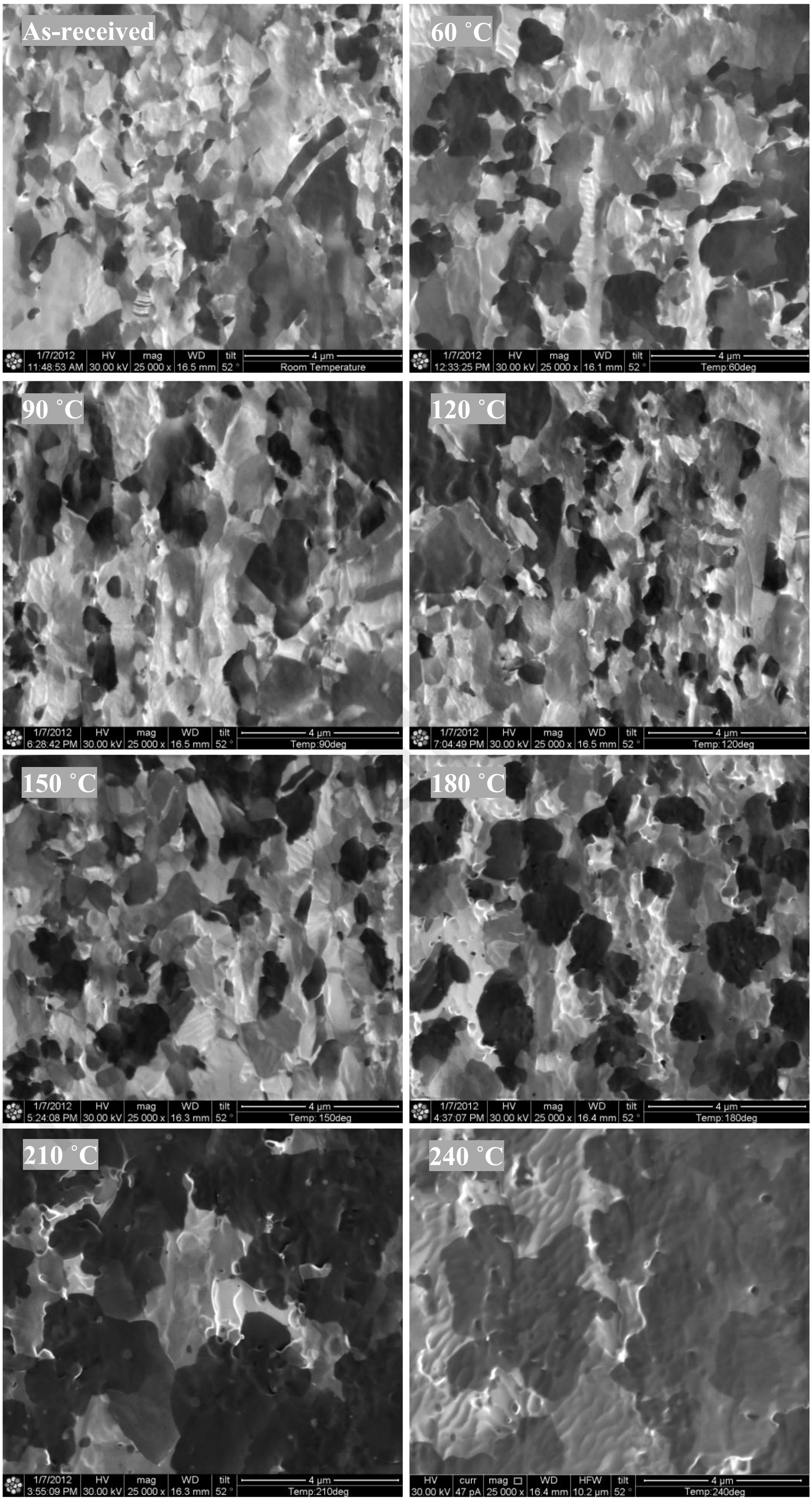

Figure 4.12 : The secondary ion micrographs of the surface grain.

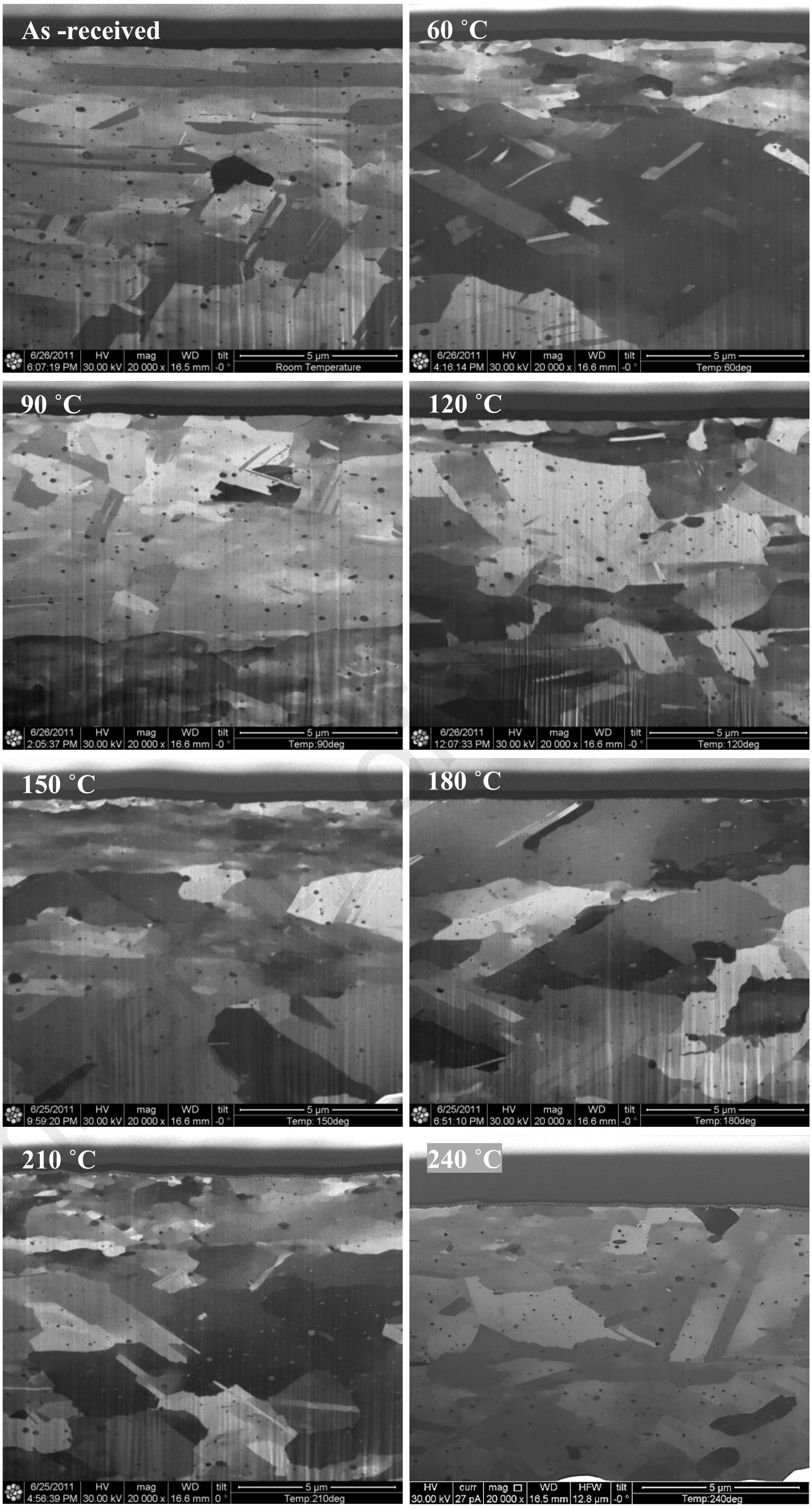

Figure 4.13 : The Secondary Ion micrographs of the bulk copper grain.

4.2 Spectroscopy Analysis

The spectroscopy analysis was performed to validate the presence of the copper oxide on the sample surface. The Energy Dispersive X-ray Spectroscopy (EDS) analysis in Field Emission Scanning Electron Microscopy (FESEM) which acquired from the sample surface provides bulk elemental compositions of the sample since the EDS signal penetration covered down to 1 µm area from the sample surface. The Auger Electron Spectroscopy (AES) depth profiling analysis provides the depth information of the copper oxide on the copper surface with reference to the SiO_2 as a standard of the etching rate. This provides an estimated thickness of the copper oxide on the sample surface. The EDS mapping and line scan analysis using Scanning Transmission Electron Microscopy (STEM) in the cross section view of the sample provides the elemental distribution and line profile information. On the other hand, the Electron Energy Loss Spectroscopy (EELS) analysis in TEM determined the oxidation state of the copper oxide from the cross section view of the sample. The sample was cross sectioned using Focused Ion Beam (FIB) prior to EDS and EELS analyses in TEM.

4.2.1 Energy Dispersive X-ray Spectroscopy (EDS) Analysis

The EDS analysis was acquired in an area of 5 µm by 5 µm on the sample surface. The acceleration voltage was 5 kV with an acquisition time of 200 seconds. Figure 4.14 shows the EDS spectra of the heat treated copper alloy leadframe samples. The EDS analysis detected the presence of carbon (C), oxygen (O) and copper (Cu) elements on the sample surface.

The EDS quantification analysis was carried out to further quantify the presence of oxygen and copper elements. The carbon element was excluded from this quantification since it was a hydrocarbon contamination that was induced from the environment and also the analysis equipment.

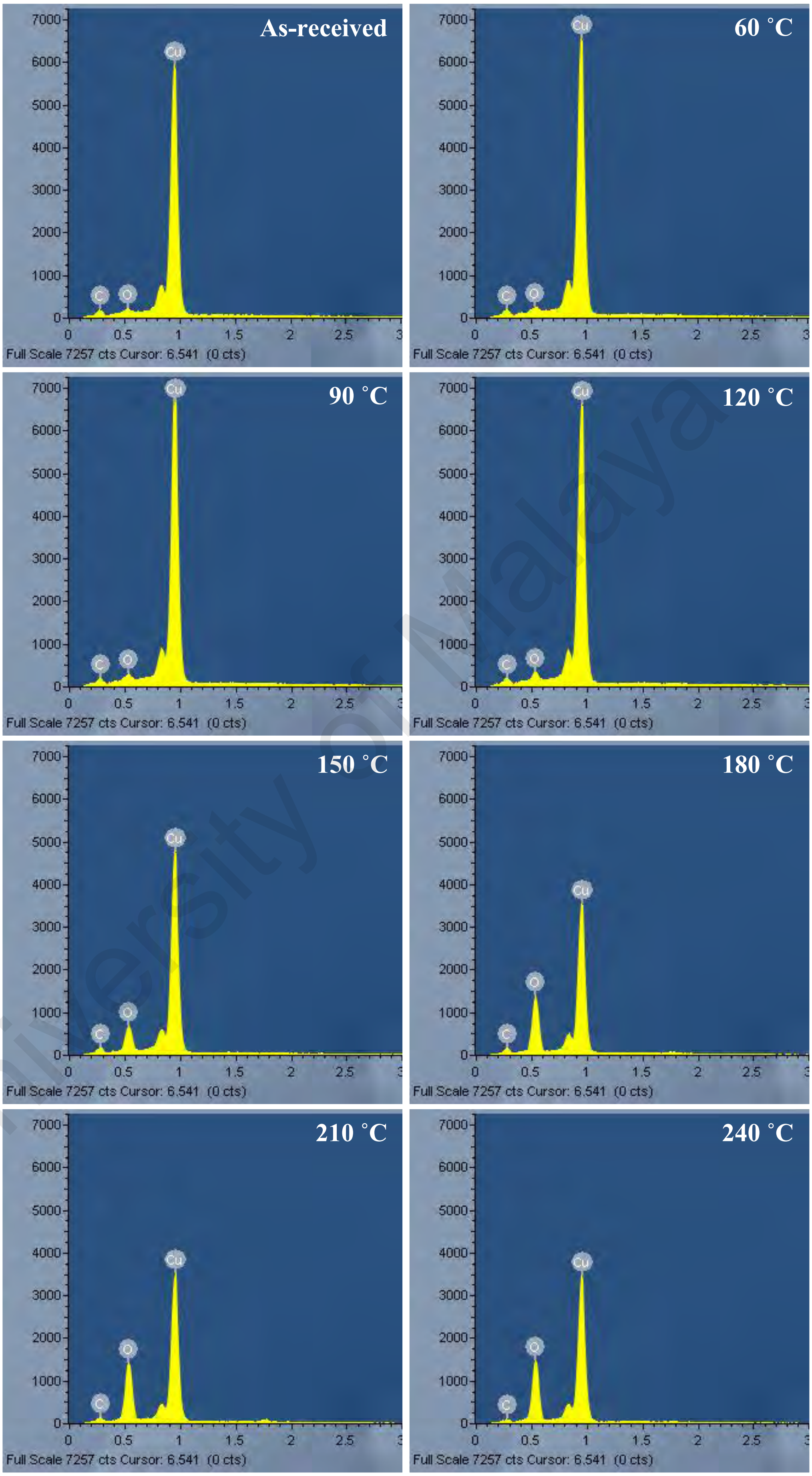

Figure 4.14 : The EDS spectrum.

Table 4.1 tabulates the EDS quantification results in atomic percentage (at %). The as-received sample has about 3 at % of oxygen content. No significant oxygen content was observed in the samples that were heat treated at 60 ˚C, 90 ˚C and 120 ˚C. However, at 150 ˚C and above, the oxygen content increased from 5 at % to maximum 40 at %. This result indicates that significant formation of copper oxide initiated at the heat treatment temperature of 150 ˚C and stabilizes at the heat treatment temperature above 180 ˚C.

Based on this EDS quantification results, it can be deduced that the oxidation with copper-riched Cu_2O was formed in the heat treatment temperature of 150 ˚C with Cu:O ratio of 3:1 and as the heat treatment temperature increases to 180 ˚C and above, the stabilized CuO is evidently present with Cu:O ratio of 1:1.

The initial formation of Cu_2O is due to the continuous supply of copper during oxidation process results in a copper-riched compound. As the heat treatment temperature increases, the supply of copper is retarded by the potential voids at the interface of copper to copper oxide while the copper-riched compound is continuously received the supply of environmental oxygen resulted in the formation of stabilized copper. This mechanism is evidently supported by the phenomenon of stress corrosion cracking (SCC) as discussed in section 4.1.4.

Table 4.1: EDS quantification results in atomic percentage.

Sample No.	Temperature (˚C)	Atomic %	
		Cu	**O**
1	As-received	96.95	3.05
2	60	96.71	3.29
3	90	96.13	3.87
4	120	94.13	5.87
5	150	80.23	19.77
6	180	59.52	40.48
7	210	57.70	42.30
8	240	56.15	43.85

4.2.2 AES Depth Profiling Analysis

The AES depth profiling analysis was carried out by 2000 eV argon (Ar) ion sputtering at the acceleration voltage of 10 kV and 10 nA current. The etching rate was 21.9 nm per minutes with reference to that of SiO_2 as a standard. In this depth profiling analysis, oxygen and copper elements were included in the profile to study the formation of copper oxide on the sample surface.

Figures 4.15 and 4.16 show the depth profile analysis results of all samples that were plotted in atomic density (at %) versus depth in nm. The presence of copper oxide was indicated by the oxygen profile. The copper oxide was completely removed by the Ar ion sputtering as the oxygen profile was depleted and the copper profile reached until 100 at %. The depth information of the oxygen profile relates to the copper oxide thickness on the sample surface.

In AES depth profiling results, the thickness of the layer was estimated by taking the 50 % intersections of the total atomic density as shown by the dotted line in Figures 4.15 and 4.16. Table 4.2 shows the estimated thickness of the copper oxide. The as-received sample shows approximately 3 nm copper oxide on the sample surface. At 150 ˚C, there was about 33 nm of copper oxide formation on the sample surface. At 180 ˚C, there was a significant increase in the formation of copper oxide as compared to the sample at 150 ˚C which was 84 nm. At 210 ˚C and 240 ˚C the copper oxide thickness was 130 nm and 230 nm respectively. In AES depth profiling analysis, the SiO_2 was used as a standard for the etching rate, this could give an error due to copper oxide have a different etching rate as compared to the SiO_2.

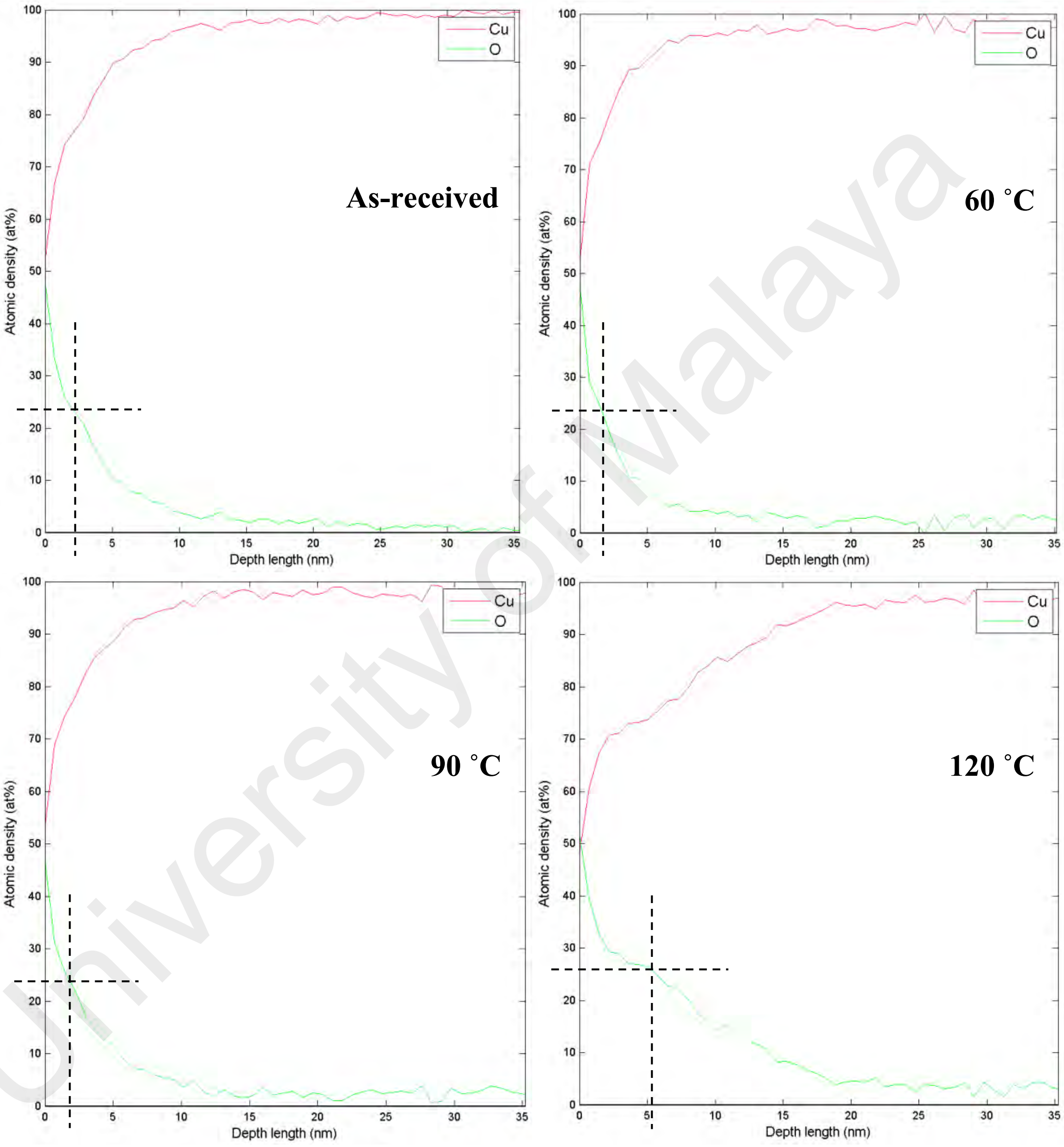

Figure 4.15: The AES depth profiling results of the as-received sample to 120 ˚C.

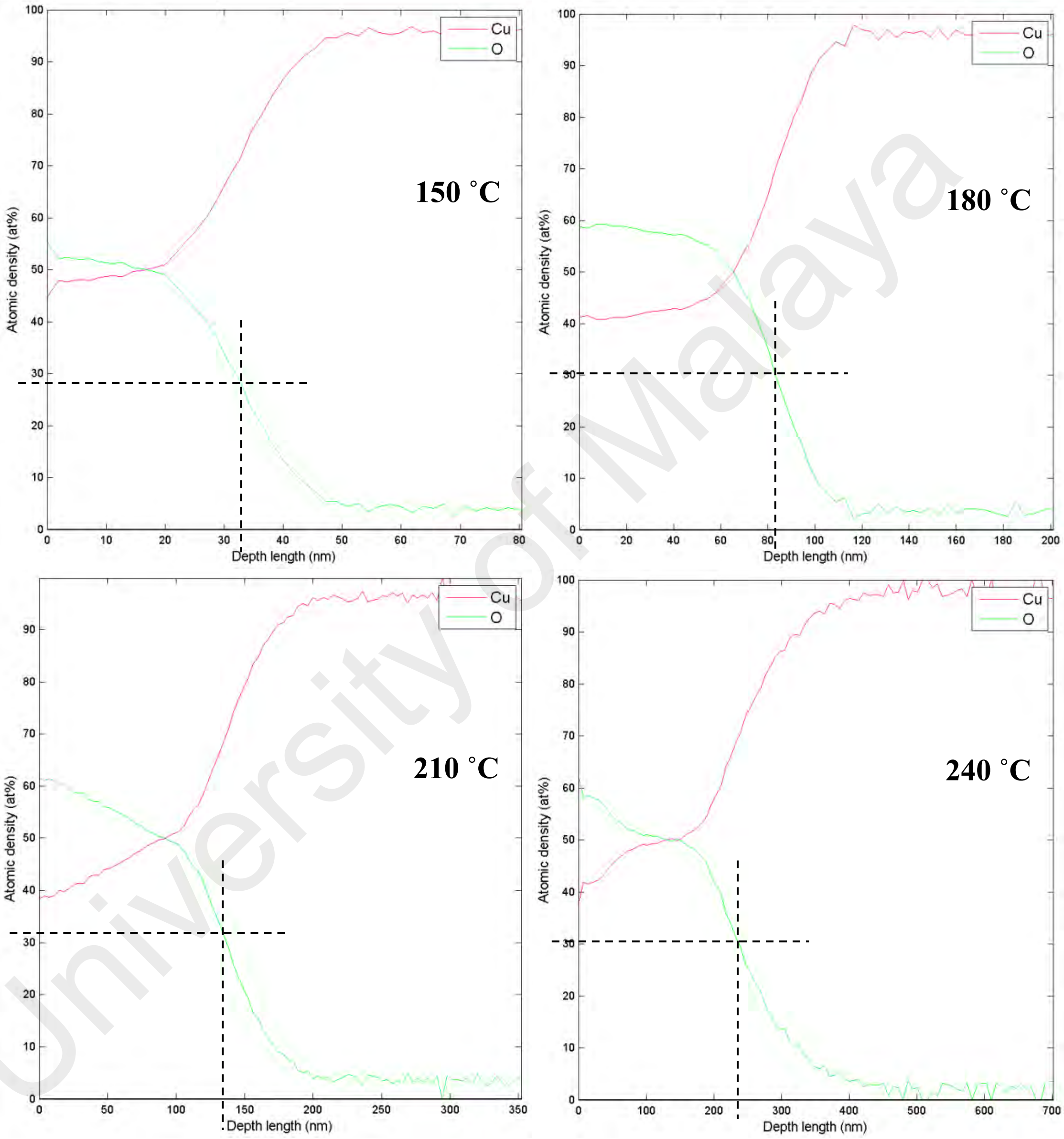

Figure 4.16: The AES depth profiling results of 150 ˚C to 240 ˚C.

Table 4.2: The estimated copper oxide thickness based on the AES depth profiling.

Sample No.	**Temperature (˚C)**	**Copper oxide thickness (nm)**
1	As-received	Not Applicable
2	60	3
3	90	3
4	120	6
5	150	33
6	180	84
7	210	130
8	240	230

The correlation of the EDS elemental analysis and the AES depth profiling result is discussed. One commonality on these two analyses is that the important reaction of copper oxide started on the heat treatment temperature of 150 ˚C and above. The EDS analysis results have indicated that the metal oxide seems stabilized at the heat treatment temperature above 180 ˚C and the AES depth profiling has shown that the reaction of metal oxide growth still continued. The TEM quantitative analysis on copper oxide growth will be performed in the next section to obtain more accurate information of the copper oxide growth.

4.2.3 STEM EDS Mapping and Line Scan Analysis

The TEM sample was prepared by FIB *in-situ* lift-out technique as discusses in section 3.3.10. There were two protective layers of platinum (Pt) that was deposited onto the sample surface. The first layer of Pt was induced by an electron beam and the second layer was induced by the ion beam. These protective layers were required to protect the copper oxide layer from the Ga ion beam damage during the TEM sample preparation. Figure 4.17 shows the STEM EDS mapping results on the sample that was heat treated at 240 ˚C analyzed in the small area of 150 nm by 200 nm.

This EDS mapping analysis shows that the two major elements were the oxygen represented by the blue colour and copper represented by the purple colour. At the interface region, the oxygen element was significantly present. Below the interface region, the oxygen element was not visible indicating the material was only a copper element. Above the interface region, both copper and oxygen elements were evidently present, indicating the copper oxide compound. There was an evidence of copper rich compound formation at the top region of the interface.

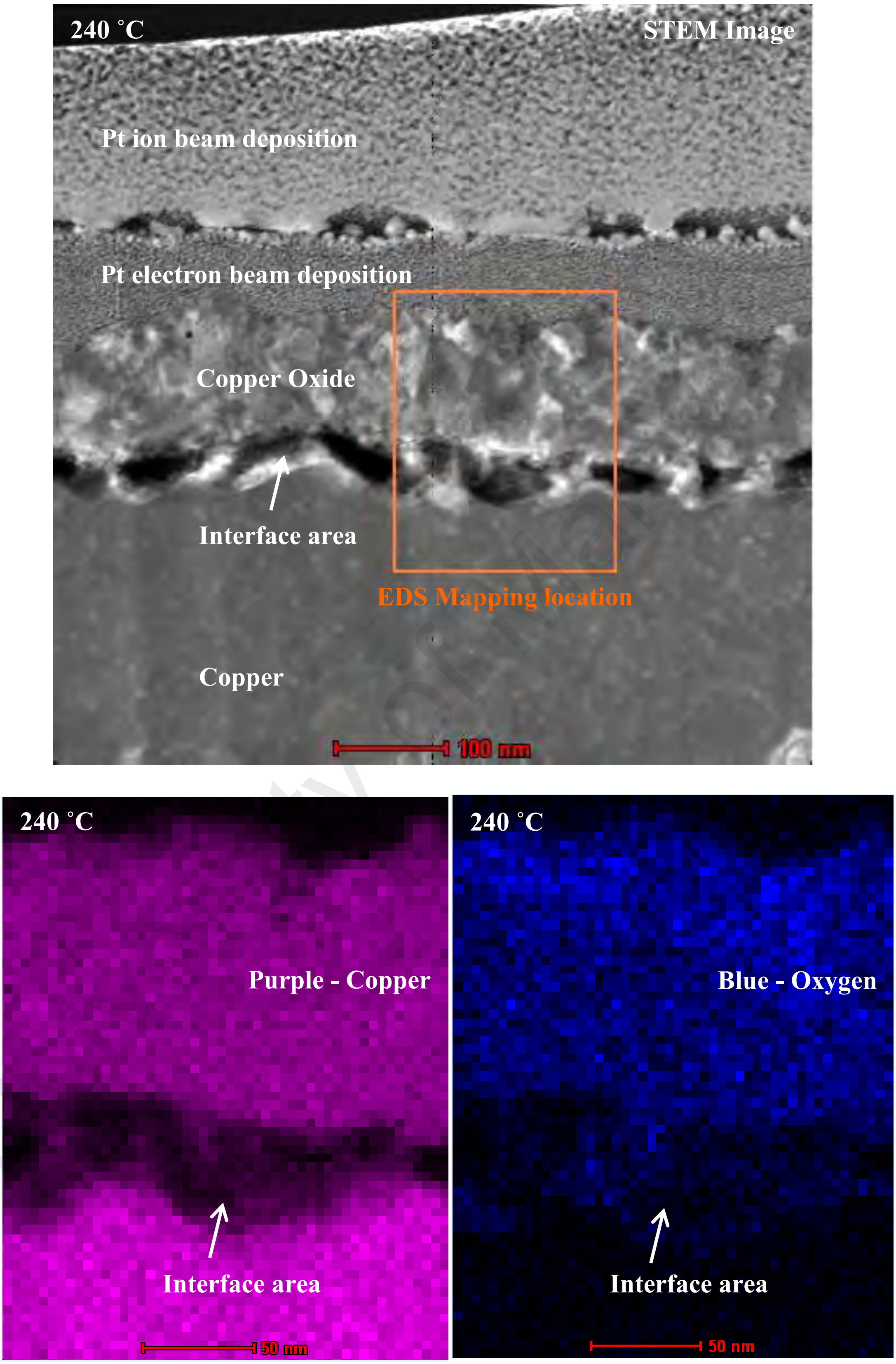

Figure 4.17 : The STEM EDS mapping of the sample at 240 ˚C.

The EDS line scan analysis was further carried out to obtain the line profile plot in atomic percentage across the copper oxide and the interface of copper to the copper oxide layer. Figure 4.18 represents the EDS line profile results. The results show that at the position of 110 nm from the initial point of the line scan, there was a low atomic concentration of copper and high atomic concentration of oxygen in which they were in the ratio of 50:50 atomic percent of copper and oxygen.

In the position of 240 nm from the initial point of the line scan, there was also evidence that the copper atomic concentration was decreasing while the oxygen atomic concentration was increasing which has a similar trend to the observation of the peak position of 110 nm. This copper and oxygen profiles give an indication of two different oxidation state formations that the CuO occurs at the interface of copper to the copper oxide and at the top region of the copper oxide. The top region of the copper oxide layer was contributed by Cu_2O oxidation state. This result will be validated using EELS analysis in the next section.

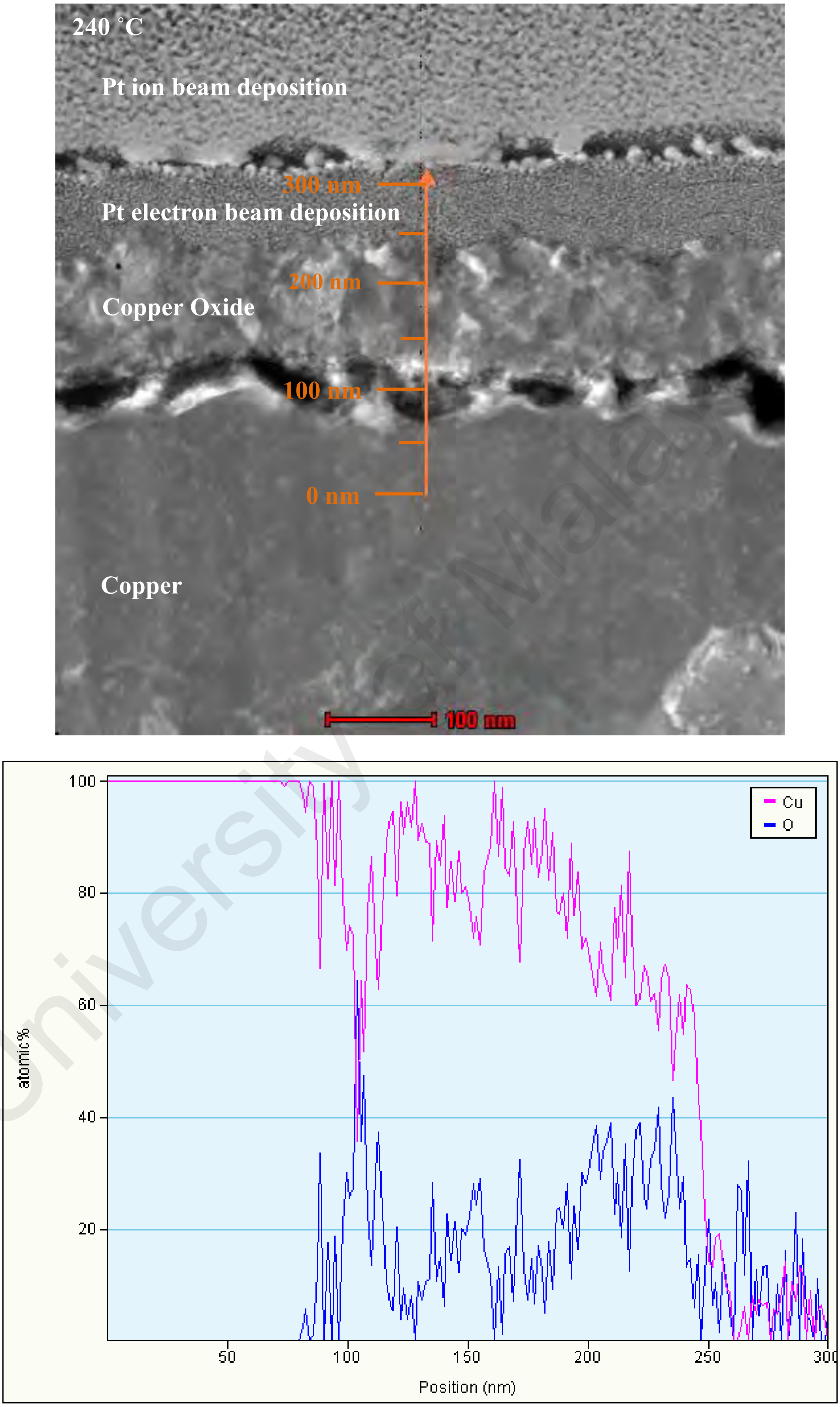

Figure 4.18 : The STEM EDS line scan of the sample at 240 ˚C.

4.2.4 EELS Analysis

The oxidation state of the copper oxide was further determined using the EELS technique. Figure 4.19 shows the EELS spectra of the bulk copper. The EELS library was used as a reference to determine the EELS spectrum that was obtained from the analysis.

Figure 4.20 shows the EELS analysis result of the sample that was heat treated at 210 °C. Four points of EELS analysis were performed on the cross section view of the copper oxide layer that was identified as the top, middle and an intact interface region.

Based on the EELS analysis results, it was identified that the interface layer consists of CuO phase. The middle part of the copper oxide layer has mainly Cu_2O phase. Towards the top layer of the copper oxide, there were the combinations of Cu_2O and CuO. This result is well aligned with the STEM EDS line scan result that has been discussed earlier in section 4.2.3.

In many of the reports, it has been claimed that the thermal oxidation of copper begins with the Cu_2O phase which is then converted to a CuO phase (Savaliya, 2015). A relatively simple explanation is that copper has two common oxidation states: +2 and +1: Copper (II) ions will form CuO whereas Copper (I) ions will form Cu_2O. Oxidation occurs rapidly as the newly formed copper atoms immediately react with dissolved oxygen molecules:

$$4Cu + O_2 \rightarrow 2Cu_2O \text{ and further oxidation} \quad (6)$$

$$2Cu_2O + O_2 \rightarrow 4CuO \quad (7)$$

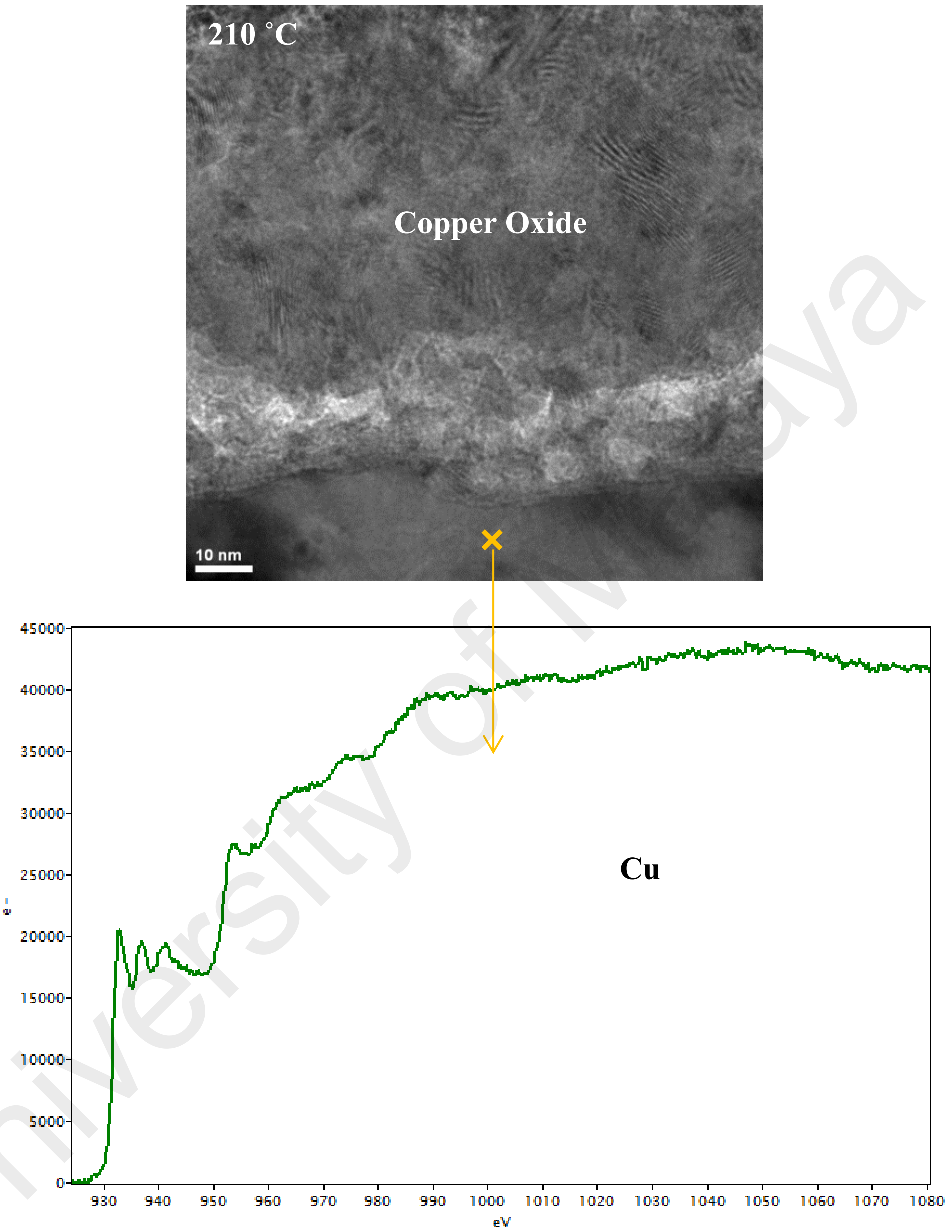

Figure 4.19 : EELS spectra of copper element.

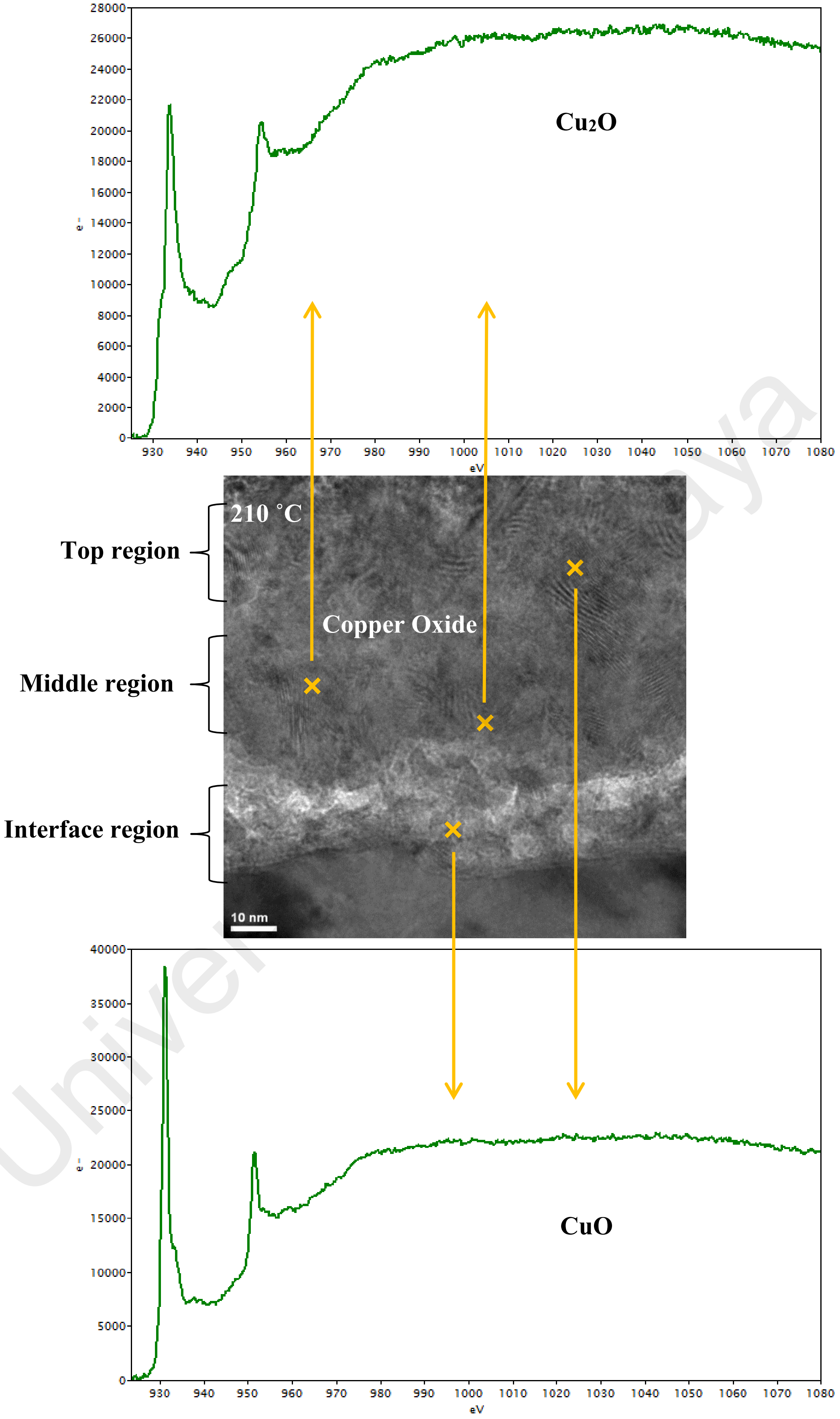

Figure 4.20 : EELS spectrum of Cu_2O and CuO.

In this EELS analysis, it can be explained that the EELS analysis was carried out in a relatively small area which is in nm range as compared to other techniques. This small scale analysis may have localized and non-uniform distribution of oxidation state of the copper oxide and thus the CuO phase was detected in the intact interface region of the sample. No CuO phase was detected at the interface that has micro-voids or micro-separation. Therefore, for this experiment, we obtained the oxidation system of CuO/Cu_2O/CuO/Cu for the area that has an intact interface region. However, for the region containing micro-voids or micro-separation, the oxidation system was CuO/Cu_2O/Cu.

Zhu (2004) reported in his copper oxidation study that at the oxidation temperature of 390 °C - 430 °C the CuO phase yielded directly. At first, with the increase of temperature, there will be a formation of copper-riched Cu_2O phase at the interface between the copper substrate and atmospheric oxygen, due to a large difference in molar volume between copper and its oxide creates high compression stress that leads to a high density of grain boundaries of this phase. These parameters with other favourable conditions convert the top layer of Cu_2O phase into CuO phase. The growth rate is controlled by two independent processes of the supply of copper ions to the interface, one is by outward lattice diffusion of copper ions that usually occurs at a higher temperature and another is grain boundary diffusion or defect mediated diffusion.

Gonçalves (2009) carried out a detailed study on the thermal oxide formation of CuO nanowires. He suggested that the fast supply of copper ions by the short circuit diffusion through grain boundaries favour the formation of CuO phase. Most of the work in the literature on the thermal oxidation of copper has been carried out on solid plates/discs and hence the formation of CuO phase above the Cu_2O phase must govern the lattice and grain boundary diffusion through the latter phase.

4.3 Kinetic Growth on Copper Oxidation

This section discusses the growth of the copper oxide in the cross section view of the samples using the HRTEM technique. This technique was used due to the formation of the copper oxide is in the nanoscale level as observed in the Auger depth profiling analysis. The HRTEM analysis allows the detailed quantitative microscopic analysis to be done. The quantitative analysis of the copper oxide layer as well as the study at the interface of the copper to the copper oxide layer is also possible. This interface region is examined to understand the factor that contributes to the delamination issues on the oxidized copper. The copper oxide thickness measurement using TEM is compared with AES depth profiling results. The crystal structure analysis of the copper oxide layer was performed using the electron diffraction technique in TEM. Lastly, the kinetic growth of the copper oxide, by means of the observation of the copper oxide thickness growth over the variation of temperature, is discussed by measuring the activation energy using the Arrhenius reaction rate model.

4.3.1 Nano-scale copper oxidation investigations

Figure 4.21 shows the HRTEM micrographs of the heat treated copper alloy leadframe samples. In this micrograph, there was a presence of an additional layer on top of the copper oxide layer. This layer was induced during the TEM lamella preparation as a protective layer to avoid any damage induced by the Ga ion beams on the sample surface.

The growth of copper oxide was indicated by a formation of a thin layer on the sample surface as being confirmed by the STEM EDS and EELS in section 4.2.3 and 4.2.4 respectively. There was a negligible formation of copper oxide on the as-received sample. A similar observation was also found in the samples that that experienced the heat treatment temperature lower than 150 °C.

At heat treatment temperature of 150 °C, a thin formation of copper oxide layer was observed. The thickness of copper oxide was 15 nm. The detailed analysis of the sample at 150 °C shows that there was an interface layer which appeared as bright contrast, in between the copper oxide and the bulk copper. This bright contrast was likely due to the low density of the copper oxide formation as a result of high and active interdiffusion between the oxygen and copper atoms causing low density interatomic bonding. This bright contrast interface layer contributes to almost half of the total of the copper oxide thickness.

As the heat treatment temperature was increased to 180 °C, the copper oxide thickness increased to 44 nm. The magnitude of the copper oxide thickness growth was 29 nm, from the heat treatment temperature of 150 °C to 180 °C. However, the interface layer with bright contrast was measured to be about 5 nm thickness, which was slightly thinner as compared to the sample at 150 °C. This is probably due to the copper to oxygen interdiffusion slows down once the supply of the two elements has reached the threshold limit. This will be analyzed and quantified in the reaction rate analysis using Arrhenius plot in section 4.3.2.

The summary of the copper oxide thickness using the TEM measurement is tabulated in Table 4.3.

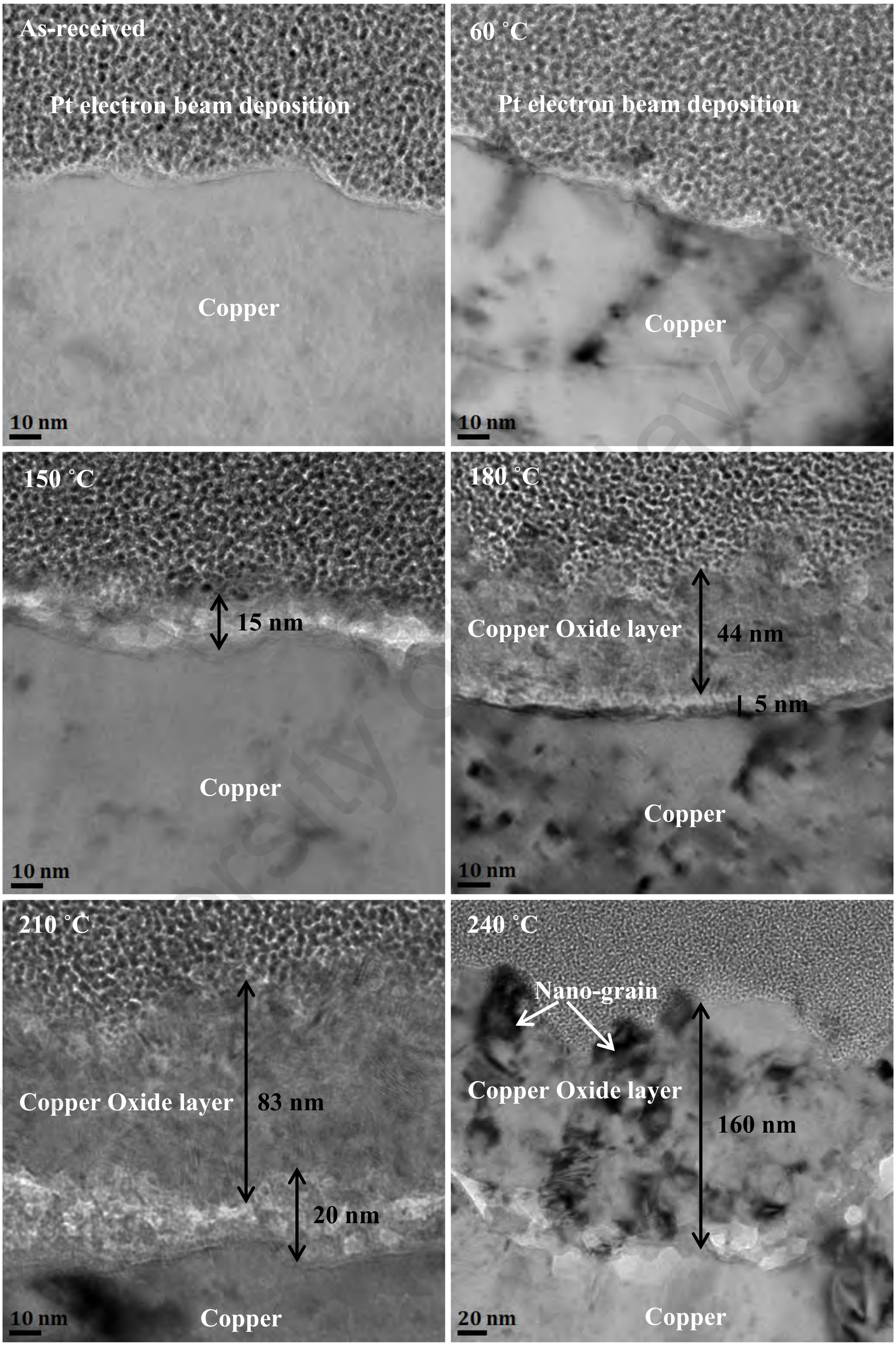

Figure 4.21: The HRTEM micrographs.

Table 4.3: The copper oxide thickness based on the HRTEM analysis.

Sample No.	**Temperature (˚C)**	**Copper oxide thickness (nm)**
1	As-received	Not Applicable
2	60	3
3	90	3
4	120	3
5	150	15
6	180	49
7	210	103
8	240	160

A closer examination of the sample that was heat treated at 180 °C found a noticeable formation of the copper oxide nano-grain, indicated by the black spots, in a random orientation with an average size of 5 nm on the sample. This black spot is called a copper oxide islands - a result of metal oxide nucleation during the metal oxidation process. The kinetic measurements of the oxide nucleation reveal that both nucleation density and surface coverage of Cu_2O islands can be promoted by alloying and oxidation temperature (Bogicevic, 2002). The ex-situ AFM studies reveal that the nucleation of oxide islands can occur on surface terraces and the subsequent oxide growth depletes local terrace copper atoms that result in the formation of surface pits (Venables, 2000).

At 210 °C, a significant increase in the copper oxide layer thickness was observed. The copper oxide has a thickness of 83 nm. The interface layer with a bright contrast shows the thickness of 20 nm which was slightly thicker than the previous two heat treatment temperatures. This is probably due to the interdiffusion process between copper and an oxygen element has reached the saturation limit of copper-riched Cu_2O metal oxide.

The further oxidation process is the reaction of copper-riched oxide with the environmental oxygen to form the stabilized CuO copper oxide. Further analysis at 210 °C heat treated samples shows strong evidence that the earlier metal oxide island of 5 nm has increased the size up to 20 nm. This is the phenomena of the metal oxide formation that started with metal oxide nucleation followed by the grain growth as the heat treatment temperature increases.

The copper oxide layer thickness was further increased to 160 nm at 240 °C heat treatment temperature. The copper oxide grain was clearly visible as indicated by the dark spot with the estimated grain size of 40 nm. The dark contrast of the grain also indicates the transformation of the high angle copper oxide grain boundary.

4.3.2 Kinetic Growth of copper oxidation

The detailed analysis of the growth of the copper oxide thickness was done by plotting the copper oxide thickness versus the heat treatment temperature derived from the TEM thickness measurement as shown in Figure 4.22. The Auger depth profiling analysis of different heat treatment temperature as tabulated in Table 4.2 was also plotted as shown in Figure 4.23.

The plots show commonality that the formation of the copper oxide thickness has the exponential growth characteristics. Both plots show an aggressive formation of the copper oxide thickness that follows an exponential growth characteristic at the heat treatment temperature above 150 °C. There was a deviation of copper oxide thickness measurement between TEM versus Auger depth profiling measurements.

The thickness measurement in TEM analysis has lower readings in the magnitude of 40 nm and 90 nm at the heat treatment temperature of 210 °C and 240 °C respectively as compared to the Auger depth profiling analysis. This deviation was due to the SiO_2 etching rate, which was 21.9 nm per minutes that was used as a reference standard. For higher accuracy, the copper oxide etching rate shall be used as a standard and has to be calibrated prior to the actual measurement. Therefore, the Auger depth profiling analysis result can only be used as an initial reference to the growth of copper oxide. For this copper oxide thickness analysis, the TEM measurement is more accurate due to the necessary steps were taken in performing the *in-situ* measurement using the TEM imaging.

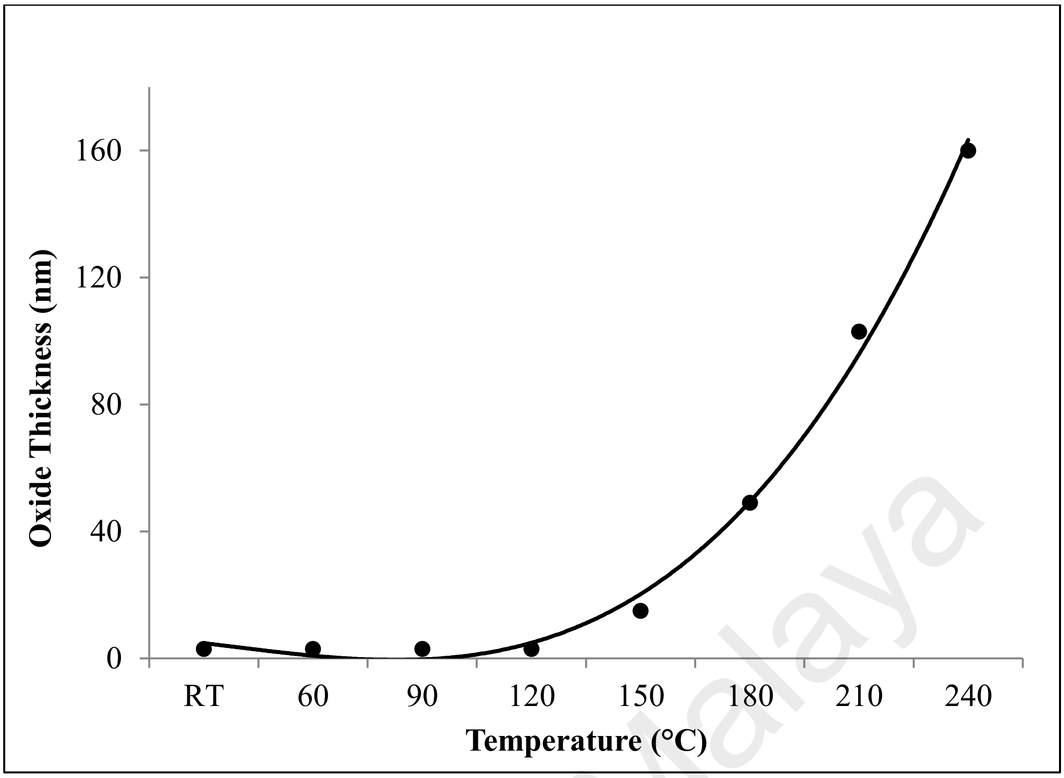

Figure 4.22: Copper oxide thickness measurement using HRTEM.

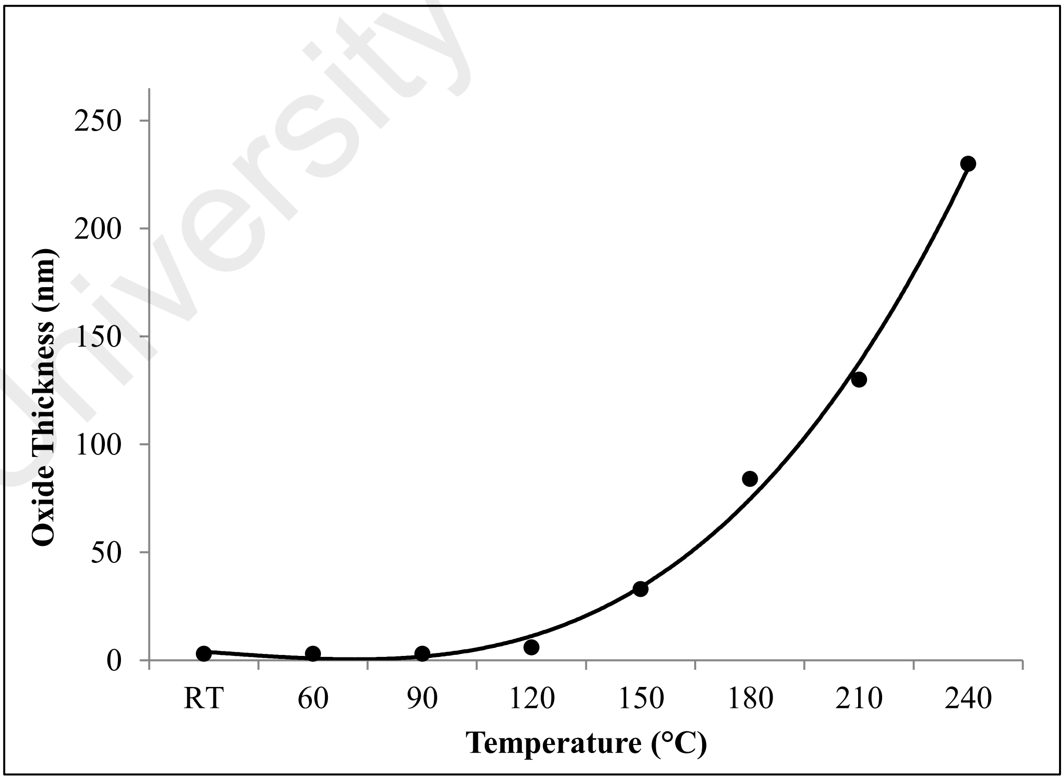

Figure 4.23: Copper oxide thickness measurement using AES.

The growth of the copper oxide occurs as a copper surface comes into contact with oxygen. The reaction sequence leading to oxidation of the copper surface is generally accepted to be oxygen chemisorption, nucleation and growth of the surface oxide, and bulk oxide growth. At high temperature, oxidation is controlled by diffusion of copper atoms through Cu_2O lattice, while at a lower temperature, the diffusion of copper atoms mainly is through the boundaries of Cu_2O (Gattinoni, 2015).

The rate of the copper oxidation depends on thermal activation, so the major factor to consider is the fraction of the molecules that possess enough kinetic energy to react at a given oxidation temperature. According to the kinetic molecular theory, a population of molecules at a given temperature is distributed over a variety of kinetic energies that is described by the Maxwell-Boltzman distribution law (Petrucci, 1997). This analysis indicated that as the heat treatment temperature is raised to 150 °C and above, it exceeds the kinetic energy to cause the reaction rate of copper oxidation to increase rapidly.

Temperature is considered a major factor that affects the rate of the oxidation. It is considered a source of energy in order to have a chemical reaction to occur. Svante Arrhenius, a Swedish chemist, believed that the reactants in a chemical reaction needed to gain a small amount of energy in order to become products. He called this type of energy as the activation energy. The amount of energy used in the reaction is known to be greater than the activation energy in the reaction.

The heat treatment temperature affects the chemical reaction rate due to the phenomenon related to the collision theory. Molecules only react if they have sufficient energy for a reaction to take place. When the temperature of a solution increases, the molecular energy levels also increase, causing the reaction to proceed faster. The graph of ln (t) versus 1/T is linear, allowing the calculation of the activation energy that is required for the reaction.

Figures 4.24 and 4.25 show the Arrhenius plot of copper oxide thickness as a function of heat treatment temperature for both TEM and AES technique. The apparent activation energy, as calculated from the slope of this straight line was 41 kJ/mol and 45 kJ/mol for both TEM and AES technique respectively. This activation energy was in the agreement with the findings from numbers of researchers as discussed in section 2.9. The calculated activation energy found by other researchers was in the range of 40 kJ/mol to 224 kJ/mol. However, this activation energy is very much depending on the type of copper material that was used, different atmospheric conditions and also different temperatures range.

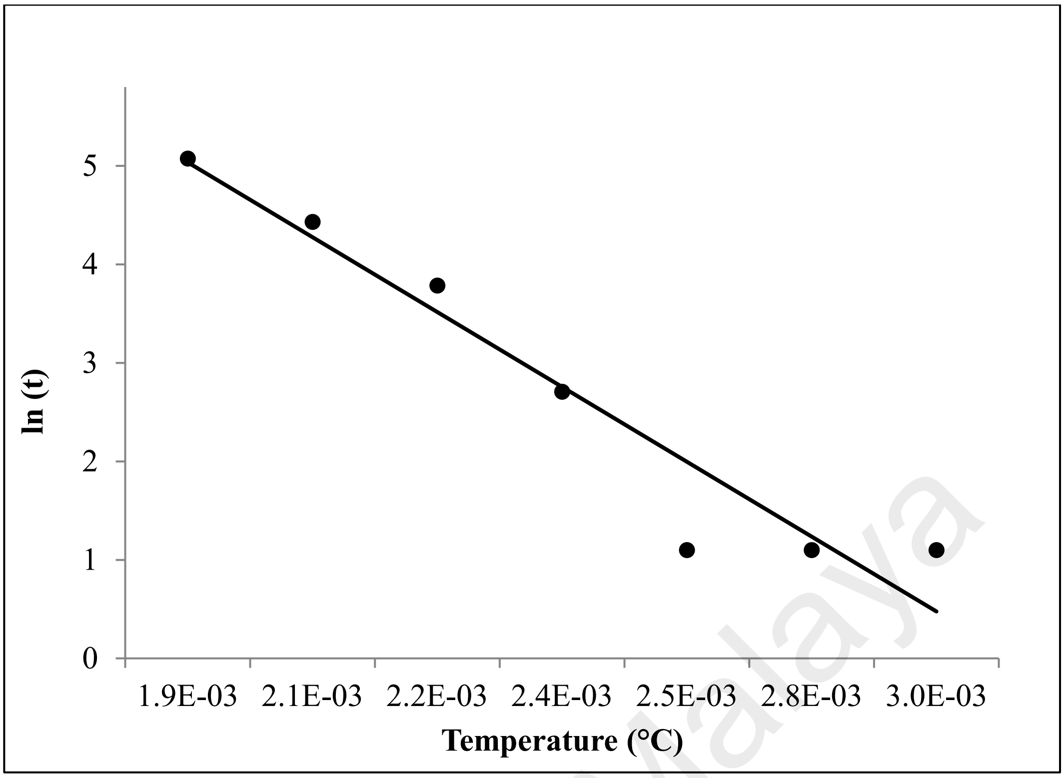

Figure 4.24: Plot of In (t) versus Temperature (1/K) for TEM technique.

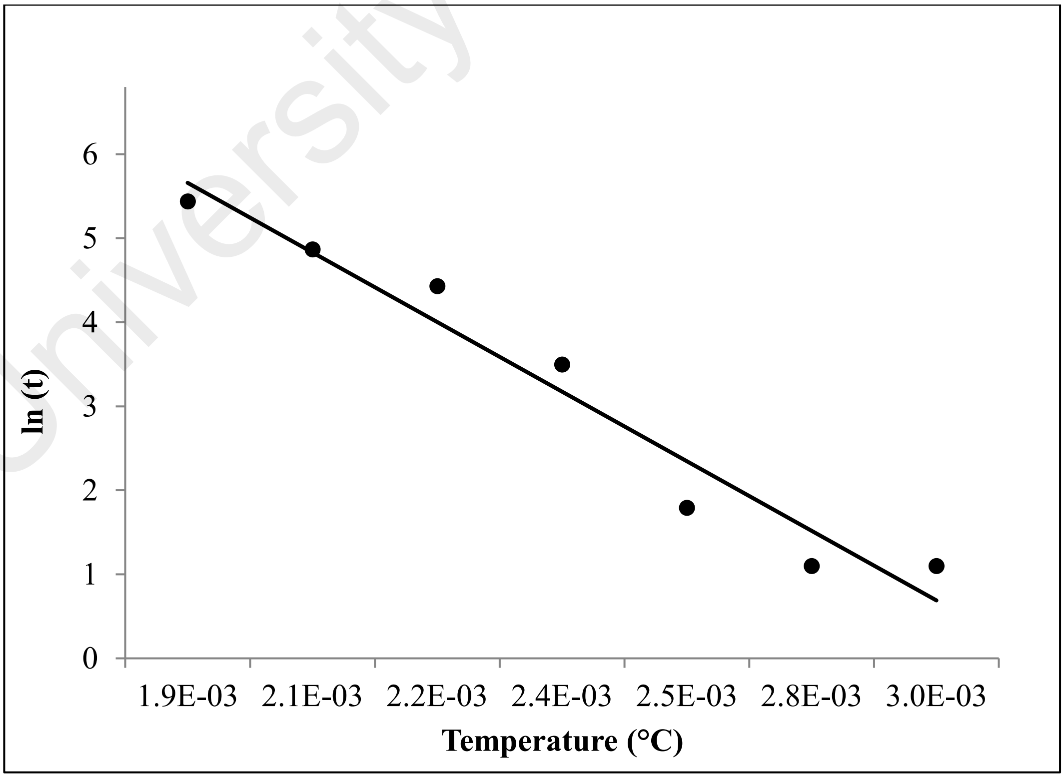

Figure 4.25: Plot of In (t) versus Temperature (1/K) for AES technique.

4.3.3 Void Formation

The interface layer of the copper oxide appeared as a bright contrast in the TEM bright field imaging due to the low density formation of the copper oxide resulting in the development of micro-voids along the interface. Figure 4.25 is the low magnification of the bright field TEM micrograph that shows the evidence of micro-voids along the interface of copper to the copper oxide. No micro-voids were observed in the samples that were heat treated at 150 ˚C and below. Scattered micro-voids were observed at the interface region of the samples that were heat treated at 180 ˚C and 210 ˚C. At the higher heat treatment temperature; 240 ˚C, the micro-voids start to initiate the separation in between the copper oxide and the bulk copper.

This volume defect is an effect of Kirkendall voids. Once the copper oxide is formed, it has different diffusion kinetics than the copper itself. Since the diffusion mechanism involves lattice vacancies, an atom can move into a vacant lattice site, effectively causing the atom and the vacancy to switch places. If large-scale diffusion takes place at the copper to the copper oxide interface, there will be a flux of atoms in one direction and a flux of vacancies in the other direction which results in volume defects which are also termed as micro-voids or separations. In many metals, voids will form in the oxide film when oxidized, especially at the metal-oxide interface (Lee, 2008). These voids formation, a volume defect, causes the electron beams to transmit easily during the TEM imaging process resulting in bright contrast as compared to the intact areas. The micro-voids may cause poor adhesion in between the copper oxide and bulk copper. Severe effects may be experienced at higher temperatures since complete separation may occur. In semiconductor packaging, poor adhesion at this interface region was found to be the root cause of the delamination issue and product failure (Gen, 2011).

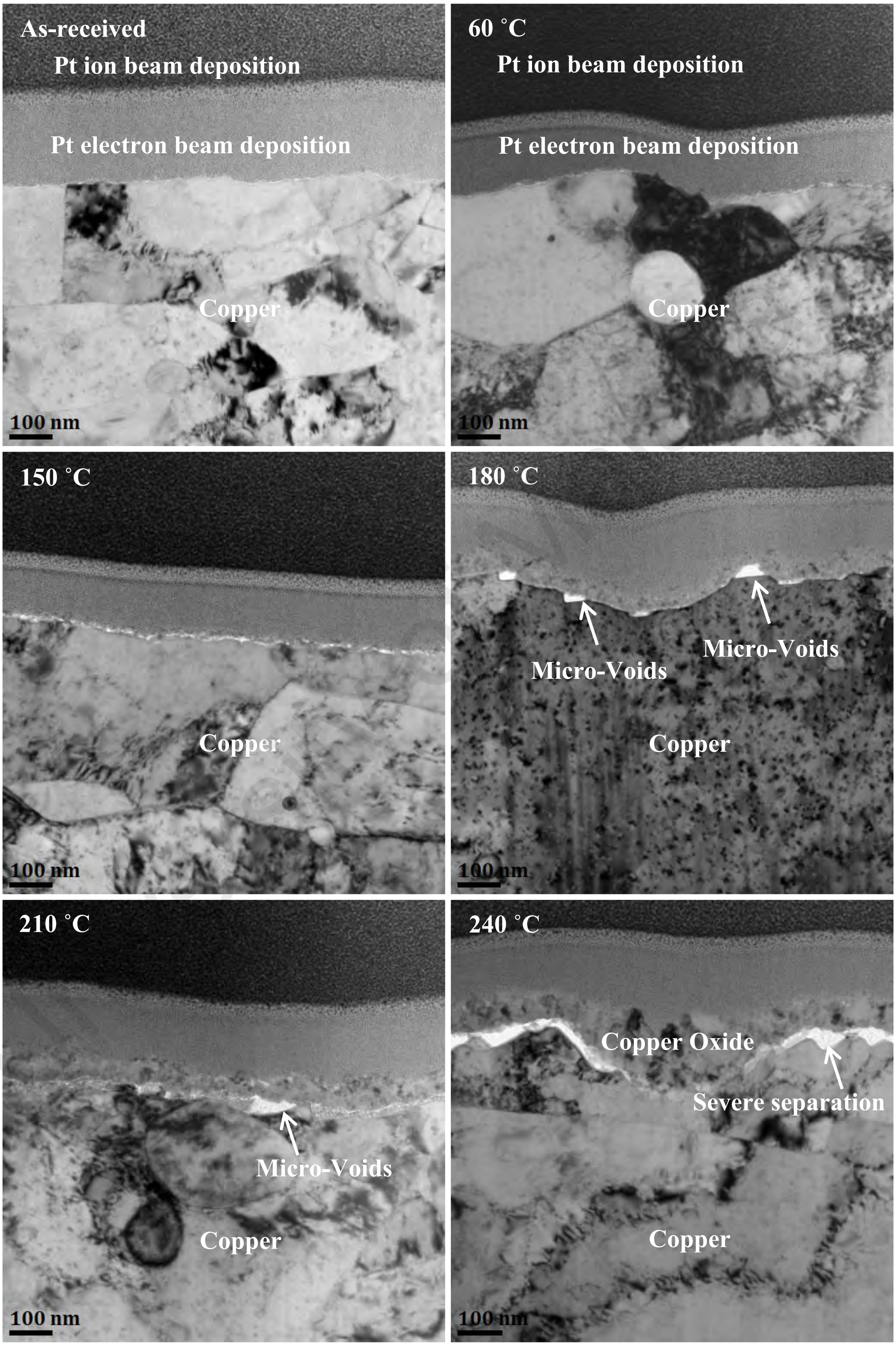

Figure 4.26: The TEM micrograph.

Gondcharton (2015) in his study of TiN-Cu bonding also observed a void nucleation and growth at the bonding interface of TiN-Cu, during post bonding annealing at the temperature beyond 300 ˚C. This phenomenon suggested to the vacancy diffusion due to thermal stress sustained by copper during post bonding thermal budget.

4.3.4 Crystal Structure of Copper Oxide

The atomic structure of the copper oxide was further investigated using HRTEM technique at 530,000 times of magnification. Figure 4.26 shows the atomic structure of the copper oxide.

The polycrystalline structure of the copper oxide was obtained by the SAED analysis. The SAED pattern was acquired in the middle portion of the copper oxide, excluding the interface area, bulk copper region and Pt deposition area. The copper oxide shows the crystalline structure with 0.24 nm to 0.25 nm lattice fringe spacing and has a monoclinic structure.

The SAED pattern shows that most of the middle part of the copper oxide had the oxidation state of Cu_2O. Savaliya (2015) in his copper oxide studies had also reported a similar d-spacing result that the distance between two peaks shows the d-spacing value of 0.23 nm and the copper oxide structure was found to have a monoclinic structure based on the XRD analysis.

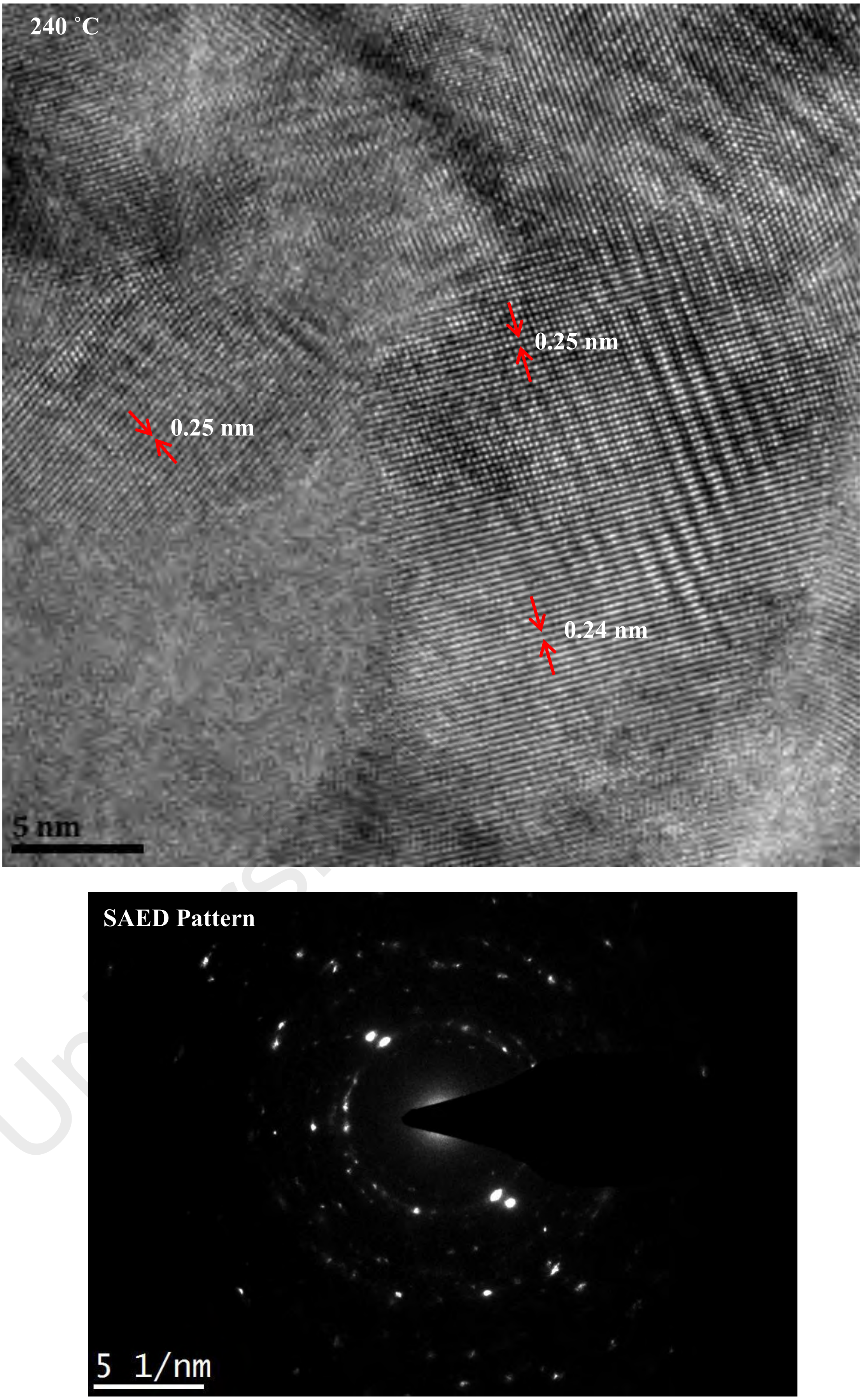

Figure 4.27: Atomic structure and SAED pattern of copper oxide.

CHAPTER 5: CONCLUSION AND FUTURE WORK

5.1 Conclusion

The heat treatment process promotes the oxidation on the copper alloy leadframe samples. The oxidation was found to cause the physical colour transformation from light brown to dark brown. The change in the surface texture from tiny particle to a bigger particle size were also the effects of the oxidation. At 150 °C, the particle size in the range of 20 nm to 50 nm was observed on the sample surface. The agglomeration of bigger particle size up to 100 nm at 210 °C shows an initiation of isotropic growth of the surface grain due to the oxidation. The increase in the heat treatment temperature to 240 °C, caused the growth of near spherical shape of surface grains with porous surfaces. The oxidation was also caused the change in the mechanical properties of the copper alloy leadframe samples. The surface hardness of the samples was found to be increased with an increasing of heat temperature temperature. The coarse granular surface derived from high temperature treatment was found to be hard and brittle. The effect of stress corrosion cracking occurs at the heat treatment temperatures of 240 °C as the sample is subjected to a mechanical deformation.

The oxidation forms a copper oxide layer on the copper alloy leadframe surface. The thickness of the copper oxide layer was found to be increased as the heat treatment temperature increases. At high heat treatment temperatures, the formation of micro-voids and separations along the interface of the copper oxide to the copper alloy leadframe provides a strong evidence why a delamination is likely to occur at this interface. In this research work, the oxidation system of $CuO/Cu_2O/CuO/Cu$ was found on the sample that has an intact interface region in between the copper oxide to the copper alloy leadframe. The activation energy was found to be 41 kJ/mol.

5.2 Future Work

Further works can be done in this field of research on the effect of copper alloy leadframe samples with solder material and to study the level of oxidation to the reaction of solder material as well as the IMC layer. The work can be focused on the interaction of the Sn-Ag-Cu derived from solder material to the level of oxidation from the surface of the copper alloy leadframe. The elastic properties and the hardness properties of the IMC phase after oxidation can be further examined to understand the effect of these properties to the bonding strength of copper oxide and IMC layer. For each intermetallic phase, the type of crystal structure, electrical resistivity and the material properties can be further investigated as well. The mechanical stress acting on the void interface between the copper oxide and IMC layer can also be studied in details. This study will provide a potential understanding of the solderability issue that is one of the main critical process issues in the current semiconductor packaging industries.

REFERENCES

Ahn, C. C. (Ed.). (2006). *Transmission Electron Energy Loss Spectrometry in Materials Science and the EELS Atlas.* New York, NY: John Wiley and Sons.

Ahn, C. C., & Krivanek, O. L. (1983). *EELS Atlas*. Warrendale, PA: Gatan.

An.reoli, T. E., Fanestil, D. D., Hoffman, J. F., & Schultz, S. (2013). *Physiology of Membrane Disorders*. Heidelberg, Germany: Springer Science and Business Media.

Austin, A. E., & Richard, N. A. (1961). Grain Boundary Diffusion. *Journal of Applied Physics, 32*(8), 1462-1471.

Balluffi, R. W., Allen, S., & Carter, W. C. (2005). *Kinetics of Materials.* New York, NY: John Wiley and Sons.

Barsoum, M., & Barsoum, M. W. (2002). *Fundamentals of Ceramics*. Boca Raton, FL: CRC Press.

Bartos, P. (2004). *Nanotechnology in Construction*. London, England: Royal Society of Chemistry.

Bell, D. C., & Garratt-Reed, A. J. (2003). *Energy Dispersive X-Ray Analysis in the Electron Microscope*. New York, NY: Garland Science.

Belousov, V. V., & Klimashin, A. A. (2013). High Temperature Oxidation of Copper. *Russian Chemical Reviews*, *82*(3), 273.

Beranger, G., Armanet, F., & Lambertin, M. (1989). *Role of Active Elements in the Oxidation Behaviour of High Temperature Metals and Alloys*. Heidelberg, Germany: Springer.

Berriche, R., Lowry, R., & Rosenfield, M. I. (1999). An Oxidation Study of Cu Leadframes. *International Symposium on Advanced Packaging Materials: Processes, Properties and Interface* (pp. 275-281).

Birkebak, R. C., & E. R. G. Eckert. (1965). Effects of Roughness of Metal Surfaces on Angular Distribution of Monochromatic Reflected Radiation. *Journal of Heat Transfer, 87*, 85-93.

Bishop, M. (2013). *An Introduction to Chemistry - Oxidation-Reduction Reactions* (pp. 207-47). Monterey, California: Chiral Publishing Company.

Bogicevic, A., & Jennison, D. R. (2002). Effect of Oxide Vacancies on Metal Island Nucleation. *Surface Science*, *515*(2), 481-486.

Brook, R. J. (Ed.). (2012). *Concise Encyclopedia of Advanced Ceramic Materials*. Amsterdam, Netherlands: Elsevier.

Buseck, P., Cowley, J., & Eyring, L. (Eds.). (1989). *High Resolution Transmission Electron Microscopy: And Associated Techniques*. Oxford, England: Oxford University Press.

Cahn, R. W., & Lifshitz, E. M. (Eds.). (2016). *Concise Encyclopedia of Materials Characterization*. Amsterdam, Netherlands: Elsevier.

Callister W. D., (1996). *Materials Sciences and Engineering - An Introduction*. New York, NY: John Wiley and Sons.

Carlson, T. (2013). *Photoelectron and Auger Spectroscopy.* Heidelberg, Germany: Springer Science and Business Media.

Cho, S. J., & Paik, K. W. (1998). Oxidation Studies on a Cu-Base Leadframe Alloy between 150 °C and 300 °C. *Scripta Materialia*, *38*(7), 1149-1154.

Chong, C. T., Leslie, A., Beng, L. T., & Lee, C. (1995). Investigation on the Effect of Copper Leadframe Oxidation on Package Delamination. *Electronic Components and Technology Conference* (pp. 463-469).

Chuang, C. L., Aoh, J. N., & Din, R. F. (2006). Oxidation of Copper Pads and Its Influence on the Quality of Au/Cu Bonds during Thermosonic Wire Bonding Process. *Microelectronics Reliability*, *46*(2), 449-458.

Connors, K. A. (1990). *Chemical Kinetics: The Study of Reaction Rates in Solution*. New York, NY: John Wiley and Sons.

Cotterill, P., & Mould, P. R. (1976). *Recrystallization and Grain Growth in Metals*. Malabar, FL: Krieger Publishing.

Cottis, R. A. (Ed.). (2009). *Shreir's Corrosion*. Amsterdam, Netherlands: Elsevier Science.

Davis, J. R. (Ed.). (2001). *Copper and Copper Alloys*. Geauga County, Ohio: ASM International.

Deo, N. N. S., & Chang, A. H. (1994). *U.S. Patent No. 5,281,849.* Washington, DC: U.S. Patent and Trademark Office.

Diamanti, M. V., Del Curto, B., & Pedeferri, M. (2008). Interference Colors of Thin Oxide Layers on Titanium. *Color Research and Application*, *33*(3), 221.

EDFAS Desk Reference Committee. (2011). *Microelectronics Failure Analysis: Desk Reference*. Geauga County, Ohio: ASM International.

Fernández, A. I., Uranga, P., López, B., & Rodriguez-Ibabe, J. M. (2000). Static Recrystallization Behaviour of a Wide Range of Austenite Grain Sizes in Microalloyed Steels. *ISIJ International*, *40*(9), 893-901.

Fujita, K., Ando, D., Uchikoshi, M., Mimura, K., & Isshiki, M. (2013). New Model for Low Temperature Oxidation of Copper Single Crystal. *Applied Surface Science*, *276*, 347-358.

Gattinoni, C., & Michaelides, A. (2015). Atomistic Details of Oxide Surfaces and Surface Oxidation: The Example of Copper and Its Oxides. *Surface Science Reports*, *70*(3), 424-447.

Garverick, L. (Ed.). (1994). *Corrosion in the Petrochemical Industry*. Geauga County, Ohio: ASM International.

Geiger, C. A. (2001). *Solid Solutions in Silicate and Oxide Systems*. Twickenham, England: The Mineralogical Society of Great Britain and Ireland.

Gen, W., Chen, X., Hu, A., & Li, M. (2011). Effect of Ag on Oxidation of Cu-Base Leadframe. *Microelectronics Reliability*, *51*(4), 866-870.

Goldstein, J. (Ed.). (2012). *Practical Scanning Electron Microscopy: Electron and Ion Microprobe Analysis.* Heidelberg, Germany: Springer Science and Business Media.

Gonçalves, A. M. B., Campos, L. C., Ferlauto, A. S., & Lacerda, R. G. (2009). On the Growth and Electrical Characterization of CuO Nanowires by Thermal Oxidation. *Journal of Applied Physics*, *106*(3), 034303.

Gondcharton, P., Imbert, B., Benaissa, L., & Verdier, M. (2015). Copper-Copper Direct Bonding: Impact of Grain Size. *Interconnect Technology and Materials for Advanced Metallization Conference* (pp. 229-232).

Guleryuz, H., & Cimenoglu, H. (2005). Surface Modification of a Ti-6Al-4V Alloy by Thermal Oxidation. *Surface and Coatings Technology*, *192*(2), 164-170.

Hashmi, S. (2014). *Comprehensive Materials Processing*. Amsterdam, Netherlands: Elsevier.

Haque, M. M., & Khan, A. A. (2008). Investigation on Structure and Properties of Brass Casting. *Journal of Materials Science and Technology*, *24*(3), 299-301.

Haque, M. M., & Ismail, A. F. (2008). Effect of Cooling Rate on Strength and Fracture Surfaces of Alpha Brass Casting. *Advanced Materials Research, 33,* 7-12.

Henderson, G., Neuville, D., & Downs, R. (Eds.). (2014). *Spectroscopic Methods in Mineralogy and Material Sciences*. Berlin, Germany: Walter de Gruyter GmbH and Co KG.

Herrmann, K. (Ed.). (2011). *Hardness Testing: Principles and Applications*. Geauga County, Ohio: ASM International.

Hillard, R. J., & Roberds, B. (1999). Analytical and Diagnostic Techniques for Semiconductor Materials. *Devices and Processes*, *16*, 385.

Huebschen, G., Altpeter, I., Tschuncky, R., & Herrmann, H. G. (Eds.). (2016). *Materials Characterization Using Nondestructive Evaluation (NDE) Methods*. Cambridge, England: Woodhead Publishing.

Horváth, B., Shinohara, T., & Illés, B. (2013). Corrosion Properties of Tin-Copper Alloy Coatings in Aspect of Tin Whisker Growth. *Journal of Alloys and Compounds*, *577*, 439-444.

Hou, Y. Q., Zhuang, D. M., Zhang, G., Zhao, M., & Wu, M. S. (2003). Influence of Annealing Temperature on the Properties of Titanium Oxide Thin Film. *Applied Surface Science*, *218*(1), 98-106.

Hsieh, J. H., & Li, C. (2006). Effects of Hollow Cathode and Ar/H_2 Ratio on Plasma Cleaning of Cu Leadframe. *Thin Solid Films*, *504*(1), 101-103.

Izquierdo, J., Santana, J. J., González, S., & Souto, R. M. (2010). Uses of Scanning Electrochemical Microscopy for the Characterization of Thin Inhibitor Films on Reactive Metals: The Protection of Copper Surfaces by Benzotriazole. *Electrochimica Acta*, *55*(28), 8791-8800.

Jackson, S. D., & Hargreaves, J. S. (2009). *Metal Oxide Catalysis*. New York, NY: John Wiley and Sons.

Jain, V. K. (Ed.). (2017). *Nanofinishing Science and Technology: Basic and Advanced Finishing and Polishing Processes*. Boca Raton, FL: CRC Press.

Jernigan, G. G., & Somorjai, G. A. (1994). Carbon Monoxide Oxidation Over Three Different Oxidation States of Copper: Metallic Copper, Copper (I) Oxide, and Copper (II) Oxide - A Surface Science and Kinetic Study. *Journal of Catalysis*, *147*(2), 567-577.

Jiles, D. (2008). *Introduction to the Principles of Materials Evaluation*. Boca Raton, FL: CRC Press.

Jones, R. H., Ricker, R. E., & Jones, R. H. (1992). Mechanisms of Stress Corrosion Cracking in Stress Corrosion Cracking - Materials Performance and Evaluation. *Materials Park*, Geauga County, Ohio: ASM International.

Kim, J. K., Lebbaj, M., Liu, J. H., Kim, J. H., & Yuen, M. M. (2000). Interface Adhesion Between Copper Leadframe and Epoxy Moulding Compound: Effects of Surface Finish, Oxidation and Dimples. *Electronic Components and Technology Conference* (pp. 601-608).

Kim, J. K., Woo, R. S., Hung, P. Y., & Lebbai, M. (2006). Adhesion Performance of Black Oxide Coated Copper Substrates: Effects of Moisture Sensitivity Test. *Surface and Coatings Technology*, *201*(1), 320-328.

Krupp, U. (2007). *Fatigue Crack Propagation in Metals and Alloys: Microstructural Aspects and Modelling Concepts*. New York, NY: John Wiley and Sons.

Lahiri, S. K., Singh, N. W., Heng, K. W., Ang, L., & Goh, L. C. (1998). Kinetics of Oxidation of Copper Alloy Leadframes. *Microelectronics Journal*, *29*(6), 335-341.

Lee, H. J., & Yu, J. (2008). Study on the Effects of Copper Oxide Growth on the Peel Strength of Copper/Polyimide. *Journal of Electronic Materials*, *37*(8), 1102-1110.

Lee, H. Y. (2001). Failure Paths of the Cu-Based Leadframe/EMC Joints. *Materials Science and Engineering: A*, *311*(1), 217-225.

Lee, H. Y., Park, Y. B., Jeon, I., Kim, Y. H., & Chang, Y. K. (2005). Analysis of Failure of Nanobelt-Coated Copper-Based Leadframe/Epoxy-Based Molding Compound Systems After Pull-Out Test. *Materials Science and Engineering: A*, *405*(1), 50-64.

Lalena, J. N., & Cleary, D. A. (2010). *Principles of Inorganic Materials Design*. New York, NY: John Wiley and Sons.

Leong, G. C., & Uda, H. (2013). Comparative Reliability Studies and Analysis of Au, Pd-Coated Cu and Pd-Doped Cu Wire in Microelectronics Packaging. *PloS one*, *8*(11), e78705.

Li, J., & Dasgupta, A. (1994). Failure Mechanism Models for Material Aging due to Interdiffusion. *Transactions on Reliability*, *43*(1), 2-10.

Li, W. H., & Ong, S. J. (2012). Cu Diffusion in Ag-Plated Cu Leadframe Packages. *Microelectronics Reliability*, *52*(7), 1523-1527.

Lin, R., Blackshear, E., & Serisky, P. (1988). Moisture Induced Package Cracking in Plastic Encapsulated Surface Mount Components during Solder Reflow Process. *International Reliability Physics Symposium* (pp. 83-89).

Lin, T. Y., Leong, W. S., Chua, K. H., Oh, R., Miao, Y., Pan, J. S., & Chai, J. W. (2002). The Impact of Copper Contamination on the Quality of the Second Wire Bonding Process Using X-Ray Photoelectron Spectroscopy Method. *Microelectronics Reliability*, *42*(3), 375-380.

Liu, P., Tong, L., Wang, J., Shi, L., & Tang, H. (2012). Challenges and Developments of Copper Wire Bonding Technology. *Microelectronics Reliability*, *52*(6), 1092-1098.

Lobnig, R. E., Frankenthal, R. P., Siconolfi, D. J., Sinclair, J. D., & Stratmann, M. (1994). Mechanism of Atmospheric Corrosion of Copper in the Presence of Submicron Ammonium Sulfate Particles at 300 and 373 K. *Journal of the Electrochemical Society*, *141*(11), 2935-2941.

Maki, K., Ito, Y., Matsunaga, H., & Mori, H. (2013). Solid Solution Copper Alloys with High Strength and High Electrical Conductivity. *Scripta Materialia*, *68*(10), 777-780.

Manfredi, C., & Otegui, J. L. (2002). Failures by SCC in Buried Pipelines. *Engineering Failure Analysis*, *9*(5), 495-509.

Marcus, P., & Mansfeld, F. B. (Eds.). (2005). *Analytical Methods in Corrosion Science and Engineering*. Boca Raton, FL: CRC Press.

Mehrer, H. (2007). *Diffusion in Solids: Fundamentals, Methods, Materials, Diffusion Controlled Processes*. Heidelberg, Germany: Springer Science and Business Media.

Miura, K., & Maki, T. (1998). A Simple Method for Estimating f (E) and k 0 (E) in the Distributed Activation Energy Model. *Energy and Fuels*, *12*(5), 864-869.

Morgan, W. D. (1949). *The Encyclopedia of Photography: AZ*. Clearwater, FL: National Educational Alliance.

Nakayama, W., Boulton, W., & Pecht, M. (1999). *The Japanese Electronics Industry*. Boca Raton, FL: CRC Press.

Neikov, O. D., Murashova, I. B., Yefimov, N. A., & Naboychenko, S. (2009). *Handbook of Non-Ferrous Metal Powders: Technologies and Applications*. Amsterdam, Netherlands: Elsevier.

Nellist, P. D., & Pennycook, S. J. (Eds.). (2011). *Scanning Transmission Electron Microscopy: Imaging and Analysis*. Heidelberg, Germany: Springer.

Nishi, Y., & Doering, R. (Eds.). (2000). *Handbook of Semiconductor Manufacturing Technology*. Boca Raton, FL: CRC Press.

Nogi, K., Naito, M., & Yokoyama, T. (2012). *Nanoparticle Technology Handbook*. Amsterdam, Netherlands: Elsevier.

Ohno, Y., & Ohzeki, Y. (1993). *U.S. Patent No. 5,227,662*. Washington, DC: U.S. Patent and Trademark Office.

Orloff, J. (2009). *Charged Particle Optics*. New York, NY: John Wiley and Sons.

Padua, G. W., & Wang, Q. (2012). *Nanotechnology Research Methods for Food and Bioproducts*. New York, NY: John Wiley and Sons.

Panter, J., Viguier, B., Cloué, J. M., Foucault, M., Combrade, P., & Andrieu, E. (2006). Influence of Oxide Films on Primary Water Stress Corrosion Cracking Initiation of Alloy 600. *Journal of Nuclear Materials*, *348*(1), 213-221.

Park, B. K., Kim, D., Jeong, S., Moon, J., & Kim, J. S. (2007). Direct Writing of Copper Conductive Patterns by Ink-Jet Printing. *Thin Solid Films*, *515*(19), 7706-7711.

Park, J. H., & Natesan, K. (1993). Oxidation of Copper and Electronic Transport in Copper Oxides. *Oxidation of Metals*, *39*(5), 411-435.

Paul, A., Laurila, T., Vuorinen, V., & Divinski, S. V. (2014). *Thermodynamics, Diffusion and the Kirkendall Effect in Solids*. Heidelberg, Germany: Springer.

Peacock, D. G., & Richardson, J. F. (Eds.). (2012). *Chemical Engineering: Chemical and Biochemical Reactors and Process Control*. Amsterdam, Netherlands: Elsevier.

Pelzer, R., Nelhiebel, M., Zink, R., Wöhlert, S., Lassnig, A., & Khatibi, G. (2012). High Temperature Storage Reliability Investigation of the Al-Cu Wire Bond Interface. *Microelectronics Reliability*, *52*(9), 1966-1970.

Petrucci, R. H., Harwood, W. S., & Herring, F. G. (1997). General Chemistry, Principles and Modern Applications. *Journal of Chemical Education, 74*(5), 491.

Picone, A., Riva, M., Brambilla, A., Calloni, A., Bussetti, G., Finazzi, M., ... & Duò, L. (2016). Reactive Metal-Oxide Interfaces: A Microscopic View. *Surface Science Reports*, *71*(1), 32-76.

Proulx, T. (Ed.). (2011). *Experimental Mechanics on Emerging Energy Systems and Materials: Annual Conference on Experimental and Applied Mechanics*. Heidelberg, Germany: Springer Science and Business Media.

Reardon, A. C. (Ed.). (2011). *Metallurgy for the Non-metallurgist*. Geauga County, Ohio: ASM International.

Rollett, A., Humphreys, F. J., Rohrer, G. S., & Hatherly, M. (2004). *Recrystallization and Related Annealing Phenomena*. Amsterdam, Netherlands: Elsevier.

Romano, I., (2015). *About Copper*. Beussels, Belgium: Copper Institute.

Russ, J. C. (2013). *Fundamentals of Energy Dispersive X-Ray Analysis: Butterworths Monographs in Materials*. Oxford, England: Butterworth-Heinemann.

Savaliya, C., Rathod, K. N., Dhruv, D., & Markna, J. H. (2015). Preparation of Nanostructured Copper Oxide Rods Using Advanced Sonication Method. *International Journal of Nanoscience and Nanoengineering*, *2*(4), 27.

Schulz, M. J., Kelkar, A. D., & Sundaresan, M. J. (Eds.). (2005). *Nanoengineering of Structural, Functional and Smart Materials.* Boca Raton, FL: CRC Press.

Schwarz, J. A., Contescu, C. I., & Putyera, K. (2004). *Dekker Encyclopedia of Nanoscience and Nanotechnology*. Boca Raton, FL: CRC Press.

Segneanu, A. E., Grozescu, I., Balcu, I., Vlatanescu, N., & Sfirloaga, P. (2012). *A Comparative Study Between Different Corrosion Protection Layers*. Rijeka, Croatia: INTECH Open Access Publisher.

Sequeira, C. A. C., & Amaral, L. (2014). Role of Kirkendall Effect in Diffusion Processes in Solids. *Transactions of Nonferrous Metals Society of China*, *24*(1), 1-11.

Serp, P., & Figueiredo, J. L. (Eds.). (2009). *Carbon Materials for Catalysis*. New York, NY: John Wiley and Sons.

Shook, R. L., & Goodelle, J. P. (2000). Handling of Highly Moisture Sensitive Components - An Analysis of Low Humidity Containment and Baking Schedules. *Electronics Packaging Manufacturing*, *23*(2), 81-86.

Shuisheng, X., Yanli, L., & Lin, Z. (2003). Progress of Study on Leadframe Copper Alloy and Its Implementation in Electronic Industry. *Chinese Journal of Rare Metals*, *6*, 031.

Smith, I. C., & Carson, B. L. (1977). *Trace Metals in the Environment*. New York, NY: American Society of Agronomy.

Tabor, D. (2000). *The Hardness of Metals*. Oxford, England: Oxford University Press.

Tan, C. W., Daud, A. R., & Yarmo, M. A. (2002). Corrosion Study at Cu-Al Interface in Microelectronics Packaging. *Applied Surface Science*, *191*(1), 67-73.

Tandon, R. (2014). *Parson's Diseases of the Eye*. Amsterdam, Netherlands: Elsevier Health Sciences.

Tay, A. A. O., & Lin, T. Y. (1996). Effects of Moisture and Delamination on Cracking of Plastic IC Packages during Solder Reflow. *Electronic Components and Technology Conference* (pp. 777-782).

Thorvaldsen, A. (1997). The Intercept Method-2. Determination of Spatial Grain Size. *Acta Materialia*, *45*(2), 595-600.

Totten, G. (2008). Fatigue Crack Propagation. *Advanced Materials and Processes*, *166*(5), 39.

Tung, C. H., Sheng, G. T., & Lu, C. Y. (2003). *ULSI Semiconductor Technology Atlas*, New York, NY: John Wiley and Sons.

Tylecote, R. F. (1951). Review of Published Information on the Oxidation and Scaling of Copper and Copper Base Alloys. *Journal of the Institute of Metals*, *78,* 259-299.

Valensi, G. (1948). Theoretical and Experimental Investigations About Conjugated Formation of Several Layers. *International Conference on Surface Reactions* (pp. 156-164).

Venables, J. A., & Harding, J. H. (2000). Nucleation and Growth of Supported Metal Clusters at Defect Sites on Oxide and Halide (001) Surfaces. *Journal of Crystal Growth*, *211*(1), 27-33.

Vij, D. R. (Ed.). (2007). *Handbook of Applied Solid State Spectroscopy*. Heidelberg, Germany: Springer Science and Business Media.

Voigtländer, B. (2015). *Scanning Probe Microscopy: Atomic Force Microscopy and Scanning Tunneling Microscopy*. Heidelberg, Germany: Springer.

Volkov, A. Y. (2004). Improvements to the Microstructure and Physical Properties of Pd-Cu-Ag Alloys. *Platinum Metals Review*, *48*(1), 3-12.

Wan, Y., Wang, X., Sun, H., Li, Y., Zhang, K., & Wu, Y. (2012). Corrosion Behavior of Copper at Elevated Temperature. *International Journal of Electrochemical Science*, *7*, 7902-7914.

Whitaker, J. C. (Ed.). (1996). *The Electronics Handbook*. Boca Raton, FL: CRC Press.

Williams, D. B., & Carter, C. B. (1996). *The Transmission Electron Microscope*. Heidelberg, Germany: Springer.

William F.. Smith, & Hashemi, J. (2011). *Foundations of Materials Science and Engineering*. New York, NY: McGraw-Hill.

Woodtli, J., & Kieselbach, R. (2000). Damage due to Hydrogen Embrittlement and Stress Corrosion Cracking. *Engineering Failure Analysis*, *7*(6), 427-450.

Yariv, A., & Yeh, P. (1984). *Optical Waves in Crystals*. New York, NY: Wiley.

Yee, L. F., & Yew, C. L. W. (2012). Die Attach Materials Impacts to Copper Wire Bonding: New Challenges. *Electronics Packaging Technology Conference* (pp. 263-268).

Zeng, K., Stierman, R., Chiu, T. C., Edwards, D., Ano, K., & Tu, K. N. (2005). Kirkendall Void Formation in Eutectic SnPb Solder Joints on Bare Cu and Its Effect on Joint Reliability. *Journal of Applied Physics*, *97*(2), 024508.

Zhang, X., Wallinder, I. O., & Leygraf, C. (2014). Mechanistic Studies of Corrosion Product Flaking on Copper and Copper Based Alloys in Marine Environments. *Corrosion Science*, *85*, 15-25.

Zheng, Y. (2003). Study of Copper Applications and Effects of Copper Oxidation in Microelectronic Package. *Partial Fulfillment of MatE*, *234*, 1-26.

Zhao, W., Wu, J., Hu, A., Li, M., & Mao, D. (2010). An Investigation into Copper Oxidation Behavior. *International Conference on Electronic Packaging Technology and High Density Packaging* (pp. 319-323).

Zhou, G., & Yang, J. C. (2004). Temperature Effects on the Growth of Oxide Islands on Cu (110). *Applied Surface Science, 222*(1), 357-364.

Zhou, Y., Yang, L., & Huang, Y. (2013). *Micro and Macromechanical Properties of Materials.* Boca Raton, FL: CRC Press.

Zhu, Y. W., Yu, T., Cheong, F. C., Xu, X. J., Lim, C. T., Tan, V. B. C., ... & Sow, C. H. (2004). Large Scale Synthesis and Field Emission Properties of Vertically Oriented CuO Nanowire Films. *Nanotechnology*, *16*(1), 88-92.

Zhu, Y., Mimura, K., & Isshiki, M. (2002). Oxidation Mechanism of Copper at 623-1073 K. *Materials Transactions*, *43*(9), 2173-2176.

LIST OF PUBLICATIONS AND PAPERS PRESENTED

1. Esa, S. R., Yahya, R., Hassan, A., & Omar, G. (2012). Copper Oxidation Study by TEM. *Physical and Failure Analysis of Integrated Circuits International Symposium* (pp. 1-5).

2. Esa, S. R., Omar, G., Yahya, R., Tamaldin, N., Hassan, A., Abdul Rahim, B., ... & Azli, W. (2016). Electron Microscopic Investigation on Nanostructure Behaviors of Thermal Oxidation Copper. *Key Engineering Materials*, *694*, 116-119.

3. Esa, S. R., Yahya, R., Hassan, A., & Omar, G (2016). Nano-scale Copper Oxidation on Leadframe Surface. *Ionics*, *23*(2), 319-329.